Films minces magnétiques sur substrat flexible : Etude des effets magnéto-mécaniques par résonance ferromagnétique

Mouhamadou Gueye

École doctorale Galilée

Doctorat de physique

THÈSE

pour obtenir le grade de docteur délivré par

l'Université Paris XIII

Spécialité "Science des Matériaux"

présentée par

Mouhamadou Gueye

soutenue
le 27 Mars 2017

Magnetic thin films on flexible substrates: magnetomechanical study by ferromagnetic resonance

Jury

Mme. Alexandra Mougin	Rapporteur
M. Vincent Repain	Rapporteur
M. Mohamed Belmeguenai	Examinateur
M. Manuel Bibes	Examinateur
M. Damien Faurie	Examinateur
M. Philippe Goudeau	Examinateur
M. Michel Viret	Examinateur
M. Fatih Zighem	Examinateur

Université Paris XIII
Laboratoire des Sciences des Procédés et des Matériaux (LSPM)
UPR CNRS 3407, 99 avenue J. B. Clément, 93430 Villetaneuse, France

THESE

École doctorale Galilée

Doctorat de physique

THÈSE

pour obtenir le grade de docteur délivré par

l'Université Paris XIII

Spécialité "Science des Matériaux"

présentée par

Mouhamadou Gueye

soutenue
le 27 Mars 2017

Magnetic thin films on flexible substrates: magnetomechanical study by ferromagnetic resonance

Jury

Mme. Alexandra Mougin	Rapporteur
M. Vincent Repain	Rapporteur
M. Mohamed Belmeguenai	Examinateur
M. Manuel Bibes	Examinateur
M. Damien Faurie	Examinateur
M. Philippe Goudeau	Examinateur
M. Michel Viret	Examinateur
M. Fatih Zighem	Examinateur

Université Paris XIII
Laboratoire des Sciences des Procédés et des Matériaux (LSPM)
UPR CNRS 3407, 99 avenue J. B. Clément, 93430 Villetaneuse, France

THESE

Table des matières

Table des figures

Liste des tableaux

Acknowledgments

I would like to thank most sincerely ladies and gentlemen of the jury who have agreed to comment and criticize this thesis project. I am most grateful to Manuel Bibes, Philippe Goudeau, Michel Viret and to both rapporteurs Alexandra Mougin and Vincent Repain.

I sincerely thank Fatih Zighem, Damien Faurie and Mohamed Belmeguenai for their invaluable contribution.Thanks to them, I have had the good fortune to work on very rich project. Their guidance has been relevant, I learned a lot thanks to them. Our regular formal or informal conversations have always been for me inspirational and motivational. Fatih has always been present and patiently answered to all my questions. I would like to express my appreciation and my thanks to him. It has been a genuine pleasure to work with them. I would also like to thank them for placing their trust in me and for having given me a freedom in my way of working and managing my time. I've had the opportunity to present wy works at conferences both in the national and international contexts. Againg thank you for manuscrit revisions. I would like to warmly thank all the member of the FINANO team in which this thesis project has been done.

I would like to thank all our collaborators who have contributed to the success of this project : Dr Mihai Gabor from the Center for Superconductivity, Spintronics and Surface Science, Technical University of Cluj-Napoca for having elaborated the Co_2FeAl and Pr. A.O. Adeyeye and his team from the National University of Singapour for having provided us CoFeB samples.

I would particularly like to thank Alexis Garcia Sanchez engineer in LSPM and all the PhD students (Béucia Bermane, Tarik Sadat, Stéphane Dufrenoy, Pauline Canaud, Kévin Ardon, Sabrine Ayadi, Skander Merabtine and all the others). Thanks for the good time we had during these last three years. I wish you bon courage and every success for those of you who have not finished yet their thesis project.

I cannot conclude my acknowledgments without paying a respectful homage to my family for their support and encouragement. Thank you a lot to you Megueye Gueye, Fatou Sall, Seynabou Gueye, Pape Gueye, Seynabou Sall.I would also like to thank my wife, Kandé, for her unflagging support.

I would like to thank Debo Gueye, Aboubakrine N'diaye, Lamine Gaye, Macoumba Gaye, Pape Mactar Diop, Sandjiry Diop, Cheikh Ndoye, Alioune Badara Seye and all the classemates of D.M.W.M France and everyone who have contributed both directly and indirectly in making this project a success.

Introduction

General context Devices fabricated on flexible substrates (polymers such as Kapton®, PET, PDMS, PVDF, ...) have been widely studied because of their remarkable potential for new applications requiring non-planar functional systems [1]. During last years, several electronic devices, such as flexible organic solar cells [2], light-emitting diodes [3], and transistors [4], have been realized on top of various polymeric substrates and even on paper. On a general point of view, flexible electronics has become a convincing technology undertaking with countless shape attributes, from single curvature conformal displays to complex curvilinear stretchable devices (especially for biomedical applications). The extent to which these thin films on flexible substrates can be safely bent or stretched are essential, but highly challenging design features.

An example is given in figure 0.0.1, showing advanced concepts for conformal wrapping of silicon-based circuits, initially fabricated in 2-Dimensional layouts, by using thin polymer/metal interconnects. The results provided new practical routes to the integration of high performance electronics with biological tissues and other systems of interest for new applications [5].

The realization of functional, transparent, flexible, and stretchable magnetic micro- and nano-structures may lead to a new generation of magnetic materials for sensing and recording as well as magneto-optical and magneto-photonic devices. The current generation of those technologies, utilizing more traditional substrate technologies, has been highly successful. This suggests that the new generation with added functionalities will also be a success. Giant magnetoresistance (GMR) or tunneling magnetoresistance (TMR) multilayer structures can be used for high-speed read / write heads in disk storage devices with their high magnetoresistance. Recently, GMR or TMR sensors manufactured on flexible substrates, called magnetoelectronics flexible, have attracted much interest because of their potential applications. Predictable applications of highly sensitive and flexible/stretchable magnetoelectronics encompass the in-flow detection of magnetic particles in advanced fluidics and lab-on-a-chip platforms, and in human tissues (health monitoring, ...). Moreover, moldable forms of consumer electronics devices and smart textiles will benefit from magnetic functionalities offered by compliant magnetoelectronics [6].

The pioneering works on GMR were made by Uhrmann *et al.* [7] and Ozkaya *et al.* [8]. The main purpose of these studies was to demonstrate the feasibility of a magnetostrictive sensors on a flexible polyimide substrate. Slightly later, Barraud *et al.* [9] showed that for magnetic tunneling junctions (MTJs) grown on flexible organic substrates, the spin dependent tunneling properties of spintronic devices can be preserved even after 1% mechanical strain. Among more recent papers, one can cite works made by Denys Makarov group (Helmholtz-Zentrum Dresden-Rossendorf, Germany), whose main interests are about applied features of magnetism in curved surfaces for sensoric applications. They have developed GMR multilayers (Co/Cu and Pemalloy/Cu) on stretchable (PET)

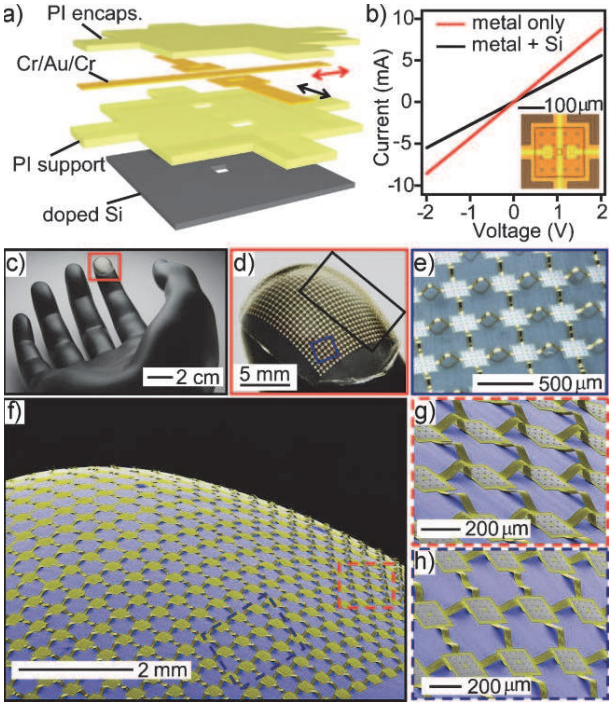

Figure 0.0.1 – a) Sketch of a layout of silicon, metal, and polymer layers in a unit cell of a silicon circuit mesh test structure. b) Current–voltage characteristics measured by contacting the continuous metal line. c,d) Photographs of the circuit mesh transferred onto the tip of a finger on a plastic substrate with the shape of a human hand. d) Magnified view of the region indicated by the box in (c). e) Magnified image of the region indicated by the blue box in (d) collected using a scanning focal technique. f, h) Colorized angled-view SEM images of the sample shown in c). g,h) Magnified views of areas indicated by the dashed boxes in f). The gray, yellow, and blue colors correspond to silicon, Polyimide (PI), and PDMS, respectively [5].

and flexible (Kapton®) substrates, as shown in Figure 0.0.2. They have demonstrated the potentialities of these systems for smart implants, and proximity sensorics for on-skin or wearable electronics but also to realize the sensory feedback for a unique class of soft actuators—soft robotics [10, 11].

Bedoya *at al.* have also studied flexible GMR systems [12]. They have characterized $Co/Al_2O_3/NiFe$ junctions deposited on Kapton®) substrate under bending. They showed that the performance were not affected upon substrate bending up to a radius of $r = 5$ mm, demonstrating the potential of these devices for flexible spintronic applications, see figure 0.0.3. Surprisingly, it seems that magnetoelastic effects and thin film damaging that would appears at relatively low strains (a few %) have a slight effect on magnetoresistive properties.

Concerning magnetic field sensorics, flexible GMI (giant magneto-impedance (MI)) systems were also developed by Li *et al.* [13]. Magneto-impedance properties of $Ni_{80}Fe_{20}/Cu/Ni_{80}Fe_{20}$ tri-layers deposited on Kapton® were studied by ferromagnetic resonance with *in situ* bending (figure 0.0.4). Particularly, they have shown that despite of very low magne-

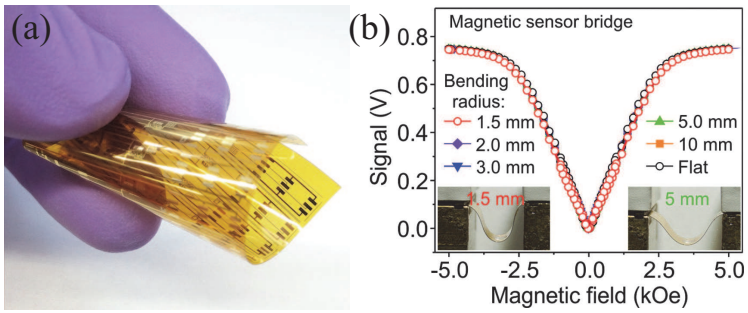

Figure 0.0.2 – a) Array of flexible magnetosensory systems. These are made of Co/Cu multilayers deposited on Kapton foils. These flexible magnetosensitive sensors can be used to monitor displacements or motion and provide feedback as needed. b) Response of the magnetic sensor bridge measured at different bending radii and plotted versus applied magnetic field.

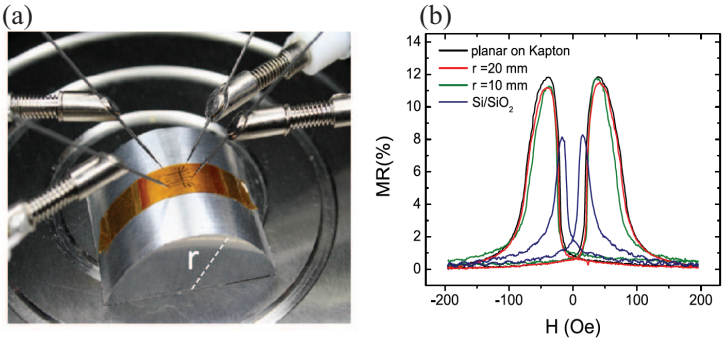

Figure 0.0.3 – a) Photograph of the bending angle magnetotransport experiment; the radius of the curved support is used as a parameter in the device characterization. b) MR ratio of flexible GMR system, as a function of applied magnetic field [12].

tostriction coefficient of the films ($\lambda = 6.22 \times 10^{-8}$), the magneto-impedance properties are very sensitive to elastic strains, e.g. to applied bending. Hence, the stability of this kind of sensors during deposition must be improved by adjusting the Ni_xFe_{1-x} alloy composition, with a vanishing magnetostriction at $x = 0.81$ [14].

Main issues The main issues are to understand how the applied strains to the flexible magnetic systems impact their magnetic properties. Obviously, when a thin film is deposited on a flexible substrate, it is usually submitted to high mechanical stresses due to the stretching or the curvature of the whole system. Moreover, these stresses are all the more important given that the Young's modulus contrast is high between the film and the substrate. This contrasts is characterized by the Dundurs parameter α:

$$\alpha = \frac{\overline{Y_f} - \overline{Y_s}}{\overline{Y_f} + \overline{Y_s}}$$

were $\overline{Y} = Y/\left(1-\nu^2\right)$ is the plane strain elastic modulus, ν is the Poisson ratio,

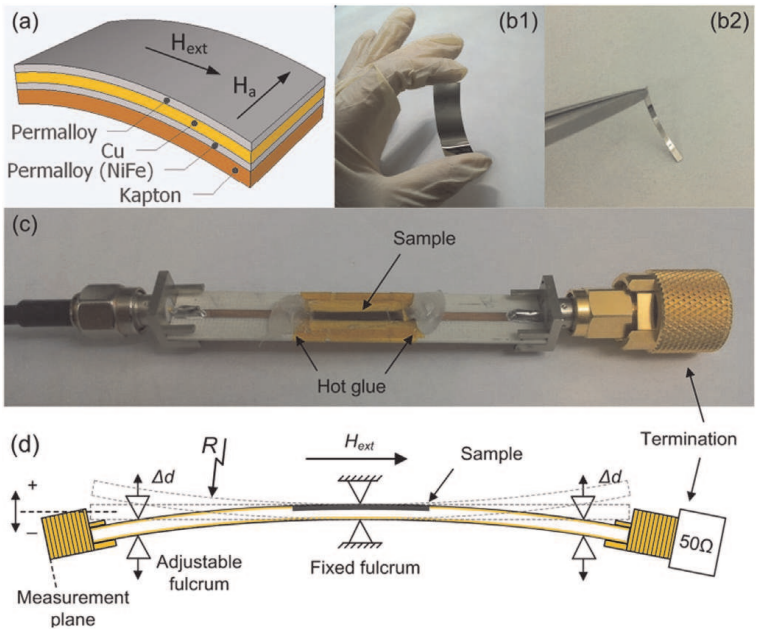

Figure 0.0.4 – a) The layer stack of a sensor on a Kapton substrate. b1) A layer stack deposited on a flexible Kapton substrate. b2) MI sensor strip of 22 mm 1.5 mm after patterning. c) Picture of the flexible MI sensor mounted on the sample holder. d) Schematic of the high-frequency microstrip-based curvature measurement setup for the flexible magnetic sensor [13].

subscript f and s refer to the film and the substrate respectively. The value of α can vary from -1 for a rigid substrate to 1 for a compliant substrate. All the studies made in the PhD concern systems whose Dundurs parameter is comprised between 0.9 and 1. In these cases, a small effort applied to the system lead to high stresses in the thin film.

These stresses may have an important effect on the static and dynamic magnetic properties, especially on the resulting magnetic anisotropy of thin films on polymer substrates. The involved phenomena can be the magnetoelasticity (inverse magnetostriction effect), but also the multifissuration that occurs in thin film uniaxially strained that may modify the magnetization distribution in the film (shape anisotropy). Concerning the magnetoelastic effects, these are little known for the most fashionable spintronics materials (such as full Heusler alloys Co_2FeAl or ferromagnetic amorphous alloys CoFeB that must also be used in flexible systems. Therefore, the experimental determination of magnetostriction coefficients of such alloys is of significant importance. However, the techniques allowing such estimations are rare for thin films.

Recently, a few techniques dedicated to thin films have been developed, such as magnetoelastic measurement setup with a Magneto-Optical Kerr Effect (MOKE) magnetometer [15, 8], substrate deflection method under magnetic field [17], laser Doppler vibrometry [18], MOKE with applied whole wafer curvature [19], strain modulated ferromagnetic resonance[20], or vibrating sample magnetometer coupled with bending [21].

Concerning measurements for flexible substrates, the first works have been made Ludwig *et al.* ($Fe_{50}Co_{50}$, $Co_{80}B_{20}$, Fe–Co–B–Si on polyimide substrates) by bending the samples in a high-frequency permeameter [22]. The change in permeability as a func-

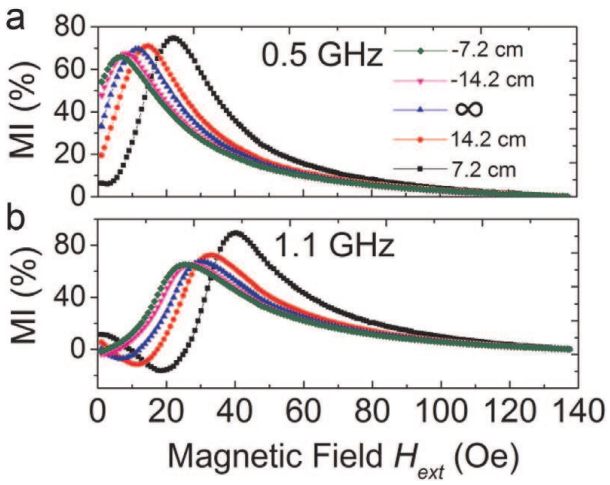

Figure 0.0.5 – MI ratio of the sample under different bending levels at (a) 0.5 GHz and (b) 1.1 GHz [13].

tion of applied strain is directly related to the magnetostriction coefficient. The slight difficulty is that the relationship between the two parameters is not linear, as shown in figure 0.0.6.

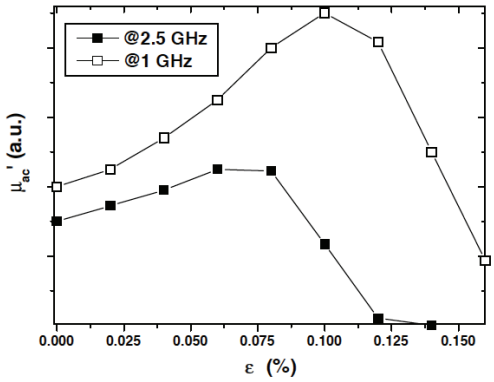

Figure 0.0.6 – Change of the permeability as a function of applied tensile strain for a positive magnetostrictive multilayer (FeCo(2.1 nm)/CoB(0.9nm)) thin film on polyimide [22].

Uhrmann *et al.* have made first experiments using MOKE and *in situ* tensile tests on thin films (CoFe/Cu/CoFe GMR system) deposited on polyimide substrate, showing clearly strain influence on hysteresis loops (see figure 0.0.7), but without estimating magnetostriction parameters[7].

Ozkaya *et al.* [8] have proposed to estimate magnetostriction coefficient of Co/Cu/Ni stacks from GMR curves and MOKE curves recorded during tensile tests. The estimation of magnetostriction coefficient λ in each magnetic layer (Co and Ni) has been made by introducing the magnetoelastic energy in the micromagnetic model proposed by H. Holloway and D. J. Kubinski [23]. The fits of the simulations to the experimental curves are shown in figure 0.0.8. However, very low values were found as compared to bulk

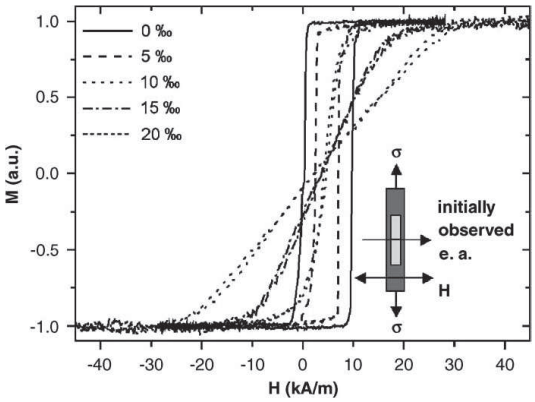

Figure 0.0.7 – Minor loop of the free-layer magnetization in unstrained state and under four different strain levels: 0% (solid line), 0.5% (dashed line), 1% (dotted line), 1.5% (dash dotted line), 2% (short dashed line) [7].

counterparts (1.75×10^{-6} for Cobalt instead of 60×10^{-6} and -0.4×10^{-6} for Nickel instead of -30×10^{-6}). Size effect on magnetoelastic behavior are evoked in the paper. These last exists for very thin layers (a few nanometers) but it seems also that the proposed analysis for heterogeneous stacks is not straightforward and the interlayer exchange coupling energy is not taken into account in the model.

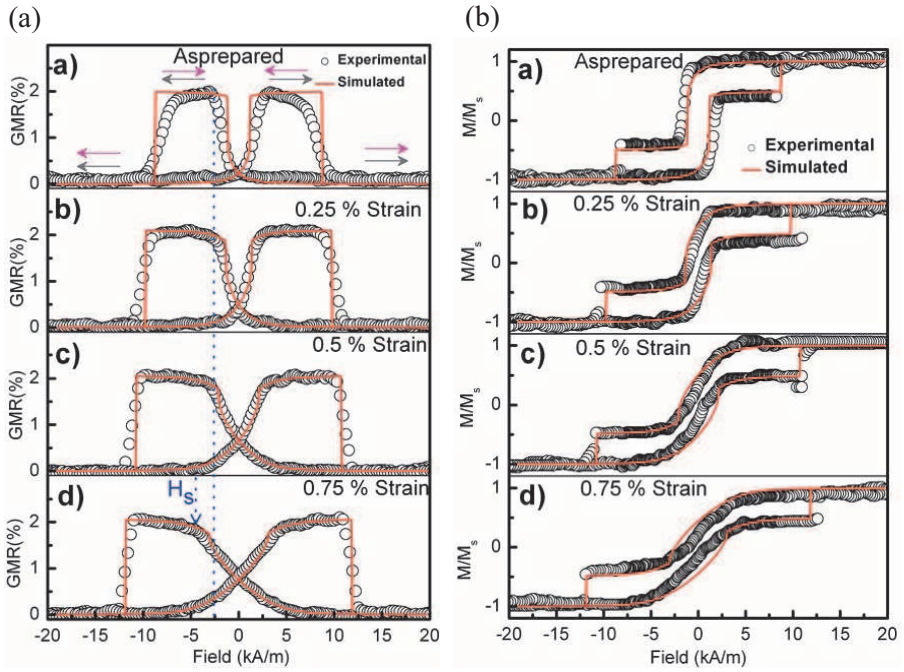

Figure 0.0.8 – Experimental and calculated curves for Co (8 nm)/Cu (4.2 nm)/Ni (8 nm) GMR systems for 4 different applied strains (0%, 0.25%, 0.5% and 0.75%) [8]. (a) GMR curves and (b) MOKE curves.

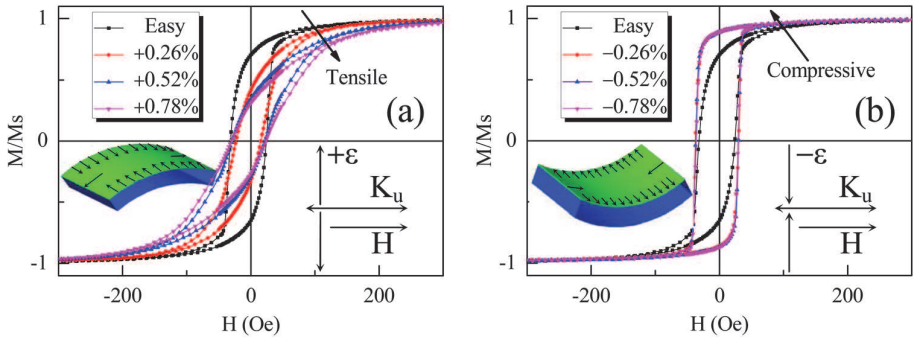

Figure 0.0.9 – Hysteresis loops for $Fe_{81}Ga_{19}$/ PET obtained under various external strains using different measuring configurations, (a) Magnetic field H perpendicular to the tensile strain (outward bending of PET substrates), (b) H perpendicular to the compressive strain (outward bending of PET substrates) [16].

Dai *et al.* [16] have investigated on magnetic properties of magnetostrictive $Fe_{81}Ga_{19}$ films grown on flexible polyethylene terephthalate (PET) substrates under various mechanical strains by combining MOKE measurements and *in situ* bending. The hysteresis loops were measured under various compressive or tensile strains by inward or outward bending of the films, as shown in figure 0.0.9. They showed that the easy axis can be tuned to the hard axis or vice versa by analyzing the magnetization curves with the Stoner-Wohlfarth model, including magnetoelastic anisotropy contribution. This contribution being proportional to the magnetostriction coefficient λ and to the uniaxial stress σ, they were able to identify/estimate $\lambda = 100 \times 10^{-6}$ in this alloy (know to show high magnetostriction value for this composition). Moreover, they showed that a uniaxial magnetic anisotropy K_u is present for each film deposited on flexible substrates, which is interpreted by inevitable slight deformations of the system. This point will be discussed later in the manuscript (chapter 5).

Among the techniques probing magnetization in thin films, FMR-based ones are the more pertinent for the targeted applications, since it allows measuring static (anisotropies, saturation magnetization, ...) and dynamic (damping effect, microwave properties, ...) magnetic properties. Weiler *et al.* [24] have used broadband FMR to quantify the effect of an electric field on magnetic anisotropy of Ni thin films deposited directly on a piezoelectric actuator. The piezoelectric actuator deforms upon the application of a voltage V_p. Due to its elasticity, an elongation (or contraction) along one direction is always accompanied by a contraction (or elongation) in the two orthogonal directions. Therefore, for $V_p > 0$, the actuator expands along its dominant elongation axis (here $\hat{y}$) and contracts along the two orthogonal directions (and conversely for $V_p > 0$), as shown in figure 0.0.10.

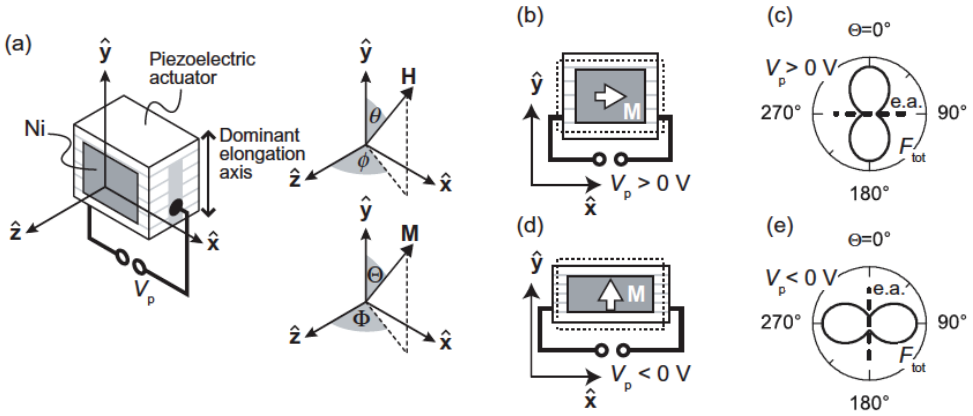

Figure 0.0.10 – a) Schematic illustration of the ferromagnetic thin film/piezoelectric actuator hybrid. b), d) The application of a voltage $V_p \neq 0$ V to the actuator results in a deformation of the actuator and the affixed ferromagnetic film. The relaxed actuator at $V_p = 0$ V is shown by dotted contours. c), e) Schematic free energy contours in the film plane. The magnetic easy axis (e.a.) shown by the thick dashed line is oriented parallel to the compressive strain and can thus be rotated by 90° by changing the polarity of V_p [24].

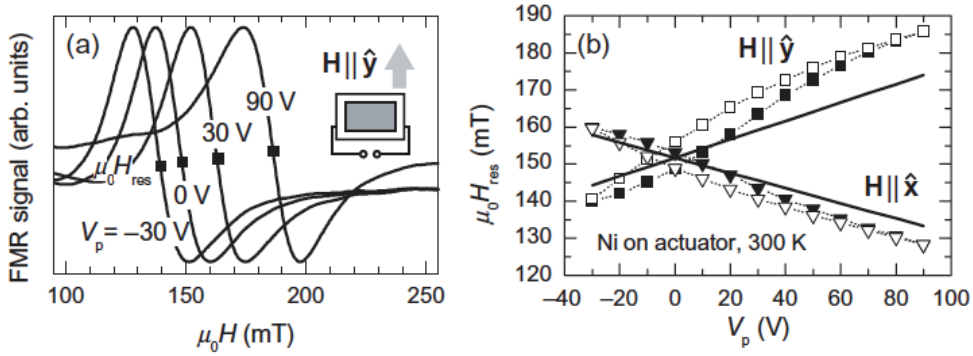

Figure 0.0.11 – a) FMR spectra recorded at different voltages V_p. b) The dependence of resonance field on V_p for two perpendicular configuration (longitudinal strain parallel or perpendicular to **H**) [24].

As Ni is directly deposited onto the actuator, the elastic strains are well transmitted to the thin films. Hence, thin film magnetoelastic properties can induce a rotation of the easy axis for the magnetization. Experimentally, this is traduced by shifts of FMR spectra (figure 0.0.11) and a change in the angular dependance of the resonance, as illustrated in figures 0.0.10-c) and 0.0.10-e).

Experimental study of the magnetic anisotropy for different applied voltages are shown in figure 0.0.12. The angular dependance of the resonance field is strongly affected by the elastic strains induced by applied voltage. These results demonstrate that a piezoelectric actuator allows to modify the magnetic anisotropy of a ferromagnetic thin film, enabling a voltage control of magnetization orientation. The possibility to orient the main elongation

axis of the actuator along any given direction in the film plane opens a pathway for the investigation of the magnetoelastic properties of ferromagnetic thin films under tunable stress. We will see in the present manuscript that it is possible to tailor magnetization of thin films deposited on polymer substrates using this approach.

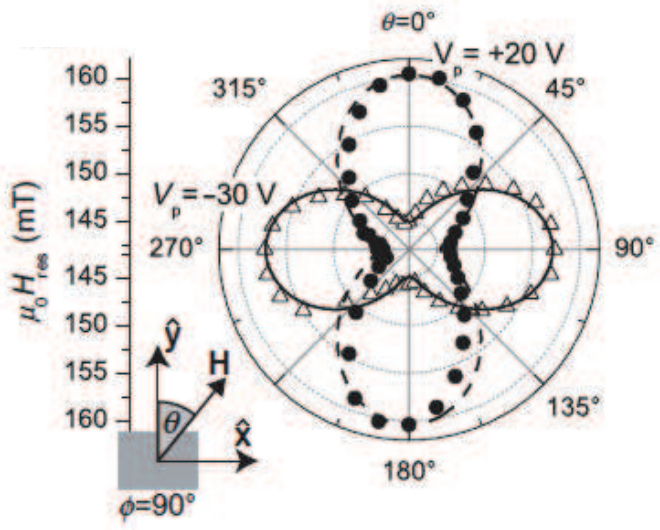

Figure 0.0.12 – Angular dependance of the resonance field for two applied voltages ($V_p = -30$ V and $V_p = +20$ V) [24].

Objectives The goal of this thesis is the investigation of the magneto-mechanical properties of ferromagnetic thin films deposited on flexible substrates. It is known regardless of the deposition process employed, that thin films on flexible substrates are the seat of intrinsic stresses, either tensile or compressive. In addition to these built-in stresses, thin films are subjected to stress during use, which affect their functional properties. In order to scrutinize the strain and stress effects on magnetization distribution in full Heusler alloys Co_2FeAl or ferromagnetic amorphous alloys CFB, a combination of *in situ* broadband ferromagnetic resonance, mechanical testing (bending or piezoactuation) and strain measurements (Digital Image Correlation) has been developed. A whole analytical formalism has been written to take into account of the involved phenomena (ferromagnetic resonance, residual and applied stress state, resulting anisotropy field, ...). Applied and residual stress effects on magnetic properties of the thin film alloys cited above deposited on flexible substrate have been studied. Moreover, this thesis has also explored the effect of the annealing temperature on the elastic and magnetoelastic properties of ferromagnetic amorphous films CFB, in order to estimate the potentialities of this material for applications in flexible spintronics .

Thesis organization We begin the thesis with a general overview of the field and the evolution of the technology. Then, we briefly introduce basic concepts in magnetism (in chapter 1) and elasticity (in chapter 2) generally necessary for the understanding of the performed experiments. Thereafter, the employed experimental methods in the framework of this thesis project will be described in chapter 3. Chapter 4 provides a methodology for the determination of the magnetostriction coefficients of magnetic thin film (non-

textured polycrystalline Ni (as model system), full Heusler alloys Co_2FeAl and ferromagnetic amorphous alloys CFB. Chapter 5 describes the origin of the unavoidable residual magnetic anisotropies in ferromagnetic thin films deposited on flexible substrates. Chapter 6discusses the effect of the annealing temperature on the magnetoelastic properties of CFB. Finally, in chapter 7, we will show how we can use ferromagnetic resonance in the frequency domain to follow the magnetization direction in thin film on flexible substrate.

Bibliography

[1] S. Kim, H. Y. Jeong, S. K. Kim, S.-Y. Choi, and K. J. Lee. Nano Letters 11, 5438–5442 (2011). (Cited on page 1.)

[2] M. Kaltenbrunner, M. S. White, E. D. Głowacki, T. Sekitani, T. Someya, N. S. Sariciftci and S. Bauer. Nature Communication 3, 770 (2012). (Cited on page 1.)

[3] L. Li, J. Liang, S.-Y. Chou, X. Zhu, X. Niu, Z. Yu, Q. Pei. Scientific Reports 4, 4307 (2014). (Cited on page 1.)

[4] S. Das, R. Gulotty, A. V. Sumant, A. Roelofs. Nano Letters 14, 2861–2866 (2014). (Cited on page 1.)

[5] H.C. Ko, G. Shin, S.D. Wang, M.P. Stoykovich, J.W. Lee, D.H. Kim, J. S. Ha, Y. Huang, K.-C. Hwang, J.A. Rogers, Small 5, 2703 (2009) (Cited on pages iv, 1 and 2.)

[6] D. Makarov, M. Melzer, D. Karnaushenko, and O. G. Schmidt, Applied Physics Review 3, 011101 (2016) (Cited on page 1.)

[7] T. Uhrmann, L. Bar, T. Dimopoulos, N. Wiese, M. Ruhrig, A. Lechner, J. Magn. Magn. Mater. 307, 209 (2006) (Cited on pages iv, 1, 5 and 6.)

[8] B. Ozkaya, S.R. Saranu, S. Mohanan, U. Herr, Phys. Stat. Sol. A 205, 1876 (2008) (Cited on pages iv, 1, 5 and 6.)

[9] C. Barraud, C. Deranlot, P. Seneor, A. Mattana, B. Dlubak, S. Fusil, K. Bouzehouane, D. Deneuve, F. Petroff, A.Fert, Appl. Phys. Lett. 96, 072502 2010 (Cited on page 1.)

[10] M. Melzer, M. Kaltenbrunner, D. Makarov, D. Karnaushenko, D. Karnaushenko, T. Sekitani, T. Someya, O. G. Schmidt, Nature Communication 6, 6080 (2015). (Cited on page 2.)

[11] N. Münzenrieder, D. Karnaushenko, L. Petti, G. Cantarella, C. Vogt, L. Büthe D. D. Karnaushenko, O. G. Schmidt, D. Makarov, and G. Tröster, Advanced Electronic Materials 2, 1600188 (2016) (Cited on page 2.)

[12] LA. Bedoya-Pinto, M. Donolato, M. Gobbi, L. E. Hueso and P. Vavassori, Applied Physics Letters, 104(6), 062412 (2014). (Cited on pages iv, 2 and 3.)

[13] B. D. Li, M. N. Kavaldzhiev, and J. Kosel, J. Magn. Magn. Mater. 378, 499 (2015). (Cited on pages iv, 2, 4 and 5.)

[14] R. Bonin, M.L. Schneider, T.J. Silva, J.P. Nibarger, J. Appl. Phys. 98, 23904 (2005). (Cited on page 3.)

[15] I. G. Will, A. Ding, and Y. B. Xu, Rev. Sci. Instrum. 83, 064707 (2012). (Cited on page 4.)

[16] G. Dai, Q. Zhan, Y. Liu, H. Yang, X. Zhang, B. Chen, and R.-W. Li, Applied Physics Letters 100, 122407 (2012) (Cited on pages v and 7.)

[17] W. Brückner, C. Lang and C. M. Schneider, Rev. Sci. Instrum. 72, 2496 (2001). (Cited on page 4.)

[18] R. Varghesea, R. Viswanb, K. Joshia, S. Seifikarc, Y. Zhoua, J. Schwartzc, and S. Priyaa, J. Mag. Mag. Mater. 363, 179–187 (2014). (Cited on page 4.)

[19] C. B. Hill,W. R. Hendren, R.M. Bowman, P. K. McGeehin,M. A. Gubbins, and V. A. Venugopal, Meas. Sci. Technol. 24, 045601 (2013). (Cited on page 4.)

[20] K. Nesteruk, R. Zuberek, S. Piechota, M. W. Gutowski, and H. Szymczak, Meas. Sci. Technol. 25, 075502 (2014). (Cited on page 4.)

[21] B. Buford, P. Daghat, and A. Jander, J. Appl. Phys. 115, 17E309 (2014). (Cited on page 4.)

[22] A. Ludwig, M. Tewes, M. Glasmachers, M. Löhndorf, E. Quandt, J. Magn. Magn. Mater. 242-245, 1126 (2002) (Cited on pages iv, 4 and 5.)

[23] H. Holloway and D. J. Kubinski, Journal of Applied Physics 83, 2705 (1998) (Cited on page 5.)

[24] M. Weiler, A. Brandlmaier, S. Geprägs, M. Althammer, M. Opel, C. Bihler, H. Huebl, M. S. Brandt, R. Grossand S. T. B. Goennenwein, New Journal of Physics 11, 013021 (2009)

(Cited on pages v, 7, 8 and 9.)

1 Fundamental concepts in magnetism

This chapter is dedicated to the introduction of magnetic mechanisms that are relevant in the framework of this thesis. First of all, the magnetic interactions and the magnetic anisotropies effects which are important to be understood by the reader. Thereafter, the microscopic and macroscopic behaviors of the magnetization under the influence of an external perturbation. Before presenting the experimental techniques employed in this thesis, we will gives the theoretical description magnetization dynamics and the resulting magnetic excitations uniform mode precession of the magnetization and spin waves and some relaxation mechanisms we encountered in the study of ferromagnetic thin films.

1.1 Magnetic interactions

In this section, we will outline the origin of magnetic interactions by emphasizing ferromagnetic ordering, since ferromagnets are the main subject of this thesis. We will show that the magnetic dipolar interaction is too weak to be responsible of the ferromagnetism.The ferromagnetism is classically explained by quantum mechanical effect; indeed, it is the exchange interactions which is the cause of magnetism in metals. Therefore, we will show that the exchange interaction can be splitted into two different class: direct and indirect interactions, respectively.

1.1.1 Magnetic dipolar interaction

The energy of two magnetic dipoles $\vec{\mu_1}$ and $\vec{\mu_2}$ separated by the vector $\vec{r}$ is given by:

$$E = \frac{\mu_0}{4\pi r^3}\left(\vec{\mu_1}.\vec{\mu_2} - \frac{3}{r^2}\left(\vec{\mu_1}.\vec{r}\right)\left(\vec{\mu_2}.\vec{r}\right)\right) \tag{1.1.1}$$

The dipolar energy is long-range interaction and thus depends on their distance and relative orientations. For an estimation of this energy we choose typical values with $\mu_1 = \mu_2 = 1\mu_B$ (where μ_B is the Bohr magneton) and $r = 2$Å. Additionally, assuming $\vec{\mu_1} \uparrow\uparrow \vec{\mu_2}$ and $\mu \uparrow\uparrow \vec{r}$ leads to an energy:

$$E = \frac{\mu_0 \mu_B^2}{2\pi r^3} = 2.1 \times 10^{-24} J \approx 10^{-6} eV \tag{1.1.2}$$

The corresponding temperature ($E = k_B T$ with k_B the Boltzmann constant) is far below 1K. But, the order temperature, otherwise the Curie temperature T_C of ferromagnetic materials can reach up to 1000 K (for instance the Curie temperature of Co_2FeAl Heusler alloys studied in this research project is approximatively $T_C \sim 1000$ K). Therefore, the magnitude of the magnetic dipole interaction is too weak to cause a ferromagnetism order.

1.1.2 Exchange interactions

The exchange interaction is the interaction responsible for the establishment of magnetic order in magnetic materials, parallel alignment of spins i.e ferromagnetic, antiparallel alignment of spins i.e ferrimagnetic, etc. This interaction arises from a quantum mechanical effect with no classical analogue, due to the indistinguishability of electrons. The exchange interaction can be splitted into two types of interactions (direct and indirect exchange) according to the distance between the magnetic moments. When the electrons of neighboring magnetic atoms directly interact, this interaction is called direct exchange because it is done without the mediation of intermediate atoms. In the case of indirect exchange, the involved wave functions are weakly overlapped (for rare earth metal atoms with their localized $4f$ electrons) then the direct exchange does not represent the dominating mechanism for magnetic properties. For this class of systems the indirect exchange interaction is responsible for magnetism.

1.1.2.1 Direct exchange

The direct exchange as previously introduced arises from a direct overlapping of electronic wave functions of the contiguous atoms. The electrons that belong to those wave functions are indisguishables. Because the electrons are fermions, the Pauli exclusion principle must be fulfilled. As a consequence, the wave function is then antisymmetric. The exchange interaction can expressed in the sample case of two electrons by an effective hamiltonian H_{spin} which is given in the Equation .

$$H_{spin} = -2J\vec{S_1}.\vec{S_2} \tag{1.1.3}$$

where $\vec{S_1}$ and $\vec{S_2}$ are the angular spin momentum vector of atoms in the i and j sites. J is the exchange constant or the exchange integral. To be more general, atoms in solids are constituted of many electrons, the exchange energy in the case of many-body systems is then given within the Heisenberg model by the Hamiltonian:

$$H = \sum_{ij} J_{ij}\vec{S_i}.\vec{S_j} \tag{1.1.4}$$

with J_{ij} being the exchange constant between i and j spins. The factor 2 is included in the double counting within the sum. Often a good approximation is given by:

$$J_{ij} = \begin{cases} J & \text{for nearest neighbor spins} \\ 0 & \text{otherwise} \end{cases} \tag{1.1.5}$$

The sign of the exchange integral describes the alignment of spins. For example, if $J > 0$, the interaction favors parallel alignment of the spins, which corresponds to ferromagnetic ordering. If $J < 0$, an antiparallel (i.e antiferromagnetic) alignment occurs. Moreover, it is correlated to the ratio a/r, with a being the interatomic distance and r the radius of the $d-$shells. Bethe-Slater give the graphical illustration of such behavior (see figure 1.1.1). As we can see, this curve allows to distinguish between ferromagnetic $3d$ elements like Fe, Co and Ni exhibiting a parallel alignment and thus a positive exchange constant and antiferromagnetic elements like Mn and Cr with an antiparallel orientation of the magnetic moments and therefore a negative exchange constant[2, 3, 4].

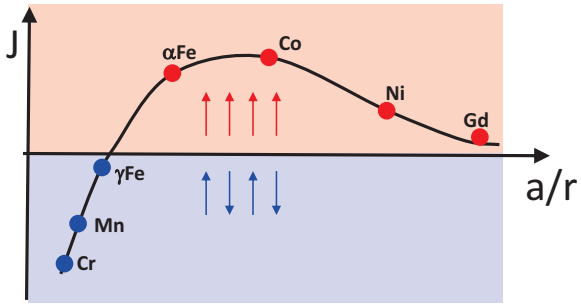

Figure 1.1.1 – Bethe–Slater curve: elements above the horizontal axis are ferromagnetic, below the axis are antiferromagnetic. a corresponds to the interatomic distance and r is the radius r of the $3d$ electron shell.

1.1.2.2 Indirect exchange

It exists different class of indirect exchange depending on the magnetic material. In the following, we present the main known ones.

Superexchange Super exchange arises frequently in transition metal oxides where the 3d magnetic ions are separated by non-magnetic oxygen ions. Thus there is no direct overlap between d orbitals of magnetic ions; the interaction is indirect and occurs because d orbitals hybridize with p orbitals of oxygen ions; Let's consider 2 magnetic ions $M1$ and $M2$ separated by an oxygen ion O, d electrons are partially delocalized on oxygen and the delocalization energy is different according to magnetic moment configurations i.e parallel or antiparallel (see figure 1.1.2-left). It is the most common magnetic interaction in insulators, e.g. La_2CuO_4, MnO, MnF_2, NiO, etc. The sign and value of this super exchange interaction depends on the number of electrons, of the type of d orbitals involved, and on the angle M1-O-M2. It is most often negative, leading to antiferromagnetic interaction as in MnO for instance, but it can be positive as in EuO. Finally it is always a short range interaction because it involves hybridization between neighboring ions, M and O.

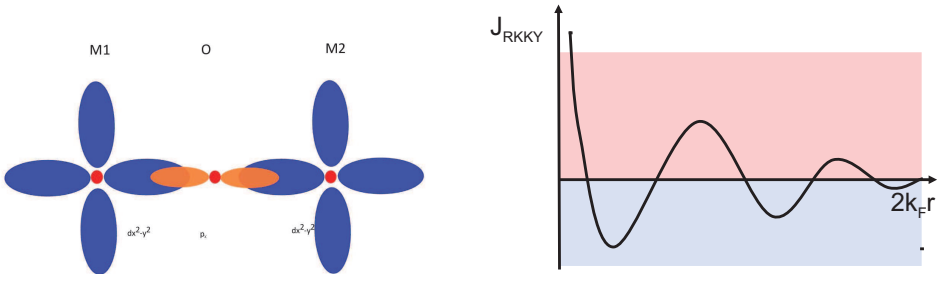

Figure 1.1.2 – Left: Illustration of the indirect magnetic exchange interaction between anion-mediated magnetic cations. Right: Variation of the indirect exchange coupling constant, J_{RKKY}, of a free electron gas in the neighborhood of a point magnetic moment at the origin $r = 0$.

RKKY exchange interaction The indirect exchange couples moments over relatively large distances. It is the dominant exchange interaction in metals, where there is little or no direct overlap between neighboring electrons. It therefore acts through an intermediary, which in metals are the conduction electrons (itinerant electrons). This type of exchange is better known as the RKKY interaction named after Ruderman, Kittel, Kasuya and Yoshida [5, 6, 7]. The RKKY exchange is a long-range interaction contrary to direct exchange, the RKKY coefficient J_{RKKY} which is given by oscillates from positive to negative as the separation of the ion changes and has the damped oscillatory nature shown in figure 1.1.2-right.

1.2 Magnetic anisotropy effects

When the physical properties of a material depend on the direction in which they are measured, these properties are said to exhibit anisotropy. In the case of ferromagnets which are the materials studied in this research project, the preference for the magnetization to lie in a particular direction in a sample is called magnetic anisotropy. The magnetic anisotropies can arise from the sample shape, crystal symmetry, stress or directed atomic pair ordering. There are two main microscopic origins of magnetic anisotropy. We distinguish between magnetic anisotropy due to spin orbit coupling (SOC) as compared to magnetic anisotropy of dipolar origin. The former includes magnetocrystalline, magnetoelastic anisotropy; the latter explained in subsection 1.1.1 is responsible of shape anisotropy. Phenomenologically speaking, the anisotropy effects are described in term of free energy density per unit volume that has the same symmetry than the crystal structure of the material. This kind of anisotropy is called magnetocrystalline anisotropy. Anisotropy is of considerable practical importance because it is exploited in the design of most magnetic materials for spintronics applications..

1.2.1 Magnetocrystalline anisotropy

The magnetocrystalline anisotropy referred to dependance of the spontaneous magnetization on the crystal structure. The magnetocrystalline anisotropy is a consequence of the spin-orbit interaction. As consequence the magnetization of a material prefers to align along a well-defined crystallographic axis to minimize its internal energy. The directions in which the magnetization lies to minimize the energy are called easy axis. An energy term is used to describes this kind of magnetic anisotropy, it is called magnetocrystalline energy.

1.2.1.1 Uniaxial anisotropy

In a material with a uniaxial (hexagonal and tetragonal) symmetry, the uniaxial anisotropy energy can be phenomenologically described by a series expansion. Let us consider Co material which crystallizes in a hexagonal structure, it presents a uniaxial anisotropy with an easy axis of magnetization parallel to the $z-$axis (otherwise $c-$axis) of the crystal. A rotation of the magnetization away from the easy axis, increases the free energy density reaching a maximum value at $\theta = 90°$, where θ is the angle between $z-$axis and the magnetization vector, with a 180° periodicity of oscillation before returning to its

initial value at θ=180°. The free energy density of a material with uniaxial (hexagonal, tetragonal) symmetry is expressed with a power series expansions[1, 2, 3, 8, 9, 11] :

$$F_u = \frac{F_0}{V_0} = \sum_n K_{un} \sin^{2n} \theta \tag{1.2.1}$$

Then, expanding the free energy F_u in the equation 1.2.1 leads to equation 1.2.2:

$$F_u = K_{u1} \sin^2(\theta) + K_{u2} \sin^4(\theta) + K_{u3} \sin^4(\theta) \cos(4\varphi) \tag{1.2.2}$$

The coefficients K_{un} (n= 1, 2, 3) are the anisotropy coefficients and $\varphi$is the angle between direction of the spontaneous magnetization and $x-$axis. The higher order terms are small and their values are not always measurable. In the case of a hexagonal or tetragonal crystal structure in which the term K_{u1} predominates and is positive, the magnetization will lie along the easy which correspond to the $z-$axis. In other words, the magnetization is stable in that direction. Such an axis is referred to the magnetization easy axis or simply easy axis. The magnetization will be along in the direction perpendicular to the $z-$axis if $K_{u1} < 0$, so the magnetization is in an unstable state in this situation and its energy is maximum. Such axis are called hard axis of magnetization or simply hard axis. However, if $K_{u1}$is not preponderant the magnetization will be in others directions. We can plot a diagram showing the magnetization directions in a hexagonal crystal for different values of the anisotropy constants $K_{u1}$and K_{u2}. For this, lets take the following situation:

$$K_{u1} > 0 \quad and \quad K_{u1} + K_{u2} > 0. \tag{1.2.3}$$

in these considerations the minimum of the anisotropy is reached when $\theta = 0$, whereas if

$$K_{u1} > 0 \quad and \quad 2K_{u2} > -K_{u1}. \tag{1.2.4}$$

the minimum of the energy is obtained when θ is equal to:

$$\theta = -\frac{K_{u1}}{2K_{u2}} \tag{1.2.5}$$

1.2.1.2 Cubic anisotropy

The anisotropy energy for cubic crystal such as Fe or Ni is formulated in term of direction of cosines $\vec{m} = \frac{\vec{M}}{M} = (\alpha_1, \alpha_2, \alpha_3)$ of the magnetization vector with respect to the cubic edges. However, the given expression of the anisotropy must respect the crystal symmetry. The anisotropy energy must be compatible with the symmetry group of the crystal by remaining unchanged under all operations. The magnetocrystalline anisotropy for cubic crystals is generally written in the form proposed by Akulov (see equation 1.2.6) [1, 10, 11, 22], i.e a polynomial series of α_1, α_2 and α_3.Those terms which include the odd powers of α_i, must vanish, because a change in sign of any of the α_i, should bring the magnetization vector to a direction which is equivalent to the original direction. Moreover, the expression must be invariant to interchange of two α_i so that the terms

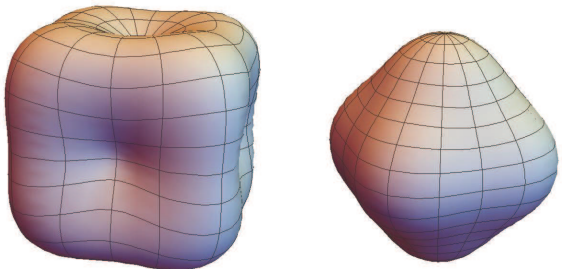

Figure 1.2.1 – First order anisotropy energy surface for iron cubic crystal for a positive K_{u1} (left) and negative K_{u1} (right) anisotropy coefficient.

$\alpha_i^{2l}\alpha_j^{2m}\alpha_k^{2n}$, must have for any combination of l, m and n the same coefficient than any interchange of i, j and k. Therefore, the terms should be in the form $\alpha_1^2 + \alpha_2^2 + \alpha_3^2 = 1$

$$F_c = K_{u1}\left(\alpha_1^2\alpha_2^2 + \alpha_2^2\alpha_3^2 + \alpha_3^2\alpha_1^2\right) + K_{u2}\left(\alpha_1^2\alpha_2^2\alpha_3^2\right) + K_{u3}\left(\alpha_1^2\alpha_2^2 + \alpha_2^2\alpha_3^2 + \alpha_3^2\alpha_1^2\right)^2 + \dots \tag{1.2.6}$$

Where the direction cosines can be given:

$$\left(\ \alpha_1,\quad \alpha_2,\quad \alpha_3\ \right) = \left(\ \sin(\theta)\cos(\varphi),\quad \sin(\theta)\sin(\varphi),\quad \cos(\theta)\ \right) \tag{1.2.7}$$

We can replace this relation (equation 1.2.6) and limiting ourselves to the first order of the anisotropy energy:

$$F_c = K_{u1}(\sin^4\theta\cos^2\varphi\sin^2\varphi + \sin^2\theta\cos^2\theta) \tag{1.2.8}$$

We can see in figure 1.2.1 the 3D representations of the cubic anisotropy for $K_{u1} > 0$ and $K_{u1} < 0$. If K_{u1} is positive, the easy axis (minima of the energy) are along the $< 100 >$ direction i.e along the cube axes. The energy minima is along $< 111 >$ directions i.e along the diagonal of the of the cube if $K_{u1} < 0$.

1.2.2 Shape anisotropy

A magnetized body has at its surface "free poles" that arise where the normal component of the magnetization $\vec{M}$ goes through a discontinuity. These “free poles” with a volume density $\rho = -\nabla\vec{M}$ and surface density $\sigma = \vec{M}.\vec{n}$ (where $\vec{n}$ is the normal vector) create a demagnetizing field $\vec{H}_d$ which opposes to the magnetization direction. If the magnetization is uniform, then only the surfaces carry some “free poles” since $\nabla\vec{M} = 0$. Thus, the intensity of the demagnetizing field $\vec{H}_d$ is proportional to the value of the magnetization $\vec{M}$:

$$\vec{H}_d = -\overleftrightarrow{N}\vec{M}$$

Where $\overleftrightarrow{N}$ is the demagnetizing tensor. The resulting free magnetic energy can be written as:

$$F_{dipolar} = \frac{1}{2}\vec{M}\overleftrightarrow{N}\vec{M} \tag{1.2.9}$$

Let us consider the case of a prolate ellipsoid object, the components $\overleftrightarrow{N}$ along the axes that coincides to the semi-axes of the ellipsoid N_x, N_y, N_z are called the demagnetizing

factors. The demagnetizing tensor is symmetric and becomes in the axes that coincides with the axes of the ellipsoid and is given by:

$$\overleftrightarrow{N} = \begin{pmatrix} N_x & 0 & 0 \\ 0 & N_y & 0 \\ 0 & 0 & N_z \end{pmatrix} \tag{1.2.10}$$

The trace of the demagnetizing tensor $\overleftrightarrow{N}$ satisfies $N_x+N_y+N_z = 4\pi$. For an arbitrary direction of the magnetization with respect to the semi-axes of the ellipsoid, characterized by the direction cosines of the magnetization α_x,α_y, α_z, the free energy density is given by:

$$F_{dip} = \frac{1}{2}M^2\left(N_x\alpha_x^2 + N_y\alpha_y^2 + N_z\alpha_z^2\right) \tag{1.2.11}$$

We can venture to calculate the dipolar free energy density for different geometries; the sphere, a spheroid, an infinitely long cylinder and for a thin film. In the case of a sphere, the tensor $\overleftrightarrow{N}$ amounts to:

$$\overleftrightarrow{N} = \begin{pmatrix} 4\pi/3 & 0 & 0 \\ 0 & 4\pi/3 & 0 \\ 0 & 0 & 4\pi/3 \end{pmatrix} \tag{1.2.12}$$

and the free energy density is given by:

$$F_{dip} = \frac{1}{2}M^2\frac{4}{3}\pi\left(\alpha_x^2 + \alpha_y^2 + \alpha_z^2\right) = \frac{2}{3}\pi M^2 \tag{1.2.13}$$

thanks to the normalization of the direction cosine $\alpha_x^2+\alpha_y^2+\alpha_z^2 = 1$. Thus, for a sphere which is isotropic, all the directions are energetically equivalent. For a spheroid the axes x and y otherwise called semi-minor axes are equal in length ($x = y$) but different to the $z-$axis (semi-major axis). As a consequence, the demagnetizing factor $N_x = N_y$ and $N_z = 4\pi - 2N_x$. The free energy density in this case is given by:

$$F_{dip} = \frac{1}{2}M^2\left(N_x\sin^2\theta\cos^2\varphi + N_y\sin^2\theta\sin^2\varphi + (4\pi - 2N_x)\cos^2\theta\right) \tag{1.2.14}$$

$$F_{dip} = \frac{1}{2}M^2\left(N_x + (4\pi - 3N_x)\cos^2\theta\right) \tag{1.2.15}$$

For an infinitely long cylinder, we have $x = y$ and , the demagnetizing tensor is given by:

$$\overleftrightarrow{N} = \begin{pmatrix} 2\pi & 0 & 0 \\ 0 & 2\pi & 0 \\ 0 & 0 & 0 \end{pmatrix} \tag{1.2.16}$$

The free energy density is given density amounts to:

$$F_{dip} = \frac{1}{2}M^2\frac{2\pi}{2}\left(\sin^2\theta\cos^2\varphi + \sin^2\theta\sin^2\varphi\right) = \frac{1}{2}\pi M^2\sin^2\theta \tag{1.2.17}$$

For thin films as is discussed in that framework of this thesis, all the demagnetizing vanishes except the one for the direction perpendicular to the film. The demagnetizing tensor is given by:

$$\overleftrightarrow{N} = \begin{pmatrix} 0 & 0 & 0 \\ 0 & 0 & 0 \\ 0 & 0 & 4\pi \end{pmatrix} \tag{1.2.18}$$

and the free energy density is:

$$F_{dip} = 2\pi M^2 \cos^2\theta \tag{1.2.19}$$

1.2.3 Magnetoelastic anisotropy and magnetostriction

In addition to magnetocrystalline anisotropy, there is another effect related to spin-orbit coupling called magnetoelastic anisotropy. Magnetoelastic anisotropy arises from the strain dependence of the anisotropy constants. Upon magnetization, a previously demagnetized crystal experiences a strain that can be measured as a function of applied field along the principal crystallographic axes. A magnetic material will therefore change its dimension when magnetized (from ℓ to $\ell + \delta\ell$). The effect was first observed by Joule that bears his name, it is also called direct magnetostriction effect. A magnetostrictive strain coefficient λ can be introduced to describe this phenomenon: $\lambda = \frac{\delta\ell}{\ell}$. It should be noted that λ can take positive or negative values. Moreover, its sign can also change during the magnetization process. Furthermore, the magnetic field dependence of λ is not linear. The converse effect otherwise Villari effect, or the change of magnetization with stress also occurs[11]. The resulting magnetostrictive strains $\lambda = \frac{\delta\ell}{\ell}$ are about 10^{-6} for Fe[12] but can reach values as high as 10^{-3} for FeTb alloys[13]. For the sake of brevity, we will take the example of a cubic system. The magnitude of the magnetoelastic anisotropy is described by two magnetostriction coefficients (λ_{111} and λ_{100}), or by the magnetoelastic coupling coefficients (B_1, B_2) and the level of stress[14]. The magnetoelastic anisotropy for a cubic system is thus given by [1]:

$$\begin{aligned} F_{me} = {} & B_1\left(\alpha_1^2\varepsilon_1 + \alpha_2^2\varepsilon_2 + \alpha_3^2\varepsilon_3\right) \\ & + B_2\left(\alpha_2\alpha_3\varepsilon_4 + \alpha_1\alpha_3\varepsilon_5 + \alpha_1\alpha_2\varepsilon_6\right) + B_3(\varepsilon_1 + \varepsilon_2 + \varepsilon_3) \end{aligned} \tag{1.2.20}$$

The direction cosines of the magnetization with respect to the cubic axes are given by α_i , the strains ε_i are measured along the cubic axes. Equation (1.2.20) describes how the magnetization direction interacts with the strains to result in a magnetoelastic energy density that is given by the so-called magnetoelastic coupling coefficients B_1 and B_2. The magnetoelastic energy is usually written as a function of the magnetostriction coefficients. For this, relations between the magnetostrictive strains, magnetoelastic coupling coefficients and elastic coefficients have to be defined. Indeed, the application of stress will deform the crystal until the magnetoelastic energy F_{me} is balanced by the elastic one F_{el} (see Chapter 2).

1. Note that contraction notations are used here (see chapter 2).

Magnetostriction in cubic single crystal

The equilibrium strains are obtained minimizing the total energy (F_{tot}), so here $F_{tot} = F_{me} + F_{el}$. Thus, the following equations are obtained:

$$\frac{\partial E_{tot}}{\partial \varepsilon_1} = C_{11}\varepsilon_1 + C_{12}(\varepsilon_2 + \varepsilon_3) + B_1\alpha_1^2 + B_3 = 0 \tag{1.2.21}$$

$$\frac{\partial E_{tot}}{\partial \varepsilon_2} = C_{11}\varepsilon_2 + C_{12}(\varepsilon_1 + \varepsilon_3) + B_1\alpha_2^2 + B_3 = 0 \tag{1.2.22}$$

$$\frac{\partial E_{tot}}{\partial \varepsilon_3} = C_{11}\varepsilon_2 + C_{12}(\varepsilon_1 + \varepsilon_3) + B_1\alpha_3^2 + B_3 = 0 \tag{1.2.23}$$

$$\frac{\partial E_{tot}}{\partial \varepsilon_4} = C_{44}\varepsilon_4 + B_2\alpha_2\alpha_3 = 0 \tag{1.2.24}$$

$$\frac{\partial E_{tot}}{\partial \varepsilon_5} = C_{44}\varepsilon_5 + B_2\alpha_1\alpha_3 = 0 \tag{1.2.25}$$

$$\frac{\partial E_{tot}}{\partial \varepsilon_6} = C_{44}\varepsilon_6 + B_2\alpha_1\alpha_2 = 0 \tag{1.2.26}$$

If equations 1.2.21, 1.2.22 and 1.2.23 are summed, a homogeneous expansion Δ is found. This expansion is independent of the direction cosines of the magnetization and corresponds to an elementary variation of the ferromagnets' volume.

$$\Delta = \varepsilon_1 + \varepsilon_2 + \varepsilon_3 = \frac{-B_1 + 3B_3}{C_{11} + 2C_{12}} \tag{1.2.27}$$

If we neglect this variation, we found that:

$$\varepsilon_{1,2,3} = \frac{-B_1\alpha_{1,2,3}^2}{C_{11} - C_{12}} - C_{12}\Delta \simeq \frac{-B_1\alpha_{1,2,3}^2}{C_{11} - C_{12}} \tag{1.2.28}$$

$$\varepsilon_{4,5,6} = \frac{-B_2\alpha_{2,1,1}\alpha_{3,3,2}}{C_{44}} \tag{1.2.29}$$

We then introduce the direction cosines (β_1, β_2 and β_3) between the cubic crystal and the crystallographic axis. The relative variation is given by:

$$\frac{\delta\ell}{\ell} = \sum_{i,j} \varepsilon_{ij}\beta_i\beta_j \tag{1.2.30}$$

The following relation is deduced:

$$\begin{aligned}\frac{\delta\ell}{\ell} = {} & \frac{-B_1}{C_{11} - C_{12}}\left(\alpha_1^2\beta_1^2 + \alpha_2^2\beta_2^2 + \alpha_3^2\beta_3^2 - \frac{1}{3}\right) \\ & + \frac{-B_2}{C_{44}}(\alpha_2\alpha_3\beta_2\beta_3 + \alpha_1\alpha_3\beta_1\beta_3 + \alpha_1\alpha_2\beta_1\beta_2)\end{aligned} \tag{1.2.31}$$

We found the well known magnetostrictive coefficients (λ_{100} and λ_{111}) as function of the coefficients B_1 and B_2 by evaluating the above equation when the crystal is respectively magnetized along $< 100 >$ and $< 111 >$:

$$\lambda_{100} = -\frac{2}{3}\frac{B_1}{C_{11} - C_{12}} \qquad \text{and} \qquad \lambda_{111} = -\frac{B_2}{3C_{44}}$$

Note that we can introduce λ_{100} and λ_{100} in equation 1.2.31:

$$\frac{\delta\ell}{\ell} = \frac{3}{2}\lambda_{100}\left(\alpha_1^2\beta_1^2 + \alpha_2^2\beta_2^2 + \alpha_3^2\beta_3^2 - \frac{1}{3}\right) + 3\lambda_{111}\left(\alpha_2\alpha_3\beta_2\beta_3 + \alpha_1\alpha_3\beta_1\beta_3 + \alpha_1\alpha_2\beta_1\beta_2\right) \tag{1.2.32}$$

Moreover, it is interesting to write the strains tensor:

$$\varepsilon = \frac{3}{2}\begin{pmatrix} \lambda_{100}(\beta_1^2 - \frac{1}{3}) & \lambda_{111}\beta_1\beta_2 & \lambda_{111}\beta_1\beta_3 \\ \lambda_{111}\beta_1\beta_2 & \lambda_{100}(\beta_2^2 - \frac{1}{3}) & \lambda_{111}\beta_2\beta_3 \\ \lambda_{111}\beta_1\beta_3 & \lambda_{111}\beta_2\beta_3 & \lambda_{100}(\beta_3^2 - \frac{1}{3}) \end{pmatrix} \tag{1.2.33}$$

Indeed, the magnetoelastic energy can be directly written as:

$$E_{me} = -\sigma : \varepsilon \tag{1.2.34}$$

As previously said, the magnetostriction coefficients are about 10^{-6} in 3d metals (Fe, Ni and Co). In Nickel single crystals, the two magnetostriction coefficients are negative ($\lambda_{100} = -51 \times 10^{-6}$ and $\lambda_{111} = -22,4 \times 10^{-6}$). The case of Fe is interesting because the coefficients are of opposite sign ($\lambda_{100} = 20 \times 10^{-6}$ and $\lambda_{111} = -20 \times 10^{-6}$).

Magnetostriction in isotropic polycrystalline films

Magnetic thin films deposited onto polymer substrates generally present a microstructure which is either isotropic or transversely isotropic. We will discuss the case of isotropic materials here. In this case, the magnetostriction is isotropic. If the film is magnetized (till saturation) along a macroscopic crystalline direction, the above tensor (equation 1.2.33) could be written as:

$$\varepsilon = \begin{pmatrix} \lambda & 0 & 0 \\ 0 & -\frac{\lambda}{2} & 0 \\ 0 & 0 & -\frac{\lambda}{2} \end{pmatrix} \tag{1.2.35}$$

This result shows that the longitudinal magnetostriction is twice time higher than the transverse one with an opposite sign. Furthermore, to find the value of this λ, it is interesting to use homogenization models initially developed for elastic coefficients calculation in polycrystalline films. The simplest ones are the Voigt and the Reuss models. In the Voigt approximation, the crystallites are considered as having the same deformation ε_0 (iso-strain), so the ensemble average is given $< \sigma >=< C\varepsilon >$ can be simplified to $< \sigma >=< C > \varepsilon_0$. As a consequence, the energy of each crystallites is expressed as a function of strain and the magnetization with the assumption of equal strain and minimization of the sum of all free energies with respect to strain. The following relation is then deduced:

$$\lambda = \left(\frac{C_{11} - C_{12}}{C_{11} - C_{12} + 3C_{44}}\right)\lambda_{100} + \left(1 - \frac{C_{11} - C_{12}}{C_{11} - C_{12} + 3C_{44}}\right)\lambda_{111} \tag{1.2.36}$$

Or by introducing the Zener anisotropy index $A = \frac{2C_{44}}{C_{11} - C_{12}}$

$$\lambda = \left(\frac{2}{2 + 3A}\right)\lambda_{100} + \left(\frac{3A}{2 + 3A}\right)\lambda_{111} \tag{1.2.37}$$

In Reuss approximation, the crystallites are considered to be the seat of the same stress σ_0 (iso-stress), a uniform stress through the crystallites is assumed. $< \epsilon >=< S\sigma_0 >$which can be simplified to $< \epsilon >=< S > \sigma_0$. Then, magnetostriction coefficient of an isotropic polycrystal is given in the Reuss approximation by: [15, 16]

$$\lambda = \frac{2}{5}\lambda_{100} + \frac{3}{5}\lambda_{111} \tag{1.2.38}$$

1.3 Magnetization Dynamics

The magnetization dynamics refers to time evolution of the macroscopic magnetization after thermal, electromagnetic (e.g. microwave) or even matter wave/particle (e.g. neutron, electron or phonon) excitations[17]. In magnetization dynamics, similarly to any other type of time evolution of a physical quantity, one has to consider the magnetic response in relation to the amplitude and energy spectrum of the excitation as well as the relaxation rates and likely different dissipation channels allowing the stored energy to dissipate to the lattice. A wide energetic range of excitations produced by time varying magnetic fields has been investigated in the frequency and time domain of spin dynamics. Depending on the amplitude of the excitation linear- and non-linear magnetic responses which are described by the field- and frequency-dependent magnetic susceptibility tensor χ can be monitored.

1.3.1 Landau Lifschitz Gilbert (LLG) equation

The dynamical process in ferromagnets are described using a continuum approach. Spins in ferromagnets are strongly coupled. For this, the magnetization ($\vec{M}=\frac{\sum\vec{\mu}}{V}$) which is the sum of magnetic moment per unit volume is used as a characteristic parameter of the ferromagnetic system. Thanks to this continuum approach, the classical theory can be used for the treatment of the dynamics process of the magnetization. However, the equations of macroscopic electrodynamics should be supplemented by materials characteristic equations, which describe the particular relation between the magnetization vector $\vec{M}$ and the magnetic field $\vec{H}$. Let us consider the ferromagnet medium as a sum of classical top with an angular momenta $\vec{J}$ and magnetic moment $\vec{\mu}$. From quantum-mechanics, we know that the magnetic moment is proportionally related to the angular moment as follows:

$$\vec{\mu} = \gamma\vec{J} \tag{1.3.1}$$

In this case, the equation of the top can be written as follows:

$$\hbar\frac{\partial\vec{J}}{\partial t} = \vec{\mu} \times \vec{H} \tag{1.3.2}$$

Using the relation $\vec{M} = N\vec{\mu}$ where N is the number of tops in a unit volume and the relation $\overrightarrow{\mu} = \gamma\overrightarrow{J}$, we obtain the equation of motion of the magnetization (equation 1.3.3) which was firstly proposed in 1935 by Landau and Lifschitz[18].

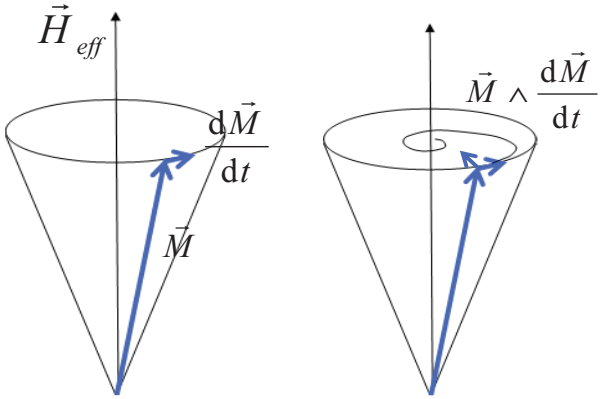

Figure 1.3.1 – When disturbing the equilibrium configuration, the magnetization $\vec{M}$ precesses around the effective magnetic field $\vec{H}_{eff}$ (left). The torque acting on the moment is given by equation 1.3.3. When introducing damping, the magnetization follows a helicoidal trajectory back to its equilibrium position (right), described by equation 1.3.4.

$$\frac{\partial \vec{M}}{\partial t} = -\gamma(\vec{M} \times \vec{H}_{eff}) \tag{1.3.3}$$

It is important to point out that this equation is only valid if the magnetization $\vec{M}$ is uniform and changes in space slowly. Moreover, this equation does not allow for 'losses', i.e, for the dissipation of the magnetic energy. Since the oscillations of the magnetization are inevitably accompanied by a dissipation of their energy, to describe this behavior Gilbert, in 1955 corrected the Landau-Lifshitz by introducing a damping term[17, 18, 19].

$$\frac{d\vec{M}}{dt} = -\gamma(\vec{M} \times \vec{H}_{eff}) + \frac{\alpha}{M_S}(\vec{M} \times \frac{d\vec{M}}{dt}) \tag{1.3.4}$$

where γ denotes the gyromagnetic ratio and α is called dimensionless Gilbert damping. Thus, $(\alpha\omega)^{-1}$ is the relaxation time with ω the microwave frequency. The resulting precessional frequency is determined by the gyromagnetic ratio γ, the saturation magnetization M_s and the effective field $\vec{H}_{eff}$ which contains internal fields such as the magnetocrystalline anisotropy field, the demagnetizing field, the exchange field, the magnetoelastic field and the external bias field $\vec{H}_0$. In the LLG equation, the first term on the right hand side describes a precession of the magnetization vector, while the second term otherwise called Gilbert damping term has been phenomenologically introduced to take into account realignment of the magnetization to its equilibrium position. This phenomenon is illustrated in figure 1.3.1. For a ferromagnetic system, if we know its free magnetic energy density F, the effective magnetic field $\vec{H}_{eff}$ in the LLG equation 1.3.4 satisfies[20]:

$$\vec{H}_{eff} = -\frac{\partial F}{\partial \vec{M}} \tag{1.3.5}$$

1.3.2 Magnetic susceptibility

We will start solving the equation of motion in order to determine the high-frequency magnetic susceptibility limiting ourselves in the simple case a lossless ferromagnet. For this, we will focus on the LLG equation where the damping term is neglected.

1.3.2.1 Lossless Magnetic Susceptibility

To solve the Landau-Lifschitz equation, we linearize it by decomposing the magnetic field and the magnetization respectively in two components: a static component ($\vec{H}_0$, $\vec{M}_0$) and a dynamic component ($\vec{h}$,$\vec{m}$):

$$\vec{H} = \vec{H}_0 + \vec{h}_\sim \quad , \quad \vec{M} = \vec{M}_0 + \vec{m}_\sim \tag{1.3.6}$$

and by assuming that

$$\left\|\vec{h}_\sim\right\| \ll \left\|\vec{M}_0\right\|, \quad \|\vec{m}_\sim\| \ll \left\|\vec{M}_0\right\| \tag{1.3.7}$$

Then by substituting the sums 1.3.6 into the Landau-Lifschitz equation 1.3.3 taking into account the conditions 1.3.7, we can linearize the equation 1.3.3 in the following form:

$$\frac{\partial \vec{m}_\sim}{\partial t} + \gamma \vec{m}_\sim = -\gamma \vec{M}_0 \times \vec{h}_\sim \tag{1.3.8}$$

This equation is linear with the dynamic components $\vec{m}_\sim$ and $\vec{h}_\sim$. Considering harmonic time dependance of $\vec{m}_\sim$ and $\vec{h}_\sim$and using the complex amplitude methods [21, 22], leads to the following complex variables:

$$\vec{h}_\sim = \vec{h}\exp(i\omega t) \quad and \quad \vec{m}_\sim = \vec{m}\exp(i\omega t) \tag{1.3.9}$$

The complex vector quantities $\vec{m}$ and $\vec{h}$ in 1.3.9. They satisfy the Landau-Lifschitz equation:

$$i\omega\vec{m} + \gamma\vec{m} \times \overrightarrow{H}_0 = -\gamma\vec{M}_0 \times \vec{h} \tag{1.3.10}$$

We can rewrite this equation projecting onto the axes of cartesian coordinate system, taking the z-axis in the same direction than $\vec{H}_0$ and $\vec{H}_0$, we get:

$$i\omega m_x \quad + \quad \gamma H_0 m_y = \gamma M_0 h_y$$

$$-\gamma H_0 m_x \quad + \quad i\omega m_y = \gamma M_0 h_x$$

$$i\omega m_z = 0$$

The components $\vec{m}$ and $\vec{h}$ are related by the high-frequency magnetic susceptibility $\overleftrightarrow{\chi}$:

$$\vec{m} = \overleftrightarrow{\chi}\vec{h} \tag{1.3.11}$$

where $\overleftrightarrow{\chi}$ is called the Polder tensor:

$$\overleftrightarrow{\chi} = \begin{vmatrix} \chi & i\chi_a & 0 \\ -\chi_a & \chi & 0 \\ 0 & 0 & 0 \end{vmatrix} \tag{1.3.12}$$

where

$$\chi = \frac{\omega_H \omega_M / 4\pi}{\omega_H^2 - \omega^2},\ \chi_a = \frac{\omega \omega_M / 4\pi}{\omega_H^2 - \omega^2},\ \omega_H = \gamma H_0 \ and \quad \omega_M = \gamma 4\pi M_0 \tag{1.3.13}$$

The components $\vec{b}$ and $\vec{h}$ are are related by this relation:

$$\vec{h} = \overleftrightarrow{\mu}\vec{b} \tag{1.3.14}$$

The high-frequency magnetic susceptibility can be easily deduced from:

$$\overleftrightarrow{\mu} = \overleftrightarrow{I} + 4\pi\overleftrightarrow{\chi} \tag{1.3.15}$$

where $\overleftrightarrow{I}$ is the identity tensor viz. a diagonal tensor with all nonzero components equal to unity. We obtain the following relation by using equation 1.3.12:

$$\overleftrightarrow{\mu} = \begin{vmatrix} \mu & i\mu_a & 0 \\ -\mu_a & \mu & 0 \\ 0 & 0 & 1 \end{vmatrix} \tag{1.3.16}$$

where

$$\mu \quad = \quad \frac{\omega_\perp^2 - \omega^2}{\omega_H^2 - \omega^2},\ \mu_a = \chi_a = \frac{\omega \omega_M / 4\pi}{\omega_H^2 - \omega^2},\ \omega_\perp^2 = \omega_H(\omega_H + \omega_M) \tag{1.3.17}$$

1.3.2.2 Lossy magnetic susceptibility

In equation 1.3.12, if $\omega \to \omega_H$, we notice that the expressions χ and χ_a grow unlimitedly. Taking the magnetic damping into consideration will avoid this phenomenon. In this part, we will address the magnetic susceptibility for lossy ferromagnet. For this purpose, we will proceed in the same way by following the same reasoning than forgoing equations (i.e the lossless ferromagnet). For this, we will use the conditions used in equation 1.3.6 in the LLG equation, then we will have an equation similar than the one obtain in equation 1.3.10:

$$i\omega\vec{m} + \gamma\vec{m} \times \vec{H}_0 + \frac{i\alpha\omega}{M_0} \times \vec{M}_0 = -\gamma\vec{M}_0 \times \vec{m}(\vec{r}, t) \tag{1.3.18}$$

To find the magnetic susceptibility in the presence of losses, one has to project the linearized LLG equation onto the coordinate axes. Then, after resolving the resulting set of equations, we have the susceptibility tensor $\overleftrightarrow{\chi}$. However, it easier to derive directly the tensor $\overleftrightarrow{\chi}$, by replacing in equation 1.3.13 the following expression:

$$\omega \to \omega_H + i\omega \tag{1.3.19}$$

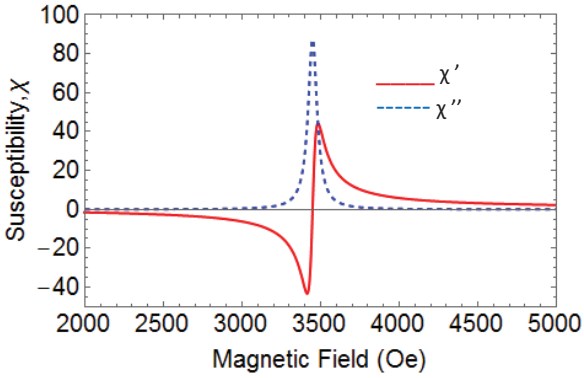

Figure 1.3.2 – The real (solid line) and the imaginary (dashed line) part of the complex hf susceptibility.

Thus replacing equation 1.3.19 in the expressions obtained in equation 1.3.13. Moreover, assuming $\chi = \chi^{'} + i\chi^{"}$ and $\chi_a = \chi_a^{'} + i\chi_a^{"}$, we get:

$$\chi^{'} = \frac{1}{D}\omega_M\omega_h[\omega_H^2 - (1-\alpha^2)\omega^2]$$

$$\chi^{"} = \frac{1}{D}\alpha\omega_M\omega[\omega_{\mathrm{H}}^2 + (1+\alpha^2)\omega^2]$$

$$\chi_a^{'} = \frac{1}{D}\alpha\omega_M\omega_H[\omega_{\mathrm{H}}^2 - (1-\alpha^2)\omega^2]$$

$$\chi_a^{"} = 2\alpha\omega_M\omega^2\omega_{\mathrm{H}}$$

$$D = [\omega_H^2 - (1+\alpha^2)\omega^2]^2 + 4\alpha^2\omega^2\omega_{\mathrm{H}}^2 \tag{1.3.20}$$

Figure 1.3.2 shows the dependence of the real and imaginary parts of the Polder tensor $\overleftrightarrow{\chi}$ on the applied bias field H_0. The real part change in sign, while the imaginary parts pass through maxima at the resonance. The resonance condition is given by :

$$\omega = \frac{\omega_H}{1+\alpha^2} \tag{1.3.21}$$

At the resonance, we have:

$$\chi^{"} = \frac{\omega_M}{2\alpha\omega} \tag{1.3.22}$$

The widths are defined as the intervals between ω or H_0values at points where $\chi" = \chi"_{res}/2$, are:

$$\Delta\omega = 2\alpha\omega\Delta H = \frac{2\alpha\omega}{\gamma} \tag{1.3.23}$$

The imaginary part of the magnetic susceptibility $\chi^{"}$ characterizes the energy absorption that appears in a ferromagnetic system due to excitation by a microwave field. The absorbed microwave power , P_{rf} in a ferromagnetic thin film, is defined as [20]:

$$P_{rf} = \frac{1}{2}\omega Im\left[\chi\right]\left|h_{rf}\right|^2 \tag{1.3.24}$$

1.4 Spin waves modes

In a ferromagnet it exists different magnetic excitations among which one can mention: the uniform precession mode and the spin waves. The uniform mode implies that all magnetic moments precess at the same frequency and phase. In the jargon of spin waves, it is the lowest energy magnon (spin wave) with the wavevector $k = 0$. However, higher order excitations may cause the magnetic moments to precess with the same frequency but at different phases and are referred to as spin waves. Since the exchange interaction is short range compared to dipolar interaction (cf. subsection 1.1.2), spin waves can be classified depending on their wavelength into dipole or exchange dominated. In the long wavelength regime, spin waves are dipole dominated and referred to as magnetostatic. In contrast, for small wave lengths the spin wave properties are dominated by exchange interaction. We will first present the uniform precession mode which is the mode mainly probed in ferromagnetic resonance experiments, then the magnetostatic spin waves and standing spin waves. To finish we will attack the relevant relaxation mechanisms generally encountered in ferromagnetic resonance.

1.4.1 Uniform precession mode

The uniform mode of the magnetization in a ferromagnet corresponds to the oscillations in phase of the magnetic moment under the influence of an external excitation, the microwave field (h_{rf}). In ferromagnetic resonance we have access to the uniform mode of magnetization which is the fundamental, the mode corresponding to the lowest energy of the ferromagnetic sample. So, in the calculation of the resonance condition, a uniform magnetization was assumed. The frequency of the uniform mode can be determined by solving the LLG equation as we did in (1.3.18). However, it is more convenient to solve the LLG in the spherical coordinate system since the ferromagnetic resonance technique is based on the angle between the magnetization and an applied magnetic field. This method was first proposed by Smit and Beljers [23] and by Suhl [24] and lately generalized by Skrotskii and Kurbatov taking the dissipation into account[25, 26].

This method is based on the transition of coordinates of the magnetization from a cartesian coordinate system $\vec{M} = \left(\ M_x,\ \ M_y,\ \ M_z\ \right)$ to a spherical coordinate system $\vec{M} = \left(\ M_S\sin(\theta)\cos(\varphi),\ \ M_S\sin(\theta)\sin(\varphi),\ \ M_S\cos(\theta)\ \right)$, where θ and φ are the angles of $\vec{M}$ in a spherical coordinate system and Mis the length of the magnetization vector $\vec{M}$ (see figure 1.4.1). We can rewrite the LLG equation introduced in equation 1.3.4 as a function of the variables θ and φ with the assumption of a uniform magnetization (macrospin approximation). The unit vectors in this spheric coordinate system are $\vec{e_r} =$

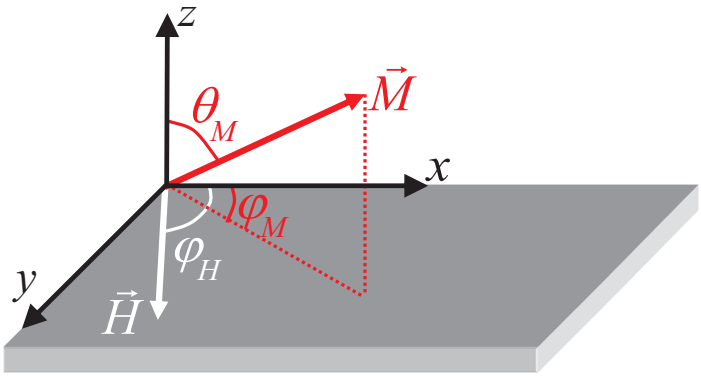

Figure 1.4.1 – Representation of the magnetization $\vec{M}$ and the magnetic field $\vec{H}$ in the space of spherical coordinate system.

$\begin{pmatrix} \sin(\theta)\cos(\varphi), & \sin(\theta)\sin(\varphi), & \cos(\theta) \end{pmatrix}, \vec{e}_\theta = \begin{pmatrix} \cos(\theta)\cos(\varphi), & \cos(\theta)\sin(\varphi), & -\sin(\theta) \end{pmatrix}$, $\vec{e}_\varphi = \begin{pmatrix} -\sin(\varphi), & \cos(\varphi), & 0 \end{pmatrix}$. The unit vectors $\vec{e}_r$, $\vec{e}_\theta$, $\vec{e}_\varphi$ are time-dependent, their derivatives as function of time are given:

$$\frac{d\vec{e}_r}{dt} = \dot{\theta}\vec{e}_\theta + \sin\theta\dot{\varphi}\vec{e}_\varphi$$

$$\frac{d\vec{e}_\theta}{dt} = -\dot{\theta}\vec{e}_r + \cos\theta\dot{\varphi}\vec{e}_\varphi$$

$$\frac{d\vec{e}_\varphi}{dt} = -\dot{\varphi}(\sin\theta\vec{e}_r - \cos\theta\vec{e}_\theta)$$

where $\dot{\theta}$and $\dot{\varphi}$are respectively the time derivative of θ and φ. In the spheric coordinate system, $\vec{M}$ and its time derivative $\frac{d\vec{M}}{dt}$ can be written as:

$$\vec{M} = M_S\vec{e}_r, \qquad \frac{d\vec{M}}{dt} = M_S\dot{\theta}\vec{e}_\theta + M_S\sin\theta\dot{\varphi}\vec{e}_\varphi \tag{1.4.1}$$

Furthermore, θ and φ depend on the position of the vector $\vec{M}$. Then, the effective field can be written as:

$$\vec{H}_{eff} = H_r\vec{e}_r + \theta_H\vec{e}_\theta + \varphi_H\vec{e}_\varphi \tag{1.4.2}$$

Remember the expression the effective field is given in equation 1.3.5; let us express the equation 1.3.5 in the spheric coordinate system:

$$\vec{H}_{eff} = -\left(\frac{\partial F}{\partial M}\vec{e}_r + \frac{1}{M_S}\frac{\partial F}{\partial\theta}\vec{e}_\theta + \frac{1}{M_S\sin\theta}\frac{\partial F}{\partial\varphi}\vec{e}_\varphi\right) \tag{1.4.3}$$

F being the total energy of the ferromagnetic system. Then, by identification of equations 1.4.2 and 1.4.3, we can determine θ_H and φ_H :

$$\theta_H = \frac{F_\theta}{M_S} \quad with: \quad F_\theta = \frac{\partial F}{\partial\theta} \tag{1.4.4}$$

$$\varphi_H = -\frac{F_\varphi}{M_S} \qquad with: \quad F_\varphi = \frac{\partial F}{\partial \theta} \tag{1.4.5}$$

Using the results from the foregoing equations 1.4.1 and 1.4.2 and incorporated them into the LLG equation, we have:

$$\begin{pmatrix} 0 \\ M_S\dot{\theta} \\ M_S \sin\theta\dot{\varphi} \end{pmatrix} = -\gamma \begin{pmatrix} 0 \\ -M_S\varphi_H \\ M_S\theta_H \end{pmatrix} + \frac{\alpha}{M_S} \begin{pmatrix} 0 \\ -M_S^2 \sin\theta\dot{\varphi}_H \\ M_S^2\dot{\theta} \end{pmatrix} \tag{1.4.6}$$

Then, replacing the equations 1.4.4 and 1.4.5 leads to the set of equations in the case of small dissipation, i.e $\alpha \ll 1$:

$$\frac{\partial \theta}{\partial t} = -\frac{\gamma}{M_S \sin\theta}\frac{\partial F}{\partial \varphi} - \frac{1}{M_S}\frac{\partial F}{\partial \theta} \tag{1.4.7}$$

$$\frac{\partial \varphi}{\partial t} = \frac{\gamma}{M_S \sin\theta}\frac{\partial F}{\partial \theta} - \frac{\alpha\gamma}{M_S \sin^2\theta}\frac{\partial F}{\partial \theta} \tag{1.4.8}$$

The equilibrium orientation of magnetization $\vec{M}$ which are defined by the angles θ_0 and φ_0 can be found from the equations, from whose solutions we must select those in which the free energy is a minimum.

$$\theta_H = \left(\frac{\partial F}{\partial \theta}\right)_{\theta=\theta_0,\varphi=\varphi_0} = 0 \qquad \varphi_H = \left(\frac{\partial F}{\partial \varphi}\right)_{\theta=\theta_0,\varphi=\varphi_0} = 0 \tag{1.4.9}$$

The analytical expressions of the resonance frequency can be obtained under certain conditions. Let us examine the non-equilibrium which arises when there are small deviations in the magnetization from the equilibrium position. In this case the conditions (equation1.4.9) no longer hold and the orientation of the vector $\vec{M}$ will be changed by the action of the components of the field which are not zero:

$$H_\theta = -\frac{F_\theta}{M_S}; \qquad H_\varphi = -\frac{F_\varphi}{M_S \sin\theta} \tag{1.4.10}$$

If the deviations from equilibrium

$$\delta\theta(t) = \theta(t) - \theta_0; \qquad \delta\varphi(t) = \varphi(t) - \varphi_0 \tag{1.4.11}$$

are small by comparison with the equilibrium values θ_0 and φ_0 then we can limit ourselves to the linear terms of the expansions of F_θ and F_φ:

$$F_\theta = F_{\theta\theta}\delta\theta + F_{\theta\varphi}\delta\varphi; \qquad F_\varphi = F_{\varphi\theta}\delta\theta + F_{\varphi\varphi}\delta\varphi \tag{1.4.12}$$

where the second derivatives of the free energy, with respect to the angles, $F_{\theta\theta}$ and $F_{\theta\varphi}$are calculated for the equilibrium position. Then we obtain a system of linear equations describing the small eigen-oscillations of the magnetization vector about the equilibrium position

$$-\frac{1}{\gamma}M_S \sin\theta_0 \delta\dot{\theta} = F_{\varphi\theta}\delta\theta + F_{\varphi\varphi}\delta\varphi \tag{1.4.13}$$

$$\frac{1}{\gamma}M_S \sin\theta_0 \delta\dot{\varphi} = F_{\theta\theta}\delta\theta + F_{\theta\varphi}\delta\varphi \tag{1.4.14}$$

The system of homogeneous equations has the periodic solutions $\delta\theta$, $\delta\varphi$ $\sim$exp$(i\omega t)$ with a frequency ω if the determinant of the characteristic system of equations is equal to zero:

$$F_{\theta\varphi}^2 - F_{\theta\theta}F_{\varphi\varphi} + \omega^2\gamma^{-2}M_S^2 \sin^2\theta_0 = 0$$

from which we find for the characteristic, or resonance, frequency of the oscillations

$$\omega_{res} = \gamma H_{eff} = \frac{\gamma}{M_S \sin\theta_0}\left[\frac{\partial^2 F}{\partial\theta^2}\frac{\partial^2 F}{\partial\varphi^2} + \left(\frac{\partial^2 F}{\partial\theta\partial\varphi}\right)^2\right]^{\frac{1}{2}} \tag{1.4.15}$$

known as the Smith-Belers-Suhl formula.

1.4.2 Magnetostatic spin waves

In subsection 1.3.2, we have stipulated the magnetic field as given at certain point of the ferromagnet, that has enabled us to calculated the ac magnetization at the same. However, this field can not be seen as given but depends strongly on the magnetization distribution in the entire system. In this condition the field and magnetization distribution over the sample can be found solving the Maxwell equation in the magnetostatic approximation combined with the material equations taking into account the boundaries conditions. The fundamental equations of macroscopic electrodynamics, the Maxwell equations are:

$$\vec{\nabla}\times\vec{E} + \tfrac{1}{c}\tfrac{\partial\vec{B}}{\partial t} = 0 \qquad \nabla\vec{B} = 0 \tag{1.4.16}$$

$$\vec{\nabla}\times\vec{H} - \tfrac{1}{c}\tfrac{\partial\vec{D}}{\partial t} = \tfrac{4\pi}{c}\vec{J} \qquad \nabla\vec{D} = 4\pi R \tag{1.4.17}$$

Here $\vec{E}$ and $\vec{D}$ are the macroscopic electric-field and electric-displacement vectors, $\vec{H}$ and $\vec{B}$ are the magnetic-field and magnetic-induction vectors, and $\vec{J}$ and $\vec{R}$, are the free electric-current and electric-charge densities. The quantities $\vec{E}$ and $\vec{B}$ are the space and time averages of the microscopic fields, respectively electric and magnetic. The vectors $\vec{D}$ and $\vec{H}$ in equations 1.4.16 and 1.4.17 are defined as:

$$\vec{D} = \vec{E} + 4\pi\vec{P} \qquad \vec{D} = \vec{H} - 4\pi\vec{M} \tag{1.4.18}$$

where $\vec{P}$ is the polarization, i.e the electric-dipole-moment density, and $\vec{M}$ is the magnetization. The equation charge conservation follows from equations 1.4.16 and 1.4.17:

$$\nabla\vec{J} + \frac{\partial R}{\partial t} = 0$$

The magnetic field in our case is a sum of the steady and ac fields. Suppose all the quantities in equations 1.4.16 and 1.4.17 including electric field to be such sums.Assume

that the ac components $\vec{h}_{\sim}$, $\vec{e}_{\sim}$, $\vec{b}_{\sim}$, $\vec{d}_{\sim}$, $\rho_{\sim}$ and $\vec{j}_{\sim}$ are small compared with the steady components, respectively, $\vec{H}_0$, $\vec{E}_0$, $\vec{B}_0$, $\vec{D}_0$, R_0 and $\vec{J}_0$. Then, if we consider the different fields and currents varying harmonically with time, all the quantities have such time dependance and we can use the method of complex amplitudes (Subsection 1.3.2). Substituting the sums of steady and ac components of all quantities in equations 1.4.16 and 1.4.17, we obtain two independent system of equations: for steady components and, according to the methods of the complex amplitudes, for the complex amplitudes of the ac components. The system for the complex amplitudes of the ac quantities is given by equations and 1.4.20[26]:

$$\vec{\nabla} \times \vec{e} + ik_0\vec{b} = 0 \qquad \nabla\vec{b} = 0 \tag{1.4.19}$$

$$\vec{\nabla} \times \vec{h} - ik_0\vec{d} = \tfrac{4\pi}{c}\vec{j} \qquad \nabla\vec{d} = 4\pi\rho \tag{1.4.20}$$

Where $k_0 = \omega/c$. The materials equations have to be introduced in the Maxwell equations $\vec{d} = \overleftrightarrow{\epsilon}\vec{e}$ and $\vec{b} = \overleftrightarrow{\mu}\vec{h}$ where $\overleftrightarrow{\epsilon}$ is the dielectric permittivity tensor and $\overleftrightarrow{\mu}$ the magnetic permeability tensor. We can show for slow waves $k \gg k_0 = \frac{\omega}{c}$, then, in zero approximation with respect to (k_0/k), the terms $ik_0\vec{d}$ in the Maxwell's equations can be neglected. We have then the magnetostatic approximation $\vec{\nabla} \times \vec{h} = 0$. In this situation, $\vec{j} = \vec{0}$ and $\rho = 0$, therefore equations 1.4.19 and 1.4.20 simplify to:

$$\begin{cases} \vec{\nabla} \times \vec{h} = 0 \\ \nabla(\overleftrightarrow{\mu}\vec{h}) = 0 \\ \vec{\nabla} \times \vec{e} = 0 \\ \nabla\vec{e} = 0 \end{cases} \tag{1.4.21}$$

The solutions of the equations with the boundaries conditions give us $\vec{h}$, $\vec{m} = \overleftrightarrow{\chi}\vec{h}$ and the dispersions relations $\omega(k)$. If $rot\vec{h} = 0$ it exists by analogy to the scalar potential resulting from Maxwell equation when $div(\overrightarrow{e}) = 0$, a vector potential ψ (the magnetostatic scalar potential) such as:

$$\vec{h} = -\nabla\psi \tag{1.4.22}$$

Substituting the relation (1.4.22) in (1.4.19 and 1.4.20), we have :

$$\nabla(\overleftrightarrow{\mu}\nabla\psi) = 0 \tag{1.4.23}$$

Assuming the magnetic permeability tensor $\overleftrightarrow{\mu} = \overleftrightarrow{I} + \overleftrightarrow{\chi}$ to be independent to the position, we have the equation know as Walker[27] and describes the magnetostatic modes.$(1+\chi)\left[\frac{\partial^2\psi}{\partial x^2} + \frac{\partial^2\psi}{\partial y^2}\right] + \frac{\partial^2\psi}{\partial z^2} = 0$

We can notice that, for $\chi = -1$ the solution corresponds to the uniform mode and for $\chi \neq -1$ the solutions are the propagating spin waves[28]. The magnetostatic waves propagating in a ferromagnetic layers are subdivided into magnetostatic surface waves (MSSW), magnetostatic forward volume waves (MSFVW) who have been first discovered by Damon and Eshbach[29, 30] and backward volume waves (MSBVW) who were first observed by Bar'yakhtar and Kagan [31].

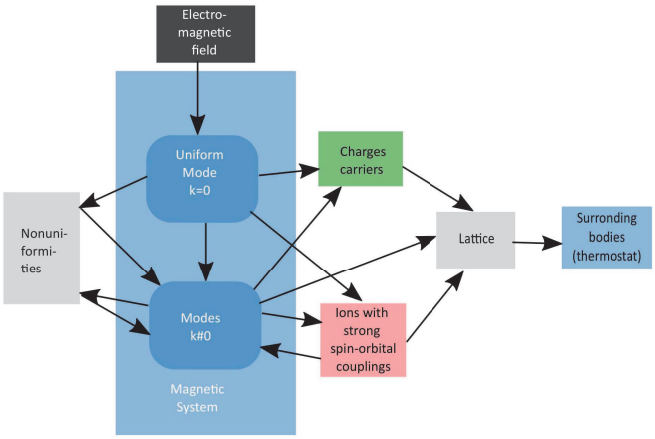

Figure 1.4.2 – Depiction of the possible paths of the relaxation of the magnetization precession. Adapted from [22].

1.4.3 Standing spin waves

So far, besides the uniform mode, confined geometries often support excitation of higher-order FMR modes which represent standing spin waves across the direction of confinement : the standing spin waves modes. Such standing spin waves modes were first predicted theoretically by Kittel[32] and corroborated experimentally by Seavey and Tannenwald[33]. They correspond to magnetization oscillations, uniform over the film surface and nonuniform in the direction normal to the surface. As the name implies, the dynamic magnetization profiles of PSSW across the thickness of the film represent stationary waves with wavevector $k = n\pi/d$ where n is the mode number and d is the thickness of the film.

1.4.4 Relaxation mechanisms

So far, the magnetic relaxation mechanism have been phenomenologically described by the LLG equation (1.3.4). In ferromagnetic resonance experiments the rf magnetic field is substantially homogeneous over the volume of the sample. Thus it excites only the homogeneous (or uniform) mode of the spin-wave spectrum. An inhomogeneous additional magnetic field broadens the resonance line because it leads to scattering of energy into nonuniform modes. In a very simple scheme the relaxation mechanism of the excited magnetization can be described in the Fig 1.4.2. The scheme indicates that uniform magnons with $k = 0$, that is the uniformly precessing magnetization are excited by microwave electromagnetic field. The uniform magnons can relax either via spin-orbit coupling and phonon-magnon interaction directly to the lattice or by dissipationless magnon-magnon scattering into non-zero wave vector magnon states followed by relaxation to the lattice. The relaxation mechanisms are classified into types: intrinsic relaxation mechanism or Gilbert and extrinsic mechanisms.

1.4.4.1 Intrinsic mechanisms

Eddy current When studying metal specimens with high electrical conductivity, the microwaves field penetrates in practice only a thin surface layer of the sample which leads to a volume inhomogeneity in the magnetization. Apart from the losses connected with ferromagnetic resonance there are also eddy current losses under these conditions which are proportional to the electrical conductivity of the material and the square of the frequency of the microwave field $\vec{h_{rf}}$. The eddy current can be neglected in ferromagnetism thin film since the thickness is very small compared to eddy current ($d \ll \delta$). In microwave frequencies, the depth of the field penetration in metal is about 10^{-5} — 10^{-4} cm.

$$\delta = \sqrt{\frac{2}{\sigma\mu\omega}} \tag{1.4.24}$$

1.4.4.2 Extrinsic mechanism

Damping Mechanism In various magnetic systems, the damping can be described by the phenomenological Gilbert damping parameter G. Sometimes, the dimensionless parameter α is given instead, which is related to G according to $\alpha = G/\gamma M$. If the Gilbert damping is referred as intrinsic damping, then it follows from the free energy density approach of the ferromagnetic system that the FMR linewidth is given by Eq.1.4.25 [26]:

$$\Delta\omega = \left(\frac{d\omega}{dH}\right)\Delta H = \frac{\alpha\gamma}{M}\left[\frac{\partial^2 F}{\partial\theta^2}\frac{\partial^2 F}{\partial\varphi^2} + \frac{1}{\sin\theta_0}\frac{\partial^2 F}{\partial\theta\partial\varphi}\right]^{\frac{1}{2}} \tag{1.4.25}$$

In ferromagnetic resonance, in order to determine α, frequency dependent FMR measurements over a large range of microwave frequencies are needed. It is important to point out in the case where the magnetization and the applied field are parallel, the FMR linewidth varies linearly with frequency (See Eq. 1.3.23).

Two-magnons scattering mechanism In ferromagnetic resonance, in addition to the Gilbert mechanism there exists another relaxation process which contributes to the damping mechanism: two magnon scattering. The two magnon scattering process involves coupling between the uniform mode and spin waves over a range of wave vectors which are degenerate with the microwave field and the FMR response. The coupling is typically strongest for spin wave wavelengths which are on the order of whatever inhomogeneities may be present in the material. This process is termed "two magnon scattering" because the mechanism can be expressed theoretically by a second quantization formalism in which a uniform precession or FMR magnon is destroyed and a spin wave magnon at the same frequency is created. The two magnon scattering contribution to the FMR linewidth has been investigated theoretically by Arias and Mills and experimentally for three types of inhomogeneities in bulk YIG, namely, surface pits, volume pores or voids, and randomly distributed single crystal grains in a polycrystal[34, 35]. Arias and Mills have calculated the contribution of two magnons scattering on the FMR linewidth based on the Green's functions formalism[36].

$$\Delta\omega_{pp}^{2mag} = \Gamma \arcsin\left(\sqrt{\frac{\sqrt{\omega^2 + (\omega_0/2)^2} - \omega_0/2}{\sqrt{\omega^2 + (\omega_0/2)^2} + \omega_0/2}}\right) \tag{1.4.26}$$

where $\omega = \gamma M_{eff}$ and $M_{eff} = 4\pi M_S - H_\perp$ being the effective magnetization. Γ represents the strength of the two-magnon scattering mechanism.

Mosaicity The mosaicity is another contribution of line broadening of the FMR linewidth which caused by a spread of the sample parameters on a very large scale. The mosacity contribution can be found in the internal field, thickness, or orientation of the crystallites within the samples. The individual regions have slightly different resonance fields. The overall signal will be a superposition of these local FMR lines yielding a broader linewidth. The mosaicity contribution is given by [37, 38, 39, 36]:

$$\Delta H^{mos}(\omega, \varphi_H) = \left| \frac{\partial H_{res}}{\partial \varphi_H} \Delta\varphi_H \right| = \left| \frac{\partial H}{\partial \varphi_H} \Delta\varphi_H \right|_{res} \tag{1.4.27}$$

Where $\Delta\varphi_H$ is the average spread of the easy axis anisotropy direction in the film plane. It is worth to mention that for frequency dependent measurements along the easy and hard axes the partial derivatives are zero and thus the mosaicity contribution vanishes.

Bibliography

[1] M. Getzlaff, Fundamental of magnetism, Springer (2008). (Cited on page 17.)

[2] K. H. J. Buschow, F. R. D. B. Physics of magnetism and Magnetic Materials, Kluwer academic publishers (Cited on pages 14 and 17.)

[3] A. P. Guimaraes, Magnetism and magnetic resonance in solids, John Wiley & Sons (1998). (Cited on pages 14 and 17.)

[4] Y. Liu, D. J. Sellmyer, D. Shindo, Handbook of advanced magnetic materials, volume 1: advanced magnetic materials: nanostructural effects, Springer (2006). (Cited on page 14.)

[5] M. A. Ruderman and C. Kittel, Physical Review **96,** 99 (1954). (Cited on page 16.)

[6] T. Kasuya, Progress of Theoretical Physics **16**, 45 (1956). (Cited on page 16.)

[7] K. Yosida, Physical Review **106**, 893 (1957). (Cited on page 16.)

[8] M. Farle, T. Silva, and G. Woltersdorf, Magnetic Nanostructures, Springer Tracts in Modern Physics **246** (2013). (Cited on page 17.)

[9] R. C. O'Handley, Modern Magnetic Materials: Principles and Applications Wiley (2000). (Cited on page 17.)

[10] O. Commowick and G. Malandain, proceedings of the 10th International conference on medical image computing and computer-assisted intervention - MICCAI 2007, Part II, Springer Verlag, **4792**, 203 (2007). (Cited on page 17.)

[11] S. Chikazumi, Physics of Ferromagnetism, Oxford University Press, New York (1997). (Cited on pages 17 and 20.)

[12] M. B. Stearns, Magnetic Properties of 3d, 4d and 5d Elements, Alloys and Compounds (Landolt–Bornstein Numerical Data and Functional Relationships in Science and Technology Group III vol 19a (Berlin: Springer). (1986) (Cited on page 20.)

[13] A. E. Clark 1980 Magnetostrictive Rare Earth-Fe2 Compounds (Ferromagnetic Materials 1) (Amsterdam: North-Holland). (Cited on page 20.)

[14] D. Sander, Report on Progress Physics **62,** 809 (1999). (Cited on page 20.)

[15] H. B. Callen and N. Goldberg, Journal of Applied Physics **36**, 976 (1965). (Cited on page 23.)

[16] E. Du Tremollet De Lacheisserie, Magnetostriction. Theory and Application of Magnetoelasticity (Boca Raton, FL: CRC Press) (1993) (Cited on page 23.)

[17] M. Farle, Report on Progress Physics **61**, 755 (1998). (Cited on pages 23 and 24.)

[18] L. Landau and E. Lifshitz. On the theory of the dispersion of magnetic permeability in ferromagnetic bodies. Phys. Z. Sowjetunion (1935). (Cited on pages 23 and 24.)

[19] T. L. Gilbert, Physical Review **100**, 1243 (1955). (Cited on page 24.)

[20] Z. Celinski et al, Journal of Magnetism and Magnetic Materials **166**, 6 (1997). (Cited on pages 24 and 28.)

[21] A. Gurevich, Guides et rnateurs creux, Moscou, "Sovetskoe radio" (1952). (Cited on page 25.)

[22] A. G. Gurevich, G. A. Melkov, Magnetization oscillations and waves, CRC Press, New York. (Cited on pages v, 17, 25 and 33.)

[23] J. Smit and H.G. Beljers. Philip. Research Reports **10**, 113 (1955). (Cited on page 28.)

[24] H. Suhl, Physical Review **97**, 555 (1955) (Cited on page 28.)

[25] J. Pelzl and U. Netzelmann , Locally resolved magnetic resonance in ferromagnetic layers and films Topics in Current Physics vol 47 (Berlin: Springer) (1989) (Cited on page 28.)

[26] S. V. Vonsovski, Ferromagnetic Resonance, Pergamon Press, Oxford London Edinburgh New York Toronto Paris Frankfurt (1966). (Cited on pages 28, 32 and 34.)

[27] L. R. Walker. Physical Review **105**, 390 (1957). (Cited on page 32.)

[28] I. Neudecker, Magnetization Dynamics of Confined Ferromagnetic Systems, Dissertation, Universität Regensburg, Germany (2006). (Cited on page 32.)

[29] P. E. Zil'berman, V. M. Kulikov, V. V. Tikhonov, I. V. Shein, Zh. Eksp. Teor. Fiz. **99**, 1566 (1991) (Cited on page 32.)

[30] R. W. Damon and J. R. Eshbach, Journal of Physics and Chemistry of Solids **19**, 308 (1961). (Cited on page 32.)

[31] V. G. Bar'yakhtar and M. I. Kaganov, Nonuniform Resonances and Spin Waves, Fizmatgiz, Moscow (1961). (Cited on page 32.)

[32] C. Kittel, Physical Review **110**, 1295 (1958). (Cited on page 33.)

[33] M. H. Seavey and P. E. Tannenwald, Physical Review Letters **1**, 168 (1958). (Cited on page 33.)

[34] E. Schlomann, A.I.E.E. Special Pub. **T-91**, 600 (1956). (Cited on page 34.)

[35] M. Sparks, R. Loudon and C. Kittel, Physical Review **122**, 791 (1961). (Cited on page 34.)

[36] R. Arias and D. Mills, Physical Review B, **60**, 7395 (1999). (Cited on pages 34 and 35.)

[37] R. D. McMichael, D. J. Twisselmann, and A. Kunz, Physical Review Letters **90**, 227601 (2003). (Cited on page 35.)

[38] M. Belmeguenai et al., Physical Review B **87** 184431 (2013). (Cited on page 35.)

[39] Kh. Zakeri,J. Lindner, I. Barsukov, R. Meckenstock, M. Farle, U. von Hrsten, H. Wende, W. Keune, Physical Review B **76**, 104416 (2007)

(Cited on page 35.)

2 Mechanical testing

In this chapter, we address the theoretical background regarding the elastic properties of solids. We start with a review of some fundamental aspects of stress, strain and the related elastic energy density. We then introduce the mechanical testing we have used in this research project, the ferromagnetic thin film/bending system and ferromagnetic thin film/piezoelectric actuator hybrid systems as devices concepts to realize the magnetomechanical coupling in ferromagnetic thin films and nanostructures. Fisrt of all, we will present the bending testing and the theoretical backgound behind it, before to attack the piezoelectric constituent, its physical properties, crystal structure and some resulting on the behaviour of the piezoelectric actuation under different voltage loading conditions.

2.1 Basics in elasticity

In this chapter, we will first introduce stress and strain notions before discussing elasticity in the basic case of a cubic single crystal.

2.1.1 Stress and Strains in solids

In order to facilitate the understanding of the magnetoelastic processes in magnetostrictive materials we deemed it necessary to start out with some fundamental definition of stress and strain. A volume element of a magnetostrictive material is shown in Fig. 2.1.1. It is assumed to be subjected to stress. Two kinds of forces can act on the element. First, there are body forces which act throughout the body with a magnitude proportional to the volume of the element. Such a body force can, for example, be due to gravity or electromagnetic interaction. Second, there are forces acting on the surfaces of the element due to interaction with surrounding material. In this case, the applied stresses on the magnetostricitive material σ are defined as the force F per area A perpendicular to the direction of the applied force. Depending on the force direction, one can distinguish between tensile and compressive stress. The stress has the same dimension as pressure, that is, $N.m^{-2}$ (or Pa) in SI unit system and $dyn.cm^{-2}$ in CGS unit system. The solid responds to the stress by a deformation called strain ε. The stress tensor is a second rank tensor, its components will all be noted by the symbol σ for the normal stresses or τ for the shear stresses with appropriate suffices. The first suffix denotes the direction of the outward normal to the surface upon which it acts and the second the direction of the stress components (see Figure 2.1.1).

One consequence of the foregoing notation is that normal (*i.e.* tensile and compressive) stresses have both the same suffices (*i.e.* σ_{xx}, σ_{yy} and σ_{zz} in Figure 2.1.1) and are positive when tensile. The remaining six stress components in Figure 2.1.1 (i.e τ_{xy}, τ_{yz}, τ_{zz}, τ_{zy}, τ_{zx}, τ_{xz}) have two different suffices and correspond to shear stresses.

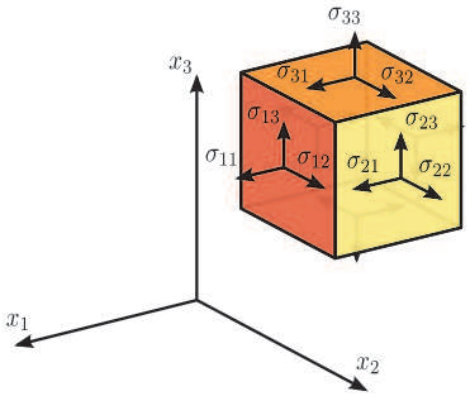

Figure 2.1.1 – The forces on the faces of a. unit cube in a homogeneously stressed body.

The nine components in the second rank tensor:

$$\begin{bmatrix} \sigma_{xx} & \sigma_{xy} & \sigma_{yz} \\ \sigma_{yx} & \sigma_{yy} & \sigma_{yz} \\ \sigma_{zx} & \sigma_{zy} & \sigma_{zz} \end{bmatrix} = \begin{bmatrix} \sigma_{xx} & \tau_{xy} & \tau_{yz} \\ \tau_{yx} & \sigma_{yy} & \tau_{yz} \\ \tau_{zx} & \tau_{zy} & \sigma_{zz} \end{bmatrix} \tag{2.1.1}$$

are not all independent since the cubic volume element must be in equilibrium, neither accelerating linearly nor rotating. This condition is achieved when $\sigma_{ij} = \sigma_{ji}$, *i.e.* , when the tensor is symmetrical and has six independent components.

The strain is a consequence of stress. As a result of strain in a material a point is moved from (x_1, x_2, x_3) to (x_1', x_2', x_3') by amounts u_i such that $x_i' = x_i + u_i$, where u_i vary with position:

$$u_i = e_{ij} x_j \tag{2.1.2}$$

We have defined a second rank tensor with nine components e_{ij} (with $e_{ij} = \frac{\partial u_i}{\partial x_j}$). The component e_{ij} represents the movement of points on the x_j axis in the direction of the x_i axis. We can separate these contributions by expressing e_{ij} as the sum of symmetrical (ε_{ij}) and antisymmetrical (ω_{ij}) components:

$$e_{ij} = \varepsilon_{ij} + \omega_{ij} \tag{2.1.3}$$

where

$$\varepsilon_{ij} = (e_{ij} + e_{ji})/2 \tag{2.1.4}$$

and

$$\omega_{ij} = (e_{ij} - e_{ji})/2 \tag{2.1.5}$$

Shape change (shear) is described by the symmetrical tensor ε_{ij}. This is the strain tensor. Rotation is described by the antisymmetrical tensor ω_{ij}.

Stresses		Strains	
Tensor Notation	Contracted Notation	Tensor Notation	Contracted Notation
$\sigma_{11}(\sigma_1)$	σ_1	$\varepsilon_{11}(\varepsilon_1)$	ε_1
$\sigma_{22}(\sigma_2)$	σ_2	$\varepsilon_{22}(\varepsilon_2)$	ε_2
$\sigma_{33}(\sigma_3)$	σ_3	$\varepsilon_{33}(\varepsilon_3)$	ε_3
$\tau_{23}=\sigma_{32}$	σ_4	$\gamma_{23}=2\varepsilon_{32}$	ε_4
$\tau_{31}=\sigma_{31}$	σ_5	$\gamma_{31}=2\varepsilon_{31}$	ε_5
$\tau_{12}=\sigma_{12}$	σ_6	$\gamma_{12}=2\varepsilon_{12}$	ε_6

Table 2.1 – Tensor versus contracted notation for stresses and strains.

2.1.2 Elasticity in single crystal: the cubic case

Hooke's law says that little stress will produce little strain. Put otherwise, strain is proportional to stress [1]. Stress and strain can be related by either the stiffness tensor (C_{ijkl}) or the compliance tensor (s_{ijkl}), each of which is of fourth rank. For example a stress component is given in terms of the strain components which is given using the summation convention by:

$$\sigma_{ij} = C_{ijkl}\varepsilon_{kl} \tag{2.1.6}$$

Or, using the compliance tensor:

$$\varepsilon_{ij} = S_{ijkl}\sigma_{kl} \tag{2.1.7}$$

If the body is homogeneous, that is, the mechanical properties are the same for every particle in the body, then c_{ijkl} are independent of position. We shall be concerned only with homogeneous bodies. There are 81 coefficients in equation 2.1.6 and equation 2.1.7, due to the symmetry of the strain tensor ($\varepsilon_{ij} = \varepsilon_{ji}$), we have $C_{ijkl} = C_{ijlk}$, the number of independent C_{ijkl} from 81 to 54. Moreover, due the symmetry of the stress tensor ($\sigma_{ij} = \sigma_{ji}$), we have $C_{ijkl} = C_{jikl}$, The preceding equations further reduce the number of independent coefficients 54 independent by 18. Thus, we have, for the general case of a linearly elastic body, a maximum of 36 material coefficients. Using this so-called contracted Voigt subscript notation (See 2.1), we can express the various equations in a shorter form[2], the fourth order tensor C_{ijkl} reduces to the matrix representation C_{ij}.

The stiffness and complaince matrix C_{ij} (resp. S_{ij}) have 36 constants. However, less than 36 of the constants can be shown to actually be independent for elastic materials when important characteristics of the strain energy are considered. Elastic materials for which an elastic potential or strain energy density function exists have incremental work per unit volume of [3] :

$$\mathrm{d}F_{el} = \sigma_i \mathrm{d}\varepsilon_i \tag{2.1.8}$$

When the stresses σ_i act through strains $\mathrm{d}\epsilon_i$. However, because of the stress-strain relations, Equation 2.1.6, the increment work becomes:

$$\mathrm{d}F_{el} = C_{ij}\varepsilon_j \mathrm{d}\varepsilon_i \tag{2.1.9}$$

Upon integration for all strains, the work per unit of volume is :

$$F_{el} = \frac{1}{2} C_{ij} \varepsilon_i \varepsilon_j \tag{2.1.10}$$

However, Hooke's law, Equation 2.1.6, can be derived from Equation 2.1.10 i.e $\frac{\partial F_{el}}{\partial \epsilon_i} = C_{ij}$, whereupon $\frac{\partial^2 F_{el}}{\partial \epsilon_i \partial \epsilon_j} = \frac{\partial^2 F_{el}}{\partial \epsilon_j \partial \epsilon_i} = C_{ij} = C_{ji}$. Thus, the stiffness matrix is symmetric, so only 21 of the constants are independent. We have then the following stress-strain relation in Equation 2.1.11 [1] with a reduction from 36 to 21 independant constants:

$$\begin{bmatrix} \sigma_1 \\ \sigma_2 \\ \sigma_3 \\ \tau_4 \\ \tau_5 \\ \tau_6 \end{bmatrix} = \begin{bmatrix} C_{11} & C_{12} & C_{13} & C_{14} & C_{15} & C_{16} \\ C_{12} & C_{22} & C_{23} & C_{24} & C_{25} & C_{26} \\ C_{13} & C_{23} & C_{33} & C_{34} & C_{35} & C_{36} \\ C_{14} & C_{24} & C_{34} & C_{44} & C_{45} & C_{46} \\ C_{15} & C_{25} & C_{35} & C_{45} & C_{55} & C_{56} \\ C_{16} & C_{26} & C_{36} & C_{46} & C_{56} & C_{66} \end{bmatrix} \begin{bmatrix} \varepsilon_1 \\ \varepsilon_2 \\ \varepsilon_3 \\ \gamma_4 \\ \gamma_5 \\ \gamma_6 \end{bmatrix} \tag{2.1.11}$$

The number of independant elastic constants can be further reduced in materials having a higher degree of crystal symmetry. In such case, some elastic constants may vanishes while the others are relared each other. Among the material with higher degree of symmetry, the cubic material is the simplest. Consider a cubic material for which the [100], [010] and [001] cube axes are parallel to the axes x_1; x_2; x_3 coordinate system. Then, The non-zero elements of the elastic stiffnesss C_{ij} are given in the Equation 2.1.12 where $C_{11} = C_{22} = C_{33}$, $C_{12} = C_{23} = C_{31}$, $C_{44} = C_{55} = C_{66}$ and all others elastic constants vanish [2].

$$\begin{bmatrix} C_{11} & C_{12} & C_{12} & 0 & 0 & 0 \\ C_{12} & C_{11} & C_{12} & 0 & 0 & 0 \\ C_{12} & C_{12} & C_{11} & 0 & 0 & 0 \\ 0 & 0 & 0 & C_{44} & 0 & 0 \\ 0 & 0 & 0 & 0 & C_{44} & 0 \\ 0 & 0 & 0 & 0 & 0 & C_{44} \end{bmatrix} \tag{2.1.12}$$

Thus, using Equation 2.1.12 into the Equation 2.1.10 we can calculate the elastic energy for a cubic material [3, 4]:

$$F_{el} = \frac{1}{2} C_{11} (\varepsilon_1^2 + \varepsilon_2^2 + \varepsilon_3^2) + C_{12} (\varepsilon_1 \varepsilon_2 + \varepsilon_2 \varepsilon_3 + \varepsilon_1 \varepsilon_3) + \frac{1}{2} C_{44} (\varepsilon_4^2 + \varepsilon_5^2 + \varepsilon_6^2) \tag{2.1.13}$$

2.2 Elasticity in polycrystals

The thin films studied during this research project are either polycrystals films or amoprhous films. Indeed, the polycrystalline thin films are constituted of an aggregate of crystal grains of various sizes and orientation. Their macroscopic properties are affected by the properties of the individual grains. The macroscopic behavior of our polycrystalline films will be regarded as isotropic and homogeneous in term of elastic properties because we have verified that they have random crystallographic texture (non-textured polycrystal). The elastic strain and stress states of an individual crystallites

1. The relations in Equation 2.1.11 are referred to characterizing anistropic materials beccause there no planes of symmetry for the materials properties.

is determined by the Hooke's equation (see equation 2.1.6) together with the boundary conditions. In these conditions, homogeneization methods are used to define effective elastic coefficients which will depend on the single crystal's elastic coefficients. Reuss and Voigt homogeneization methods are the simplest ones, as discussed in the precedent chapter. They are well known because the obtained values define a boundary for the effective elastic coefficients. For instance, in the case of an isotropic thin film, the effective elastic coefficients in the Voigt model ($\widetilde{C}_{11}$, $\widetilde{C}_{12}$ and $\widetilde{C}_{44}$) are given by (with $C = C_{11} - C_{12} - 2C_{44}$):

$$\widetilde{C}_{11} = C_{11} - \frac{2}{5}C \tag{2.2.1}$$

$$\widetilde{C}_{12} = C_{12} + \frac{1}{5}C \tag{2.2.2}$$

$$\widetilde{C}_{44} = C_{44} + \frac{1}{5}C \tag{2.2.3}$$

while in the Reuss model they are given by (with $S = S_{11} - S_{12} - \frac{1}{2}S_{44}$):

$$\widetilde{C}_{11}^{-1} = C_{11}^{-1} - \frac{2}{5}S \tag{2.2.4}$$

$$\widetilde{C}_{12}^{-1} = C_{12}^{-1} + \frac{1}{5}S \tag{2.2.5}$$

$$\widetilde{C}_{44}^{-1} = C_{44}^{-1} + \frac{4}{5}S \tag{2.2.6}$$

$$\begin{bmatrix} \widetilde{C}_{11}+2\widetilde{C}_{44} & \widetilde{C}_{11} & \widetilde{C}_{11} & 0 & 0 & 0 \\ \widetilde{C}_{11} & \widetilde{C}_{11}+2\widetilde{C}_{44} & \widetilde{C}_{11} & 0 & 0 & 0 \\ \widetilde{C}_{11} & \widetilde{C}_{11} & \widetilde{C}_{11}+2\widetilde{C}_{44} & 0 & 0 & 0 \\ 0 & 0 & 0 & \widetilde{C}_{44} & 0 & 0 \\ 0 & 0 & 0 & 0 & \widetilde{C}_{44} & 0 \\ 0 & 0 & 0 & 0 & 0 & \widetilde{C}_{44} \end{bmatrix} \tag{2.2.7}$$

One can note here that only two independent coefficients are remaining ($\widetilde{C}_{11}$ and $\widetilde{C}_{44}$). The following relation is thus deduced:

$$\sigma_{ij} = \widetilde{C}_{11}\delta_{ij}\varepsilon_{kk} + 2\widetilde{C}_{44}\varepsilon_{ij} \tag{2.2.8}$$

From this relation $\sigma_{kk} = \left(3\widetilde{C}_{11} + 2\widetilde{C}_{44}\right)\varepsilon_{kk}$, we can rewrite the above formula as function of the stresses:

$$\varepsilon_{ij} = \frac{1}{2\widetilde{C}_{44}}\sigma_{ij} - \frac{\widetilde{C}_{11}}{2\widetilde{C}_{44}(3\widetilde{C}_{11} + 2\widetilde{C}_{44})}\sigma_{kk}\delta_{ij} \tag{2.2.9}$$

We can define the Young's modulus (Y) and the Poisson's ratio (ν) by considering a simple traction:

$$\sigma = \begin{pmatrix} \sigma & 0 & 0 \\ 0 & 0 & 0 \\ 0 & 0 & 0 \end{pmatrix}; \varepsilon = \begin{pmatrix} \varepsilon_L & 0 & 0 \\ 0 & \varepsilon_T & 0 \\ 0 & 0 & \varepsilon_T \end{pmatrix} \tag{2.2.10}$$

Where ε_L and ε_T stand for the longitudinal and the transverse strains, respectively. They can be written as function of $\widetilde{C}_{11}$ and $\widetilde{C}_{44}$:

$$\varepsilon_L = \frac{\widetilde{C}_{11} + \widetilde{C}_{44}}{\widetilde{C}_{44}(3\widetilde{C}_{11} + 2\widetilde{C}_{44})}\sigma = \frac{1}{Y}\sigma \tag{2.2.11}$$

$$\varepsilon_T = -\frac{\widetilde{C}_{11}}{2\widetilde{C}_{44}(3\widetilde{C}_{11} + 2\widetilde{C}_{44})}\sigma = -\nu\varepsilon_L \tag{2.2.12}$$

Where the Young's modulus Y and the Poisson's ratio (ν) are given by:

$$Y = \frac{\widetilde{C}_{44}(3\widetilde{C}_{11} + 2\widetilde{C}_{44})}{\widetilde{C}_{11} + \widetilde{C}_{44}} \tag{2.2.13}$$

$$\nu = \frac{\widetilde{C}_{11}}{2(\widetilde{C}_{11} + \widetilde{C}_{44})} \tag{2.2.14}$$

The equation 2.2.9 can be rewritten by introducing Y and ν:

$$\varepsilon_{ij} = \frac{1+\nu}{Y}\sigma_{ij} - \frac{\nu}{Y}\sigma_{kk}\delta_{ij} \tag{2.2.15}$$

$$\sigma_{ij} = \frac{Y}{1+\nu}\varepsilon_{ij} + \frac{\nu Y}{(1+\nu)(1-2\nu)}\varepsilon_{kk}\delta_{ij} \tag{2.2.16}$$

Note that we can also define the bulk modulus (K) by considering an hydrostatic compression. In this condition, we have $\sigma_{ij} = \sigma\delta_{ij}$ and $\varepsilon_{ij} = \varepsilon\delta_{ij}$, which lead to $\sigma_{ij} = (3\widetilde{C}_{11} + 2\widetilde{C}_{44})\varepsilon$. We deduce that

$$K = \frac{1}{3}\left(3\widetilde{C}_{11} + 2\widetilde{C}_{44}\right) = \frac{1}{3}\frac{Y}{1-2\nu} \tag{2.2.17}$$

2.3 Experimental design

In this section we will present different mechanical systems that have been used to study the magnetomechanical properties of ferromagnetic thin films on compliant substrates. Two types of experimental design have been developped: i) bending system and ii) piezo-actuation system.

2.3.1 Bending

In bending system, the film is subjected to bending stress which can be either biaxial or uniaxial. Indeed, during this project research, we have performed bending test by gluing the film/substrate system onto curved aluminum blocks of different known radii (uniaxial bending) or onto "ping-pong" ball (equibiaxial bending). In the following subsections, we will give a draft of the bending theory, for more details the readers are referred to [5].

2.3.1.1 Uniaxial Bending

We first consider the bending of an *ad hoc* bar. During a uniaxial bending, the stress tensor is reduced to equation 2.3.1 with only one normal component along the bending axis, and longitudinal strains are developped at the top of the bar.

$$\sigma = \begin{pmatrix} \sigma_{xx} & 0 & 0 \\ 0 & 0 & 0 \\ 0 & 0 & 0 \end{pmatrix} \tag{2.3.1}$$

The longitudinal strains at the top of the bar can be found by analyzing the curvature of the circular block and the associated deformations. For this purpose, let us consider a bar of thickness t with an initial length L_0 at the unstressed state as shown in figure 2.3.1. Under the action of the uniaxial bending, the bar deflects with an arc length L in the xy plane (the plane of bending) and there are axial line that do not extend or contract. It exists a surface somewhere between the top and bottom of the bar in which longitudinal lines do not change in length. This surface, indicated by the dashed line in figure 2.3.1 is called the neutral surface of the beam.

Since the arc length is smaller on one side and larger on the other side of the neutral surface, lines on one side of it lengthen and the others shorten, thereby creating normal strains ε_{xx}. It is reasonable to suppose, therefore, place where the stress is zero as well as for the deformed length than the undeformed length. A such place is called the neutral axis (dashed line in figure) which is an intersection between the neutral surface and any cross-sectional plane[6, 7, 8].

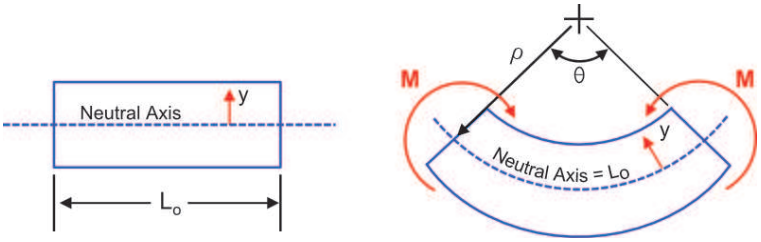

Figure 2.3.1 – An illustration of stress distribution in a bent specimen.

The normal strain ε_{xx} in the bar linearly varies from top to bottom of the beam, as expressed by the following equation:

$$\varepsilon_{xx} = \frac{L - L_0}{L_0} = \frac{(R - y)\theta - R\theta}{R\theta} = -\frac{y}{R} = -\kappa y \tag{2.3.2}$$

In this equation, y is the distance from the neutral axis, R is the radius of curvature, and κ is the curvature (with $\kappa = \pm 1/R$). Note that κ can be either positive or negative. Then, according to Hooke's law, the uniaxial stress is given in terms of the normal strain ε_{xx} by the relation:

$$\sigma = Y\varepsilon_{xx} = -Y\frac{y}{R} = -Y\kappa y \tag{2.3.3}$$

So far we have shown that bending stress cause strain in an *ad hoc* bar. In the following we discuss the case of a thin film (thickness t_f) deposited onto a substrate (thickness t_s). Being given that t_f is generally much smaller than t_s ($t_f \ll t_s$,) one can consider the strain as uniform inside the thin film and take the following value [9, 23]:

$$\varepsilon_{xx}^{top} = \pm\frac{(t_f + t_s)}{2R} \tag{2.3.4}$$

However, Suo *et al.* [23] show that when a metallic film is deposited on a polymer substrate (as the ones studied in the present research project), the high mechanical contrast (film Young's modulus $Y_f \sim 200$ GPa strongly different from the substrate one $Ys \sim 4$ GPa) lead to a change in the neutral surface as compared to a bare substrate. They give the expression of the resulting longitudinal strain at the top surface where the metallic film is confined:

$$\varepsilon_{xx} = \frac{(t+t_s)}{2R}\Gamma \tag{2.3.5}$$

whith

$$\Gamma = \frac{(1+2\eta+\chi\eta^2)}{(1+\eta)(1+\chi\eta)} \tag{2.3.6}$$

Where $\eta = \frac{t_f}{t_s}$ and $\chi = \frac{Y_f}{Y_s}$. The expression of the applied stress is thus simply given by the Hooke's law:

$$\sigma_{xx} = Y_f \varepsilon_{xx} \tag{2.3.7}$$

To illustrate the Suo *et al.* model, we have plotted the Γ variations as function of the film thickness in Figure 2.3.2-a for different values of the substrate Young's modulus (Y_s =4, 10, 20, 50 and 200 GPa). For this purpose, the substrate thickness and the film Young's modulus have been respectively fixed to $t_s = 125$ µm and $Y_f = 200$ GPa. One can see that the variations are almost linear. For $Y_f = 200$ GPa, we found that equation 2.3.5 is reduced to the so-called one (equation 2.3.4) since Γ is constant and equal to unity. For polyimide substrates ($Y_s = 4$ GPa); Γ is higher than 0.99 only for very thin films *i.e.* with thickness $t_f \lesssim 20$ nm. For thicker films, the use of equation2.3.5 is unavoidable; for example, $t_f = 200$ nm leads to $\Gamma \sim 0.93$ which can lead to strains 10% lower than the one expected by using equation 2.3.4. Of course, this effect strongly depends on the bending characterized by the radius of curvature ρ of the whole system (film+substrate). Figure 2.3.2-b presents typical variations of the obtained strain (ε_{xx}) as function of the film thickness for different values of R with $Y_s = 4$ GPa, $Y_f = 200$ GPa and $t_s = 125$ µm. We clearly see that the effect depends on R; for instance ε_{xx} is around 15% lower for a 400 nm film than the value at 20 nm.

2.3.1.2 Equibiaxial bending

We now discuss the case of a thin film deposited on a polymer substrate submitted to an equibiaxial bending [5, 9]. In this case, the stress components σ_{xx} and σ_{yy} are equivalent, i.e $\sigma_{xx} = \sigma_{yy} = \sigma$, the stress tensor is simply given by the following matrix:

$$\sigma = \begin{pmatrix} \sigma & 0 & 0 \\ 0 & \sigma & 0 \\ 0 & 0 & 0 \end{pmatrix} \tag{2.3.8}$$

To experimentally perform an equibiaxial bending, the ferromagnetic thin films were glued on top of spheric plastic ball (ping-pong balls of radius 2 cm). The strains developped at the top of the films are expressed as a function of the radius of the sphere R and the biaxial strain modulus of the film $Y_f^* = \frac{Y_f}{1-\nu_f}$. Moreover, we have adapted the Suo *et al.* modelling by introducing the Γ (see equations 2.3.5 and 2.3.6) coefficient:

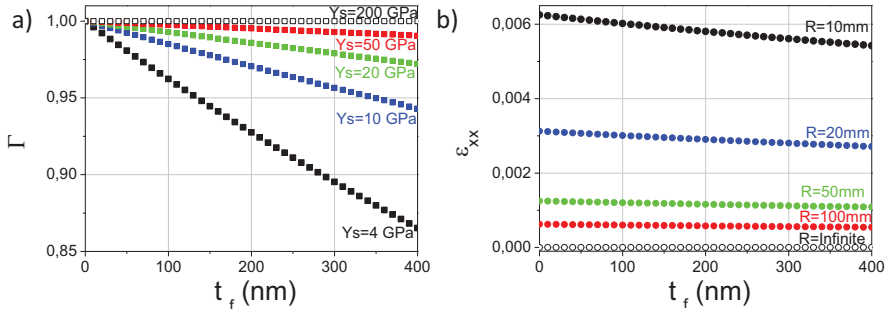

Figure 2.3.2 – a) Variation of Γ as function of the film thickness for different values of the substrate Young's modulus (Y_s =4, 10, 20, 50 and 200 GPa). b) Variation of ε_{xx} as function of t_f for different bending values (ρ =10, 20, 50, 100 and infinite (flat substrate)). In a) and b) the substrate thickness and the film Young's modulus have been respectively fixed to t_s = 125 µm and Y_f = 200 GPa.

$$\sigma = \pm Y_f^* \left(\frac{d_f + d_s}{2R} \right) \Gamma \tag{2.3.9}$$

2.3.2 Piezoelectric Actuation

In the piezoelectric actuation, the films are glued on top of commercially available piezoelectric actuators. In the following subsections, we will give a brief definition of the piezoelectric effect and the description of our systems.

2.3.2.1 Piezolectric Effect

Piezoelectricity stems from the Greek word piezō (πιέζω) or piezein (πιέζειν) which means pressure. It was originally discovered in 1880 by the French physicists Jacques and Pierre Curie. It follows that a piezoelectric material develops a potential across its boundaries when subjected to a mechanical stress (or pressure), called direct piezoelectric effect. The relation between the applied stress on a piezoelectric material and the resulting charge polarization is given by:

$$P_i = d_{ij}\sigma_j \tag{2.3.10}$$

where d_{ij} (C.N^{-1}) are piezoelectric coefficients; d is a third-rank tensor. The charge density-pressure relationship in a typical piezoelectric ferroelectric (e.g. soft Pb(Zr, Ti)O3 ≡ PZT) is hysteretic. Conversely, piezoelectric materials have another interesting property: they change their dimensions (by contracting or expanding) when an electric field $\vec{E}$ is applied to them. This converse piezoelectric effect describes the strain that is developed in a piezoelectric material due to the applied electric field:

$$\varepsilon_j = d_{kj}E_k = d_{jk}^t E_k \tag{2.3.11}$$

where t denotes the transposed matrix. The units of the converse piezoelectric coefficient are m/V. The piezoelectric coefficients d for the direct and converse piezoelectric

effects are thermodynamically identical *i.e.* $d_{direct} = d_{converse}$. The piezoelectric coefficient d can be either positive or negative. It is common to call a piezoelectric coefficient measured in the direction of applied field the longitudinal coefficient, and that measured in the direction perpendicular to the field the transverse coefficient. Other piezoelectric coefficients are known as shear coefficients [11, 13].

Piezoelectric materials are smart materials that can be used as sensor, actuator and control systems. It is a linear effect that is related to the microscopic structure of the solid. The microscopic origin of the piezoelectric effect is the displacement of ionic charges within a crystal structure. In the absence of the external stress, the charge distribution within the crystal is symmetric and the net electric dipole moment is zero. However, when an external stress is applied, the charges are displaced and the charge distribution is no longer symmetric. A net polarization develops and results in an internal electric field. A material can only be piezoelectric if the unit cell has no center of inversion (i.e. non centrosymmetric). It exists 32 crystal classes which are splitted into seven groups (triclinic, monoclinic, orthorhombic, tetragonal, trigonal, hexagonal and cubic) which are associated with the elastic nature of the materials. Only 20 of the 32 classes allow piezoelectric properties.

Finally, piezoelectric materials can be natural or man-made. Among the natural piezoelectric material one can cite: quartz (SiO_2), Rochelle salt, etc. Man-made piezoelectric materials are crystals that are quartz analogs, ceramics, polymers and composites. It exists myriads of man-made ceramics crystals perovskite: barium titanate ($BaTiO_3$); lead titanate ($PbTiO_3$); lead zirconate titanate ($Pb[Zr_xTi_{1-x}]O_3$, $(0 < x < 100)$)–more commonly known as PZT; potassium niobate ($KNbO_3$); lithium niobate ($LiNbO_3$); lithium tantalate ($LiTaO_3$), etc. and other lead-free piezoceramics. We will focus on the PZT piezoelectric ceramic which have been used in the framework of this thesis.

2.3.2.2 PZT piezoelectric Actuator

For the piezolectric actuation mechanical test, the ferromagnetic films are cemented, thanks to an epoxy glue (resine and harder), onto a piezolectric actuator as shown in the figure 2.4.1. The actuator is a commercially available PZT actuator with dimensions $1.8 \times 0.7 \times 0.7$ cm^3 (see figure 2.4.1). A voltage applied across the PZT actuator results in the deformation of the actuator which is then transferred (or not) to thin film. A good contact between the film and the actuator is neccessary in order to completelly transmit the in-plane strains. Owing to the converse piezoelectric effect inherent in piezoelectric materials, a mechanical expansion (resp. contraction) along the dominant elongation direction (along x-axis) when a positive (resp. negative) voltage is applied across it. In particular, a positive voltage results in an elongation with a related uniaxial strain $\varepsilon_{xx} > 0$ along x. Due to elasticity, this tensile strain is accompanied by compressive strains $\varepsilon_{yy}, \varepsilon_{zz} < 0$ along the orthogonal in-plane direction y and the orthogonal out-of-plane direction z [12]. To convert the voltage appplied across the piezolectric actuator into deformations, digital image correlation (DIC) technique has been used and is described in the following section.

2.4 Strain measurements

Different methods have been reported for full-field measurements, speckle interferometry [14], speckle photography [15, 16], speckle-shearing interferometry [17, 18], white-light speckles [19], Moir,... However, each of these methods suffer from stringent stability requirement and time consuming data processing [21]. To address this issue, dial gauges, electrical strain gauges, etc. have also been used. However, these devices measure strain over a very limited gauge length and, as a result, cannot be used for full-field measurements. In this context, digital image correlation (DIC) since its introduction in early 1980s by Sutton *et al.* [22] has become a popular method for the measurement of displacement and strain fields and has been used in variety of area. Recently, the digital image correlation has been used by M. H. Malakooti *et al.* [23, 24] for the characterization of the converse piezoelectric effect by measuring the d_{33} and d_{31} piezoelectric coefficients of a lead zirconate titanate (PZT) material. In the framework of this thesis, the digital image correlation was the preferred technique for a quantitative determination of the displacement and strain fields at the surface of the ferromagnetic thin films deposited on the PZT actuators and submitted to electrical loading [25, 26, 27].

2.4.1 Digital image correlation

In general, the implementation of the DIC method comprises the following three consecutive steps, namely: i) specimen and experimental preparations; ii) recording images of the planar specimen surface before and after loading; iii) processing the acquired images using a computer program to obtain the desired displacement and strains informations. In this section, the basic principles and concepts of DIC used in this research project are described.

2.4.1.1 Basic principle

Digital image correlation is a non-contact and non destructive optical technique for microscale even nanoscale surface displacement and strains of an object under different loading conditions. In digital image correlation a single camera (2D-DIC) or even a couple of camera (3D-DIC) is used to determine the displacement and strain of a planar or non-planar surfaces. It works by doing comparison of set of digitized images of a surface at two different states before deformation (reference image) and after deformation. However, to achieve this, the surface of the studied object has to be randomly spray-painted in order to have a random pattern or must have an intrinsic pattern at its surface. An area of interest (ROI) on the surface of the specimen is selected and subdivided into subsets. Typically, a reference subset of $(2M + 1) \times (2M + 1)$ pixels centred at the current point $P(x_0, y_0)$ from the left image is chosen to find its corresponding location in the right image. Once the location of the target subset in the right image is found, the disparities of the reference and target subset centres can then be determined. As shown schematically in Figure 2.4.2, a set of neighbouring points in a reference subset within the left image are assumed to remain as neighbouring points in the target subset within the right image. Thus, it is reasonable to assume that each of these points $Q(x, y)$ around the subset centre $P(x_0, y_0)$ in the reference subset can be mapped to point $Q'(x', y')$ in the target subset. Myriad of commercial and laboratory-made sofwares based on digital

image correlation are available (GRANU [28], SEPT D [29], NCORR [30], MOIRE [31], MATCHID [32], CORRELI [33], CORRELA [34],...), among them the ARAMIS DIC system (GOM mbH, Germany)[35, 37] has been used during this thesis. It should be noted that the ARAMIS DIC systems operates in both 2D and 3D events.

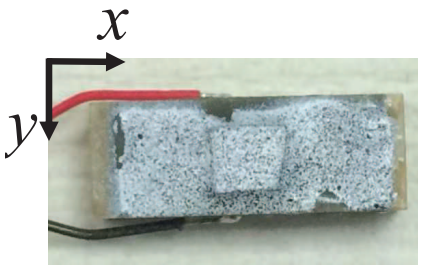

Figure 2.4.1 – Picture showing the ferromagnetic thin film cemented on the PZT-actuator with a randomly speckle pattern of the system ferromagnetic thin film and PZT actuator.

2.4.1.2 Specimen preparation

As previously said, a PZT actuator of geometrical dimensions $1.8 \times 0.7 \times 0.7\text{cm}^3$ commercially available have been used to generate strains inside our films. The displacement and strain fields are determined by DIC calculations. This actuator has property to expand of a certain amount along the elongation axis ($x - axis$) and to compress by around half along the y-axis when a positive voltage is applied. The studied thin films are cemented on the top of the actuator (see figure 2.4.1). For this purpose, we have used an epoxy glue consisting of mixture of a resin and a hardener and then waited 24 hours to be sure that the film is well-adherent to the actuator. Thereafter, for the DIC experiments, the specimen surface must have a random gray intensity distribution (i.e random speckle pattern), a spray paint has been used for this. It is important to point out that the spatial resolution is related to the grains size, the smaller the grains the higher is the resolution. Moreover, whatever the specimen and loading conditions, the grains have to be fixed and well-adherent in order to facilitate the follow-up of the material deformation. Therefore, the surface of the studied object has been randomly spray-painted in order to have a random pattern consisting of black and white random grain field as shown in figures 2.4.1 and 2.4.3.

2.4.1.3 Experimental set-up

During this research project, we have used two different setup to measure the in-plane strains. The first one is composed of a stereo camera system while the second one consists of a unique camera placed in the ferromagnetic resonance setup; this last one will be described in chapter 3. Our stereo system is composed of two CCD cameras mounted on a tripod positioned vertically in top of the film/substrate/actuator system. The field of view is fixed to approximately 22 cm^2. Given the 2448×2050 number of pixels of the cameras, the area per pixel is about 12.5 nm^2. A first image (reference image) is taken at zero applied voltage; then, a sequence of images is taken at different applied voltages

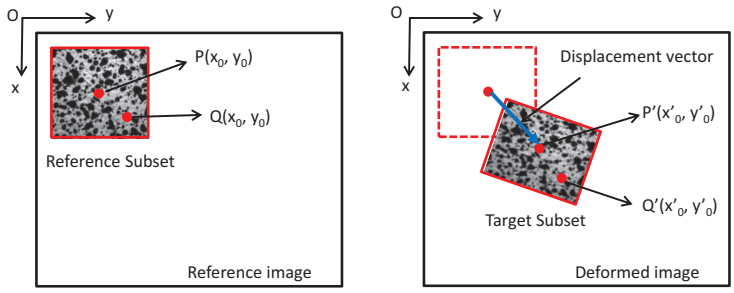

Figure 2.4.2 – Schematic illustration of reference square subset before deformation and a target subset after deformation. Adapted from [36].

and is compared to the reference. The voltage is applied thanks to a KEPCO Bipolar Operational Power Supply (BOP 500M) allowing to apply voltage in the range [-500 V; + 500 V]. However, we have experienced that the voltage limit for our actuator is around 220V. Then, the field strain at the surface of the system is extracted for each applied voltage by performing DIC calculations, which are performed by using the reference image and the different images coming from the sequence. The DIC calculations have been performed by using ARAMIS that is a commercially available software package [35]. From the fields strain, the mean in-plane strains are extracted as function of the applied voltage.

When performing our experiments, images are collected by applying voltages using either a symmetrical path (for instance: -200 V to +200 V and +200 V to -200 V) or non symmetrical path (0 V to 100 V and 100 V to 0 V for instance). The frame is generally of about 0.1 FPS; the step of applied voltage can also be varied. Furthermore, we have estimated statistical errors of our DIC setup by measuring several images in absence of applied voltage; it is estimated to be around 5×10^{-6}. Moreover, different images have been taken as a function of time at 0V after saturating the actuator at 100 V. After approximately 5 h, a difference of about 4×10^{-5} in the in-plane strains values is found; this value rises to 1×10^{-4} after several days (which is relatively high). This difference is due to the training effect of the actuator polarization.

2.4.1.4 Basic results

In this subsection, we present results coming from a Co_2FeAl (CFA) thin film (25 nm) cemented onto a piezoelectric actuator. We have employed our technique to measure the in-plane strains in this system. The voltage was applied by using a non-symmetrical path (0 V to 100 V and 100 V to 0 V) with a 2 V step. Afterwhat, ARAMIS has been used to calculate the DIC in two different (around $3 \times 3\text{mm}^2$) regions: an uncoated area of the actuator and an area located at the top of the CFA film (see figure 2.4.4. Figure 2.4.4 presents the extracted mean in-plane strains ε_{xx} and ε_{yy}. Note that we have also determined the shear strains but their values are found to be negligible in all this research project and will be neglected thereafter [26]. Indeed, similar quasi-homogeneous strain fields as function of the applied voltage have been calculated from the two regions. Thus, we can conclude that a 100% in-plane strain transmission in between the piezoelectric

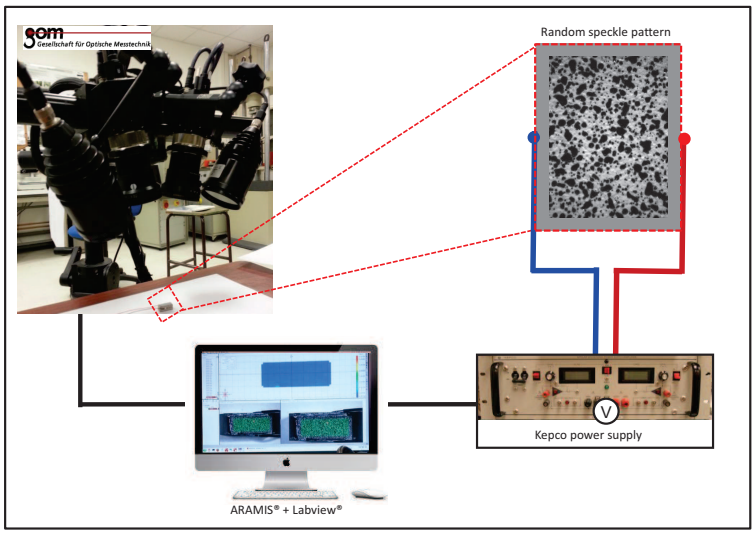

Figure 2.4.3 – Stereo camera experimental set up used during this thesis. The electric field inside the actuator is generated thanks to a voltage applied by using a KEPCO Bipolar power supply. The ARAMIS software is used to analyze the images.

actuator and the film is observed. Non linear variations are observed for both ε_{xx} and ε_{yy}, which is due to the intrinsic properties of the ferroelectric material used in the fabrication of the actuator. One can note that ε_{xx} is found to be positive and ε_{yy} is found to be negative in the voltage range [0–100 V]. Moreover, it is interesting to note that a linear variation of ε_{xx} as a function of ε_{yy} is found $\varepsilon_{xx} \simeq -0.65\varepsilon_{yy}$. The maximum achieved values of ε_{xx} and ε_{yy}, (1×10^{-3} and -0.5×10^{-3} at 100 V, respectively) show that the film is not deteriorated by the plasticity regime because it is obtained for higher values: this is experimentally confirmed by the excellent reproducibility of the experiments (even after several days).

We have also performed similar measurements by using a symmetrical path (-200 V to

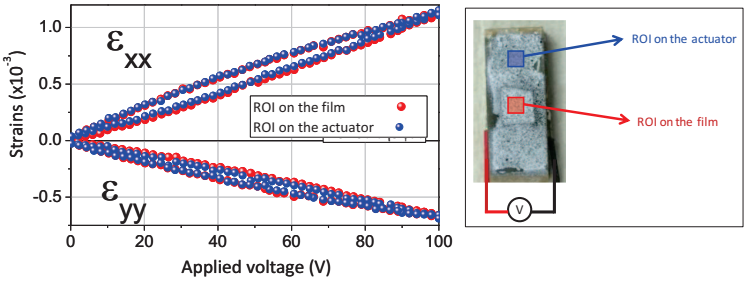

Figure 2.4.4 – Left: mean in-plane strains (ε_{xx} and ε_{yy}) in the film and actuator regions as function of the applied voltage. Right: a sketch showing the selected region of interest (ROI) on the surface of the film and actuator for the analysis of the strain transmission.

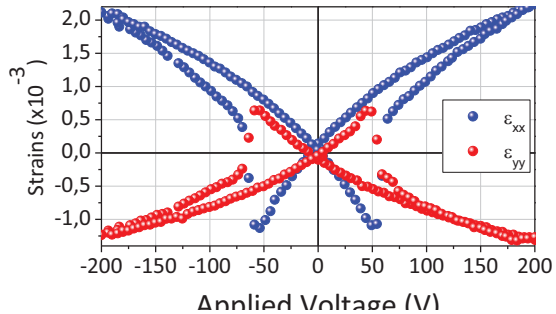

Figure 2.4.5 – Mean in-plane strains (ε_{xx} and ε_{yy}) as function of the applied voltage for a symmetrical cycle an unloading from 200 to −200 V followed by a loading from −200 to 200 V. A Butterfly-like behavior of the curve is observed. This behavior is due to the polarization switching of the piezoelectric actuator.

+200 V and +200 V to -200 V). The classical butterfly-like behavior is well captured for ε_{xx} and ε_{yy} as it is shown in figure 2.4.5. This behavior is due to polarization switching of the piezoelectric actuator. One can see that at about −60 V during unloading and +60 V during loading, the polarisation is switched.

2.4.2 Attainable strains and stresses

In this subsection, we calculate the stresses states attainable by using our mechanical testing (piezoactuation and bending). For this purpose, we continue with the CFA thin film previously studied. In both mechanical tests, we need to know the relation between stresses and strains to calculate the stresses states. X-ray diffraction measurements show that this CFA film is polycristalline and is non-textured, so its elastic behaviour is isotropic. Its elastic parameters $Y_f = 243$ GPa , $\nu_f = 0.27$ will be determined in chapter 4 by using the homogeneization method presented in this chapter. In this condition, the relation between the stress tensor components (σ_{xx}, σ_{yy}) and the measured strains (ε_{xx}, ε_{yy}) is given by the isotropic Hooke's law (see equation 2.2.16). In figures 2.4.6-a and 2.4.6-b, we show the attainable strains and the corresponding stresses for the two different types of mechanical sollicitations. In the bending test, the attainable stresses states are limited by the chosen radius of curvature of the aluminum curved blocks that we have used. The smaller one defined the upper limit. It has a radius $R_{min} \sim 13$ mm which leads to the following stresses state: $(\sigma_{xx}; \sigma_{yy}) = (\pm 1.15; 0)$ GPa and $(\sigma_{xx}; \sigma_{yy}) = (0; \pm 1.15)$. The mechanical stresses states attainable with piezoactuation are limited by the intrinsic properties of the actuator as it can be seen in figure 2.4.6-b where we observe that the piezoactuation exerces biaxial stresses to the films.

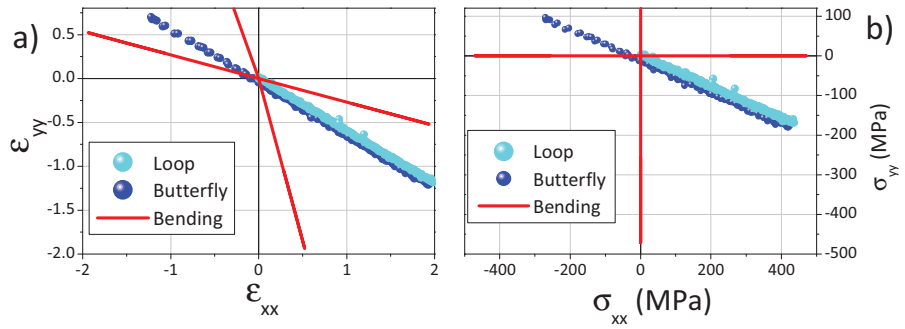

Figure 2.4.6 – a) ε_{yy} as a function of ε_{xx} for piezoelectric actuation ('loop' and 'butterfly' behavior) and unaxial bending. b) σ_{yy} as a function of σ_{xx} for piezoelectric actuation ('loop' and 'butterfly' behavior) and unaxial bending.

Bibliography

[1] P. Hertel, Continuum Physics, GTP, Springer (2012) (Cited on page 40.)

[2] J. F. Nye, Physical Properties of Crystals (1985). (Cited on pages 40 and 41.)

[3] R. M. Jones, Mechanics of composites materials, Taylor&Francis (1998) (Cited on pages 40 and 41.)

[4] D. Sander, Rep. Prog. Phys. **62,** 809 (1999). (Cited on page 41.)

[5] S. Timoshenko and S. Woinowsky-Krieger, Theory of Plates and Shells (Singapore: McGraw-Hill) (1959) (Cited on pages 43 and 45.)

[6] http://continuummechanics.org/beambending.html (Cited on page 44.)

[7] http://emweb.unl.edu/NEGAHBAN/Em325/11-Bending/Bending.htm (Cited on page 44.)

[8] J. M. Gere, Mechanical of Materials, 6th edition (2004). (Cited on page 44.)

[9] H. Gleskova, I.C. Cheng, S. Wagner, J. C. Sturm, Z. Suo,Solar Energy **80** 687–693(2006) (Cited on pages 44 and 45.)

[10] Z. Suo, E. Y. Ma, H. Gleskova, and S. Wagner, Applied Physics Letters **74**, 1177 (1999). (Cited on pages 44, 45 and 90.)

[11] D. Damjanovic, Rep. Prog. Phys. **61** 1267 (1998) (Cited on page 47.)

[12] A. Brandlmaier, Electric-field control of magnetization in multifunctional hybrid devices, Phd Thesis, Technischen Universität München (2011). (Cited on page 47.)

[13] D. Damjanovic, The Science of Hysteresis, Volume 3; I. Mayergoyz and G.Bertotti (Eds.), Elsevier (2005). (Cited on page 47.)

[14] J A Leendertz, Journal of Physics E: Scientific Instruments **3**, 214 (1970). (Cited on page 48.)

[15] E. Archbold, , J. M. Burch and A. E. Ennos, Optica Acta: International Journal of Optics **17**, 883 (1970). (Cited on page 48.)

[16] E. Archbold, and A.E. Ennos, Optica Acta: International Journal of Optics **19**, 253 (1972). (Cited on page 48.)

[17] D.E Duffy, Applied Optics **11**, 1778 (1982). (Cited on page 48.)

[18] Y. Y. Hung, Optics Communications **2**, 132 (1974). (Cited on page 48.)

[19] F. P. Chiang and A. Asundi, Applied Optics, **18**, 409 (1979). (Cited on page 48.)

[20] A. J. Durelli and V. J. Parks, Experimental mechanics **7**, 97 (1967). (Not cited.)

[21] T. C. Chu, W. F. Ranson, M. A. Sutton and W. H. Peters, Experimental Mechanics, Springer (1985). (Cited on page 48.)

[22] M. A. Sutton , W. J. Wolters , W. H. Peters , W. F. Ranson and S. R. McNeill, Determination of displacements using an improved digital correlation method. Image Vis Comput, (1983) (Cited on page 48.)

[23] M. H. Malakooti and H. A. Sodano, Applied Physics Letters **102**, 061901 (2013) (Cited on page 48.)

[24] M. H. Malakooti, A. T. Miller, and H. A. Sodan, Proceedings of SPIE Vol. 9432 943207-1 (Cited on page 48.)

[25] M. Weiler, A. Brandlmaier, S. Geprags, M. Althammer, M. Opel, C. Bihler, H. Huebl, M. S. Brandt, R. Gross, and S. T. B. Goennenwein, New Jounrnal of Physics **11**, 013021 (2009). (Cited on page 48.)

[26] F. Zighem, M. Belmeguenai, D. Faurie, H. Haddadi and J. Moulin, Review of Scientific Instruments, **85**, 103905 (2014). (Cited on pages 48 and 50.)

[27] A. Brandlmaier, S. Geprags, G. Woltersdorf, R. Gross and S. T. B. Goennenwein, Journal of Applied Physics **810**, 043913 (2011). (Cited on page 48.)

[28] F. Lagattu, J. Brillaud, M. C. Lafarie-Frenot, Material characterisation **53**, 17 (2004) (Cited on page 49.)

[29] H. Haddadi, S. Belhabib, Optics and Lasers in Engineering, **46**, 185 (2008). (Cited on page 49.)

[30] See http://www.ncorr.com/ for more information about Ncorr software. (Cited on page 49.)

[31] See http://www.opticist.org/ for more information about Moire software. (Cited on page 49.)

[32] See http://www.matchid.org/ for more information about Matchid software. (Cited on page 49.)

[33] G. Besnard, F. Hild, and S. Roux, Experimental Mechanics **46**, 789 (2006). (Cited on page 49.)

[34] https://www.pprime.fr/?q=fr/la-photomecanique (Cited on page 49.)

[35] See http://www.gom.com/ for more information about Aramis software. (Cited on pages 49 and 50.)

[36] P. K. Panda & B. Sahoo (2015) PZT to Lead Free Piezo Ceramics: A Review, Ferroelectrics, **474:1**, 128-143. (Cited on pages vi and 50.)

[37] GmbH, ARAMIS User Manual - Software v6.1 and higher. Braunshweig Germany (2009).

(Cited on page 49.)

3 Ferromagnetic resonance

Ferromagnetic resonance (FMR) is the resonant absorption of a electromagnetic field by a ferromagnetic material. In a quantum approach, considering the case of a paramagnetic crystal, the application of a static magnetic field H raises the degeneration of the electrons energy levels (spins $\pm 1/2$): it is the Zeeman effect (see figure 3.0.1). The energy difference between two adjacent levels is given by $\Delta E = h\nu_0 = g\mu_B \vec{H}_{eff}$. where μ_B is the Bohr magneton and g is a spectroscopic splitting factor. The superposition of a microwave field h_{rf} in a direction transverse to H can induce electronic transitions between adjacent energy levels. The radiofrequency energy absorbed by the crystal is maximum for $\hbar\omega = \Delta E$: it is the resonance phenomenon. In chapter 1, we have seen (in a classical point of view) that the magnetization precesses around an effective field H_{eff}. In this case, at resonance, the angle of precession considerably increases, which is reflected by a strong absorption of the incident power of the microwave signal.

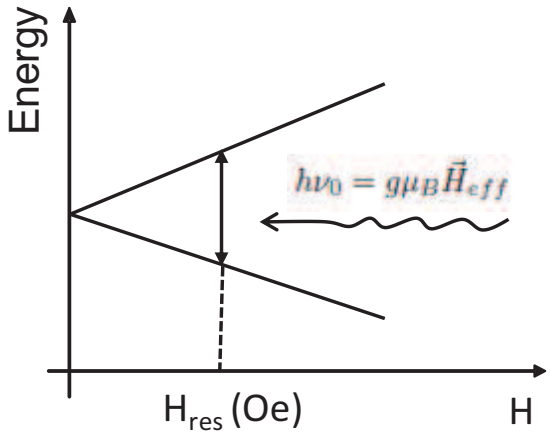

Figure 3.0.1 – Zeemann sub-levels in ferromagnetic resonance spectroscopy.

Contrary to the case of paramagnetic materials, the spins of a ferromagnetic material are strongly coupled *via* the exchange interaction forces. Thus, the observed resonance corresponds to an in-phase macroscopic collective mode precession of the spins around their static equilibrium orientation inside the magnetic field. The ferromagnetic resonance for the usual ferromagnetic materials is typically in the microwave domain (1-100 GHz). It allows a detailed study of the magnetic properties of the ferromagnetic materials.

Historically, FMR is the oldest and most widely used technique to study the magnetization dynamics in thin ferromagnetic films[1, 2, 3]. This technique consists of placing the magnetic sample inside a resonant cavity in the microwave domain. The working frequency is then fixed: it is that of a eigen mode of the cavity (typically from 1 GHz

to 100 GHz). The cavity is excited *via* a waveguide at the working frequency and the reflected power is measured as a function of the external static magnetic field applied to the sample. When the frequency of the studied magnetic mode coincides with that of the cavity, the power absorbed has a maximum, which corresponds to a minimum of reflected power. The main advantage of this technique is its sensitivity. Indeed, despite the small volume occupied by the magnetic material inside the cavity, the quality factors of a few thousand reached for this type of cavity made it possible to measure the dynamics of magnetic films whose thicknesses are of the order of a nanometer. However, this technique has the disadvantage of a fixed working frequency and limits, for instance, the broadband study of damping phenomena, which can impede a good understanding of the involved mechanisms.

This is the reason why we have adopted the broadband (0.01-20 GHz) FMR technique despite the lower sensitivity, as compared to "classical" FMR, to study the magneto-mechanical properties of our thin films. Actually, our broadband FMR offers a sensitivity allowing to detect a net magnetic moment down to 10^{-5} emu which is sufficient to detect a signal in our films. Furthermore, since we aspire to study the magneto-mechanical properties of magnetic thin films, ferromagnetic resonance has been combined with DIC to simultaneously measure in-plane displacement and strains fields. As a consequence, this present chapter is devoted to the presentation of our FMR setup.

3.1 Experimental set-up

A micro-strip ferromagnetic resonance (FMR) has been used during this thesis to carry out all the FMR absorption measurements. The basic components of our FMR spectrometer are shown in figure 3.1.1. The spectrometer utilizes a matched impedance microstrip (MS) line (Z = 50 Ω) to avoid losses. The MS line is suspended between the pole pieces of an electromagnet that is capable of generating up to 20 kOe magnetic fields. The magnet supplies the required uniform, dc magnetic field $\vec{H}_0$. A 83752B synthesized sweeper (0.01-20 GHz) or Agilent N5230A VNA vector analyzer (0.01-40 GHz) generates microwaves that travel down a coaxial cable to the MS-transmission line where some of microwave energy are absorbed by the specimen. The transmitted microwave beam travels back along the coaxial cable to a Schottky diode whose output voltage, V_t, is a function to the amplitude of the transmitted microwave electric field, e_t. The data collection system is dedicated to measure the variation of this diode voltage as a function of the applied magnetic field $\vec{H}_0$. The variations in the diode voltage that are due to changes in the energy absorption by the magnetic sample as $\vec{H}_0$ is swept through $\vec{H}_{res}$ are small and superimposed on a large constant background. In order to emphasize the variations of V_t with $\vec{H}_0$, the applied dc field is weakly modulated at 170 Hz and a lock-in amplifier is used to detect and amplify the 170 Hz component of the diode voltage.

After demodulation, the resulting signal is a first derivative FMR spectrum. Then, the output of this amplifier is connected to a data collection computer over an IEEE-488 data bus. All units are controlled by the personal computer *via* IEEE-488 bus. The control program is written using the LABVIEW graphical programming language. The program runs under WINDOWS and provides flexibility for a real time control of the magnetic field sweep direction, sampling time, data acquisition in real time and visualization. Therefore, the microwave frequency is kept constant and the applied magnetic field is varied over a

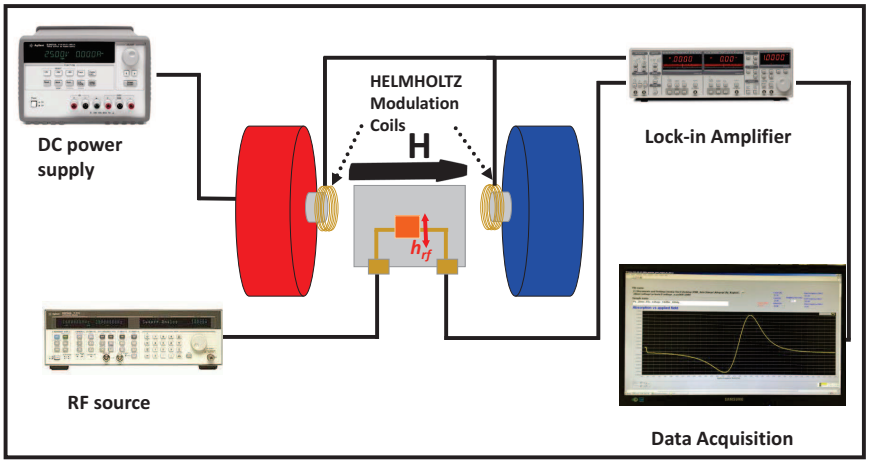

Figure 3.1.1 – Representation of the FMR absorption spectrum which is a Lorentzian and its derivative.

field range in which microwave absorption is expected. This is called sweep-field FMR. Indeed, it is also possible to attain the resonance by fixing the external field ($\vec{H}_0$) and vary the frequency (f_0) (or in other words, the sweep-frequency mode). Each of the enumerated modes has its advantages and drawbacks. For instance, in swept-field mode the magnetic state of the ferromagnetic specimen is disturb. So if one want to study the magnetic properties without changing the magnetic states of the sample (for weak strip domains samples for instance), it is more interesting to use the FMR in its frequency sweep mode. Both of these modes will be used later in chapter 7 to observe the rotation of the magnetization direction under the application of an applied voltage.

3.1.1 Microstrip lines

The first RF and microwaves systems relied on waveguide, coaxial transmission lines, etc. These last were expensive, needed shielding and are difficult to fabricate. To tackle the issues, planar transmission lines such stripline, microstrip (MS) line, slotlines, coplanar waveguide and several others related planar structures have been developed. Microstrip line is one of the most popular types of planar transmission lines due to the ease in which they are fabricated and their easy integration with other microwave devices. So, the MS line has been chosen in this research project to couple the microwaves to the ferromagnetic specimen in the FMR experiment. A typical sketch of the microstrip line is shown in figure 3.1.2-a. A conductor of width W is printed on a thin, grounded dielectric substrate of Al $_2O_3$ with a thickness d and relative permittivity ϵ_r; a sketch of the field lines is shown in figure 3.1.2-b . The exact fields of a microstrip line constitute a hybrid TM-TE wave, however when the dielectric substrate is electrically very thin (d$\ll$ λ) the fields are quasi-TEM. For a microstrip with small insertion loss, a matched 50 Ω transmission line should be considered. Thus, characteristic equations; effective dielectric constant ϵ_{eff} and characteristic impedance of the Z MS lines has approximatively the form [7, 8, 9]:

$$\epsilon_{eff} = \frac{\epsilon_r + 1}{2} + \frac{\epsilon_r - 1}{2} \frac{1}{\sqrt{1 + \frac{12h}{W}}} \tag{3.1.1}$$

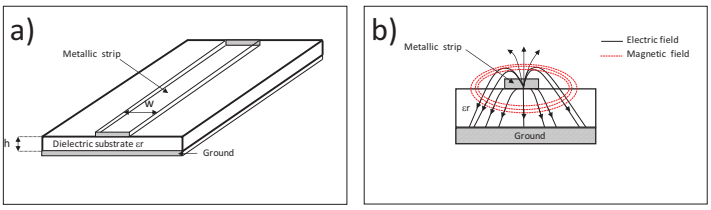

Figure 3.1.2 – A sketch of a microstrip transmission line with (a)the geometry and (b) the electric and magnetic fields lines.

The effective dielectric constant can be interpreted as the dielectric constant of a homogeneous medium that equivalently replaces the air and dielectric regions of the microstrip line. For a given dimension of the microstrip line the characteristic impedance Z_C can be expressed as follow:

$$Z_C = \begin{cases} \frac{60}{\sqrt{\epsilon_{eff}}} \ln\left(\frac{8d}{W} + \frac{W}{4d}\right) & \text{for} \frac{W}{d} \leqslant 1 \\ \frac{120\pi}{\sqrt{\epsilon_{eff}}[W/d + 1.393 + 0.667 \ln(W/d + 1.444)]} & \text{for} \frac{W}{d} \geqslant 1 \end{cases} \tag{3.1.2}$$

3.1.2 Lock-in detection technique

With our FMR technique, the small variations in the Schottky diode voltage that are due to changes in the energy absorption by the thin film as H is swept through H_{res} are measured. In order to enhance the signal to noise ratio (S/N), a modulation and lock-in detection techniques are necessary.

3.1.2.1 Lock-in in phase

To dissociate the FMR signal from noise and interferences sources that are overwhelmed in any laboratory experiment, a phase sensitive detection technique has been used. The phase sensitive detection (PSD) amplifier operates by multiplying two signals together and thus allows a conversion of the alternating input signal into a DC output one. Considering a sinusoidal input signal:

$$V(t) = V_0 \sin(\omega t) \tag{3.1.3}$$

The PSD amplifier has an integrated reference signal, considering this reference signal as being:

$$V_R(t) = V_{R0} \sin(\Omega t + \phi) \tag{3.1.4}$$

The product of the two signal from (3.1.3) and (3.1.4) gives beats at the sum and difference of the frequencies :

$$V_{PSD} = V(t)V_R(t) = \frac{V_0 V_{R0}}{2}\{\cos[(\omega - \Omega)t + \phi] - \cos[(\omega + \Omega)t + \phi]\} \tag{3.1.5}$$

The PSD amplifier or lock-in amplifier is sensitive to signals that have the same frequency and phase than the reference frequency. Any signals that doesn't fulfilled this conditions are suppressed. For this, a low-pass filter with a cutoff frequency $\frac{\omega}{2}$ or lower is used. So, the signal of the lock-in is given by:

$$V_{PSD} = \frac{V_0 V_{R0}}{2}\cos(\phi) \tag{3.1.6}$$

The sensitivity of the FMR signal can be increased by several order of magnitude when the lock-in is accompanied by a field modulation.

3.1.2.2 Field modulation lock-in technique and derivative spectrum

In our setup, a small amplitude modulation of the static magnetic field H_0 is carried out to limit the noise-contributing components to frequencies very close to the modulating frequency. Commonly, the *ac*-modulation field h_{ac} with a modulation frequency ω is achieved by placing Helmholtz coils on the two sides of our sample, i. e. along the axis of the static magnetic field. Then, the modulation field superimposed to the static leads the following:

$$H(t) = H_0 + h_{ac}\cos(\omega t) \tag{3.1.7}$$

The total power absorbed by the thin film determines the amplitude of the FMR signal (reflected beam). The FMR absorption signal, V_{FMR} varied as a function of the field $H(t)$ and is given by:

$$V_{FMR}(H(t)) = V_{FMR}(H_0 + h_{ac}\cos(\omega t)) \tag{3.1.8}$$

A Taylor expansion of the FMR signal at the vicinity of the static field H_0 leads to the equation:

$$V_{FMR}(H(t)) = V_{FMR}(H_0) + \frac{dV_{FRM}}{dH}h_{ac}\cos(\omega t)) + \dots \tag{3.1.9}$$

The FMR signal $V_{FMR}(H(t))$ is then multiplied by the reference signal V_{ref}=$\cos(\omega t + \phi)$ which have the same frequency than the modulation field ω, but with a phase ϕ. Then, we have the following equation:

$$V_{FMR}(H(t)) \times V_{ref} = V_{FMR}(H_0)\cos(\omega t + \phi)\frac{dV_{FRM}}{dH} + h_{ac}\cos(\omega t))cos(\omega t + \phi) + \dots \tag{3.1.10}$$

$$= V_{FMR}(H_0)\cos(\omega t + \phi) + \frac{1}{2}\frac{dV_{FMR}}{dH}h_{ac}\cos(\phi) + \frac{1}{2}\frac{dV_{FMR}}{dH}h_{ac}\cos(\omega t + \phi) + \dots$$

Finally the signal is subjected to a low-pass filtering with a cutoff frequency between 0 and $\frac{\omega}{2}$. In this case, the time-dependent terms (first and third terms) in equation

3.1.10can be eliminated. The second term $\frac{1}{2}\frac{dV_{FMR}}{dH}h_{ac}\cos(\phi)$ is constant and is proportional to the derivative of the input signal. Therefore FMR signal typically measures the derivative of $\frac{dV_{FMR}}{dH}$ as a function of H [4, 5] .

In FMR, we measure either the microwave power absorbed by a specimen as a function of an applied dc magnetic field, H, or the derivative of the absorption (as in our case) with respect to H. The resulting curve is described by a resonance field, H_{res}, that corresponds to maximum power absorption, and by an absorption linewidth, ΔH. The FMR absorption signal of a ferromagnetic thin film is a function of the applied field H and intrinsic magnetic properties of the film. The latter include the magnetic anisotropies, the spectroscopic $g-$factor, the magnetic damping parameter (that is responsible for the finite linewidth ΔH), and the quantity of interest such as the saturation magnetization. A typical FMR spectra is represented in figure 3.1.3.

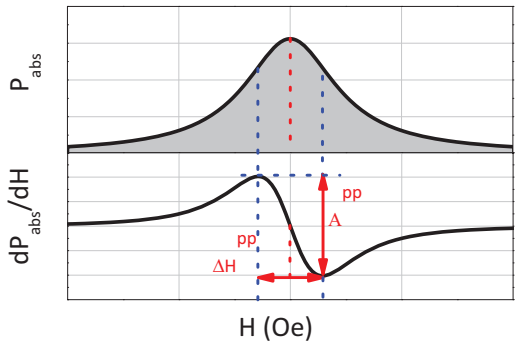

Figure 3.1.3 – An illustration of a typical FMR spectra: a Lorentzian profile of the absorption power and a derivative of a Lorentzian profile when a modulation field is used.

3.2 Lock-in parameters optimization

3.2.1 Amplitude of the modulation field

In ferromagnetic resonance the modulation phase, modulation frequency, modulation amplitude, time constant and microwave power strongly influence the spectra. Then, to obtain a reliable physical results all those different parameters have to be tailored.

From equation 3.1.10, we have derived that the FMR signal $\frac{1}{2}\frac{dV_{FMR}}{dH}h_{ac}\cos(\phi)$ is related to the amplitude of the modulation field h_{ac}. By analyzing this equation, we can discuss the impact of the modulation on the FMR spectra. At low modulation amplitudes (viz. when the modulation amplitude is small compared the linewidth ΔH of the FMR spectra), as the amplitude of the magnetic field modulation is increased, the amplitude of the FMR signals increases (see figure 3.2.1). For small modulation amplitude, the S/N increases linearly with the modulation amplitude, as shown in figures 3.2.1-a and 3.2.1-b. However, if the modulation amplitude is too large (viz. larger than the linewidth ΔH of the FMR signal), the FMR signal broadens and becomes distorted leading to a lost of valuable information [6].

In the framework of this thesis, with regard to quantitative FMR measurements, the details of lineshape and intensity are crucial, then the spectrum has to be obtained un-

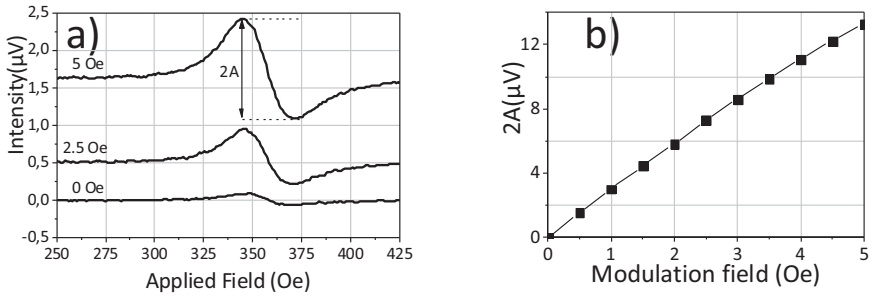

Figure 3.2.1 – The variation of the amplitude of the FMR signal with the modulation voltage with (a): The signal shape of the FMR signal as a function of increasing modulation amplitude;(b): the amplitude (2A) of the FMR spectra with the modulation voltage.

der conditions such that do not distort the spectrum. For this, the reference phase and modulation amplitude need to be carefully calibrated to obtain maximum sensitivity, minimum distortion, and quantitatively reproducible measurements. We have firstly calibrated the amplitude of the modulation amplitude and then the phase difference between the reference signal and the modulated FMR signal. In the first step of calibration of the modulation amplitude, the voltage of the lock-in amplifier is varied until the modulation amplitude is maximized. The maximum voltage of the lock-in amplifier is 5 V with a corresponding modulation amplitude of the ac modulation field of 5 Oe.

3.2.2 The lock-in phase

Once the modulation amplitude has been calibrated (here the amplitude is 5 Oe), the reference phase is easily calibrated by studying the phase angle dependence of the FMR signal intensity (see figure 3.2.2). The intensity of the FMR signal is proportional to the cosine of the phase difference between the reference signal and the modulated FMR signal (see equation 3.1.10). Then, the intensity which related to cosine function changes rapidly with respect to the phase angle at 90°. In the calibration process, spectra are acquired at several different values of the reference phase from 0° to 360° in order to find the phase angle resulting in a maximum signal intensity of the spectra at the modulation frequency (here the phase of the lock-in was locked to 70°). The Figures 3.2.2-b and 3.2.2-c are illustrations of the evolution of the amplitude of the FMR signal as a function the phase of the lock-in amplifier. We can see that the amplitude varies in a cosines way with the phase with a maximum at 70° drops to zero for at 160° before changing in sign beyond. In the figure 3.2.2-a typical FMR spectra recorded at different phases of the lock-in: 90° (black curve), 160° (red curve) and 250° (blue curve). A phase change of the FMR spectra can be noticed between the spectra recorded at 90° and 250° ($\cos(180^{\circ}) = -1$). It is important to point out the fact the experimental conditions who have considerable influence on the phase difference between the modulated FMR signal and the reference signal. For instance, the length of the cable leading to the modulation coils, the inductance of the coils, the gain setting of the modulation amplifier, just to name a few.

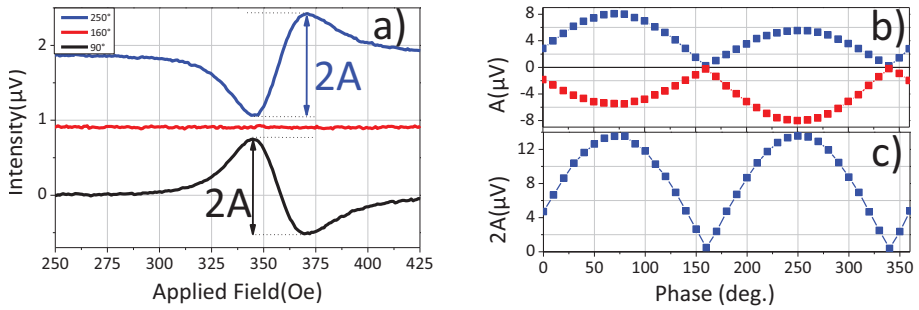

Figure 3.2.2 – The variation of the FMR signal amplitude with the phase of the lock-in amplifier.

3.2.3 The lock-in frequency

It is important to point out the fact that the choice of the modulation frequency is of paramount importance since a small modulation frequency do not dispose $1/f$ noise since this noise is high at low frequency. Consequently, for a better S/N a higher modulation frequency is required. This effect can be seen in figure 3.2.3-a.

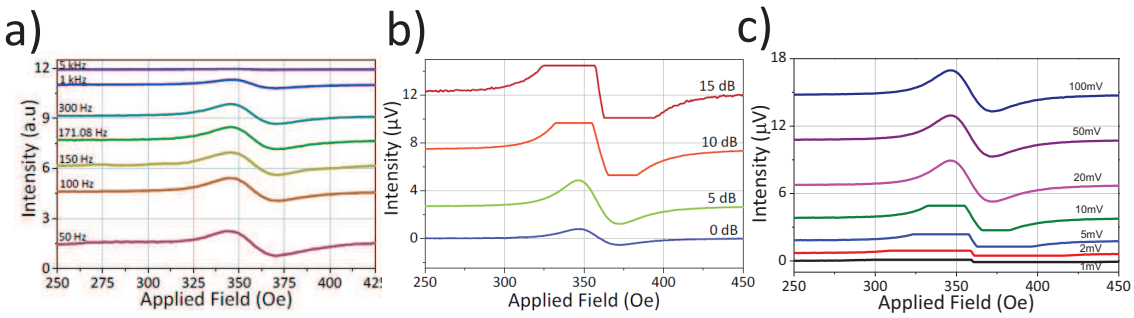

Figure 3.2.3 – a) Influence of the modulation frequency b) the rf power on the FMR spectra and the sensitivity of the lock-in detection amplifier.

3.3 FMR signal optimization

3.3.1 Time constant and sweeping time

The time constant of the lock-in amplifier play an important role for the improvement of the FMR signal sensitivity. It affects the level in the spectrum, hence the user has to be careful in the choice of the time constant. The noise is filtered out by increasing the time constant of the low-pass filter, as a result the response time of the detection circuit is slowed down. Increasing the time constant leads to a decrease of the noise level. If a long time constant is needed to dissociate a weak signal from noise, a slower scan rate must be used i.e a longer sweeping time.

3.3.2 Microwave power

In FMR spectroscopy, a Schottky barrier diode is often used to detect the transmitted signal. However, at higher frequencies the $1/f$ detector noise, which is inversely proportional to the frequency declines their performance. An excessive use of the microwave power could damage the Schottky diode and consequently it loses their sensitivity. To make sure that this does not happen, the microwave power has to be moderately chosen. To illustrate the effect of the microwave power the FMR lines, we have recorded FMR spectra at different microwave power. One can note that from figure 3.2.3-b, high microwave power saturates the spectra. In such condition no quantitative informations can be extracted from the spectra. The saturation must be avoided for an accurately measurement of the intensities, linewidths, etc. of the FMR signal by decreasing the power.

3.3.3 Sensitivity of the FMR spectra

The sensitivity of the FMR spectra dependent strongly on the the angle between the the magnetic field $\vec{H}$ and the microwave field $\vec{h}_{rf}$. When the specimen is placed in the center of the microstrip transmission and the magnetic field $\vec{H}$ applied along x (see figure 3.3.1-b, the microwave field $\vec{h}_{rf}$ created around it is perpendicular to the magnetic field $\vec{H}$ and a strong torque is exerted on the magnetization leading then to a maximum of the FMR signal (see figure 3.3.1-a). However, when the specimen is positioned in the edges of the microstrip transmission line and the magnetic field $\vec{H}$ is applied along x , the microwave field $\vec{h}_{rf}$ is parallel in this situation to magnetic field and a weak torque is exerted on the magnetization, consequently the resulting FMR signal is minimal (Low sensitivity). We will use later this selection rule in chapter 7 using the ferromagnetic resonance in its frequency mode to observe the magnetization rotation.

It is important to point out that the microstrip line is not really homogeneous, for example FMR measurements with the specimen in different zone of the MS-line (the edges) show a small shift of few Oersted of the FMR lines. To tackle this issue, it is advisable to effectuate the FMR measurements placing the specimen at the center of the microstrip line.

3.4 *In-situ* mechanical testing

For the *in situ* study of the magnetoelastic effect in ferromagnetic thin films, the ferromagnetic resonance (FMR) is combined with the mechanical testing we have presented in the chapter 2 : bending or piezoelectric actuation. Figures 3.4.1 show the set up we have used in the framework of this thesis. The principle is to deform the magnetic thin film by applying a voltage across the piezoelectric actuator or to apply bending stress with circular bended-blocks of various curvature radii. The influence of the stresses induced on the uniform precession mode of the ferromagnetic resonance is manifested by a shift of the ferromagnetic resonance spectra, as we will see in the next subsection.

Figure 3.4.1 shows the setup used when performing bending test. When using piezoactuation, our setup combines FMR and DIC techniques. As shown in top figure 3.4.1, the piezoelectric media is connected to a Keithley power supplier (Model 2400) allowing to apply DC voltages in the range [−200 V;+200 V] with 0.001 V resolution. For each

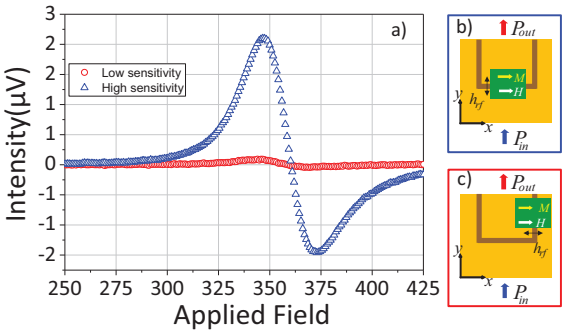

Figure 3.3.1 – Illustration of the FMR spectra sensitivity according to the angle between the magnetization and the rf field. a) A low sensitivity with minimal FMR signal in which the angle between the pumping field and the static one is equal to zero leading to a weak torque exerted by the microwave driven on the magnetization. b) High sensitivity with a maximal FMR signal in which the pumping field is directed perpendicular to the magnetization leading to a strong torque exerted by the microwave driven field on the magnetization.

applied voltage, a FMR spectrum and an image of the top surface of the sample are recorded (note that the spectrum recording takes from 1 min to several hours depending on the magnetic field step and on the total width of the spectrum). The images recording at each step will serve to determine the in-plane field strains. Furthermore, being given the initial "homogeneous" surface of the sample, a speckle pattern has been spray painted in order to generate a contrast which will serve to calculate the strain fields (an image of a typical speckled pattern (spray-painted) is presented in bottom figure 3.4.1-c. In our setup, the images are recorded thanks to a 2048×2048 pixels CCD AVT-Pike f421b camera vertically positioned in the top of the surface sample. The objective lens has been chosen in order to be sufficiently far from the electromagnet (20 cm) with a field view around 1×1 cm^2 as shown on figure 3.4.1-c). The strain fields calculations (from the different images) have been perfumed by digital image correlation thanks to the Aramis software .

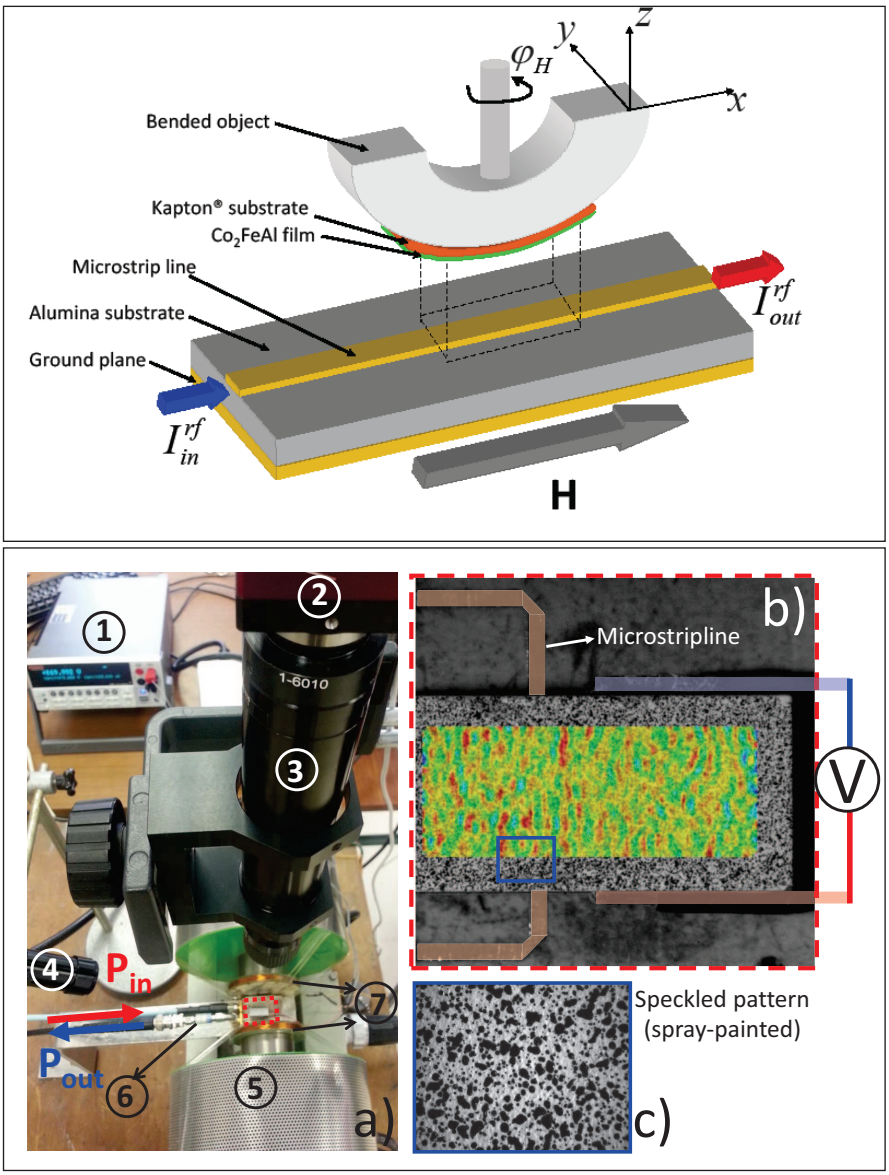

Figure 3.4.1 – Top figure: sketch of the microstripline resonator allowing for the resonance field detection of the bended CFA film deposited onto flexible substrate. I_{rf}^{in} and I_{rf}^{out} correspond to the injected and transmitted radio frequency current (fixed at 10 GHz thereafter). The static magnetic field $\vec{H}$ is applied along the microstripline. Bottom figure: (a) setup image of the combined FMR/DIC experiment. The circled numbers correspond to: (1): Keithley Model 2400; (2): CCD camera (AVTPike- f421b); (3): objective lens for the CCD camera; (4): white light source; (5): electromagnet; (6): Schottky detector; and (7): modulation coils. P_{in} and P_{out} are the injected and transmitted radio frequency current. (b) Zoom in showing the sample mounted onto the microstripline. A typical calculated strain field map is present at the top of the sample. (c) Zoom in of the speckled pattern (spray-painted) at the top of the sample necessary for the strain fields calculations.

Bibliography

[1] J. Lindner and K. Baberschke, *In situ* ferromagnetic resonance: an ultimate tool to investigate the coupling in ultrathin magnetic films, Journal of Physics: Condensed Matter **15**, 193 (2003) (Cited on page 56.)

[2] M. Farle, Ferromagnetic resonance of ultrathin metallic layers, Rep. Prog. Phys. **61,** 755 (1998) (Cited on page 56.)

[3] Z. Celinski, K. B. Urquhart and B. Heinrich, Journal of Magnetism and Magnetic Materials **166**, 6 (1997) (Cited on page 56.)

[4] C.-K. Lo, "Instrumentation for Ferromagnetic Resonance Spectrometer," in Ferromagnetic Resonance - Theory and Applications, O. Yaln, Ed. InTech, 2013. (Cited on page 61.)

[5] S. V. Vaseghi, Advanced Digital Signal Processing and Noise Reduction Fourth Edition, John Wiley&Sons, Ltd. ISBN: 978-0-470-75406-1, 2008 (Cited on page 61.)

[6] Reijerse, E. J. High-Frequency EPR Instrumentation Appled Magnetic Resonance, 2010. (Cited on page 61.)

[7] M. D. Pozar, Microwave Engineering, 4th Edition., Wiley. (Cited on page 58.)

[8] J. S. Babgy, C. H. Lee, D. P. Nyquist and Y. Yuan Propagationregimes on integrated microstrip transmission lines IEEE Transactions on microwave theory and techniques, Vol. 41. No. 11. November 1993. (Cited on page 58.)

[9] E. Salahun, G. Tann. Quc, M. Le Floc'h, A. L. Adenot and O. Acher, Application of ferromagnetic composite in different planar tunable microwaves devices, Microwave and Optical Technology Letters, Vol. 30. No. 4, August 20 2001.

(Cited on page 58.)

4 Magnetoelastic properties of high potential alloys for spintronics

The recent development of magnetic devices, such as giant magnetoresistance, magnetic tunnel junctions or magnetoimpedance systems [1, 2, 3, 4, 5, 6, 7, 8], fabricated on flexible substrates leads to the need to properly scrutinize the strain effect on the static and dynamic magnetic properties. Indeed, these devices are made by depositing a metallic medium (films or nanostructures) onto a flexible system for which a slight bending effort can lead to high in-plane uniaxial or biaxial stresses during their usage. Indeed, these stress and strain fields modify the static magnetization distribution inside nanostructures [9] and induce non-negligible planar magnetic anisotropies in thin films that are undesirable for some applications [6]. For these applications, it is of high importance to develop flexible systems with high potential alloys for spintronics.

Co-based Heusler alloys such as Co2FeAl (CFA) are an interesting class of materials having a very high Curie temperature and a half-metallic character of their spin-split band structure (metallic behavior for one spin component, and insulating behavior for the other one), as predicted theoretically by calculations. Such materials may exhibit a 100% spin polarization at the Fermi level and they are therefore emerging as potential candidates for a variety of applications such as magnetic sensors and magnetic memories. However, despite their incontestable potentiality, Co-based Heusler alloys are still rarely used in flexible systems and their magnetoelastic properties are poorly known.

On the other hand, CoFeB thin films have attracted much attention from researchers in spintronics, especially after the accessions of very high values of tunnel magnetoresistance ($>$70%). The main application lies in the development of basic tunnel junctions of this material. However, to expand the application scope of these CoFeB-based tunnel junctions, it is also crucial to study other properties than simple magnetoresistance, such as the magnetostrictive effects for magnetic sensing application. Indeed, a strain gauge is a sensor whose resistance varies with applied force; it converts force, pressure, tension and weight into a change in electrical resistance which can then be measured. Hence, the high magnetoresistance value of tunnel junctions made of CoFeB offers the potential of developing strain gauges of high sensitivity. Thus, the joint use of magnetoelastic properties and magnetoresistance can be applied to connect electrical resistance and elastic strains. However, to envisage such developments, it is important to know the relationship between strains, stresses and magnetic anisotropy in those alloys.

Our developed technique, described in chapter 3, has been used to quantitatively determine the strain effect on magnetic properties of $Co_{40}Fe_{40}B_{20}$ and Co_2FeAl thin films. Ni thin films, whose properties are well known, has also been studied to validate the proposed approach. All the films have been deposited on Kapton® substrate (thickness of $t_s \sim 125$ µm) by magnetron sputtering with a base pressure lower than 2×10^{-8} Torr. The Ni and CFA films are found to be polycrystalline with no strong preferred

orientations by x-ray diffraction; the CFB film is amorphous. As a consequence, we will consider that the elastic and magnetoelastic properties are isotropic.

4.1 Beforehand characterization

This section is devoted to the "standard" FMR characterization of the different thin films, *i. e.* in absence of applied strains. In this condition, we are able to determine some parameters which will be useful in the quantitative study of the magneto-mechanical properties of those thin films. In absence of applied strains, the frequency of the uniform precession mode is expected to only depends on the gyromagnetic factor γ, the saturation magnetization M_s and the possible presence of in-plane and out-of-plane magnetic anisotropies. The presence of in-plane anisotropies could be easily detected by measuring the in-plane angular dependence of the uniform precession mode. However, the presence of out-of-plane anisotropies is more complex to detect and needs the determination of the saturation magnetization with another technique (such as vibrating sample magnetometry). Indeed, with FMR, it is impossible to discriminate the out-of-plane anisotropy field ($H_\perp$) from the demagnetization contribution associated to the thin film geometry ($4\pi M_s$) because the resonance frequency of the uniform mode depends on $4\pi M_s - H_\perp$. It should be noted that this last term is generally called effective magnetization $4\pi M_{eff} = 4\pi M_s - H_\perp$. During this research project, we have verified that most of our films do not present such a contribution. For the sake of brevity, we will say that the saturation magnetization has been determined by FMR even if it is more complex.

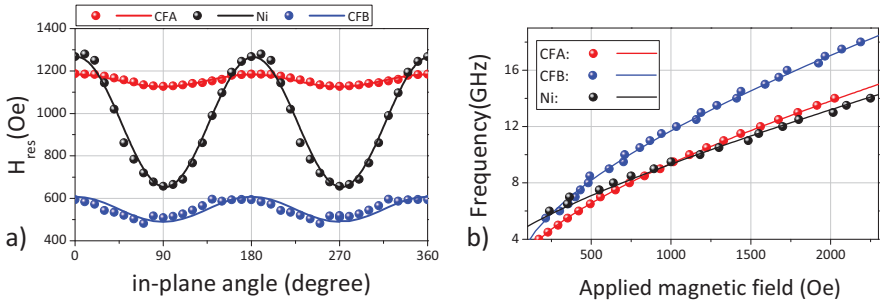

Figure 4.1.1 – a) Angular dependence of the resonance field as a function of in-plane angle for the different films. b) Frequency dependence as function of the applied magnetic field for the different films. In a) and b): $Co_{40}Fe_{40}B_{20}$(blue) and Co_2FeAl (red) and Ni (black). The solid lines correspond to fits of the experimental data using equations 4.2.3 and 4.1.3.

We always begin the characterization by measuring the angular dependence of the resonance field to see the eventual presence of in-plane anisotropies. Figure 4.1.1-a) presents such a dependence measured at 8 GHz in the different films. We clearly note the presence of a second order anisotropy (uniaxial). It should be noted here that all the studied films can be considered as isotropic in a mechanical point of view since they are polycrystalline with no preferred orientations (Ni and CFA) or are amorphous (CFB). As a conclusion, no macroscopic magnetocrystalline contribution is expected. Thus, this anisotropy; which is quite high in the Ni film; should have another origin. We will see

in Chapter 5 that it is due to a slight curvature along a given direction which leads to a bending of the film/substrate system. In the following, this uniaxial anisotropy will be fitted by using an *ad hoc* uniaxial anisotropy field (H_u) characterized by an anisotropy constant K_u with $H_u = \frac{2K_u}{M_s}$ [1]. In order to quantitatively determine M_s, γ and H_u, we need now to measure the frequency dependence of the uniform along the easy and/or hard axis and to fit the experimental to a model. Figure 4.1.1-b) shows the frequency dependencies of the uniform mode along the easy axis which corresponds to the minimum of the H_{res} variation in figure 4.1.1-a) (90 degree) . We need now to fit the experimental data presented in those figures (4.1.1-a) and 4.1.1-b)) by the following model to extract M_s, γ and H_u. The theoretical expression of the uniform mode is determined thanks to the Smith and Beljers formulation:

$$\left(\frac{2\pi f}{\gamma}\right)^2 = \left(\frac{1}{M_s \sin\theta_M}\right)^2 \left(\frac{\partial^2 F}{\partial\theta_M^2}\frac{\partial^2 F}{\partial\varphi_M^2} - \left(\frac{\partial^2 F}{\partial\theta_M \varphi_M}\right)^2\right) \tag{4.1.1}$$

In the above expressions θ_M and φ_M stands for the polar and azimuthal angles of the magnetization $\vec{M}$; γ is the gyromagnetic factor; f is the driving frequency and F is the following magnetic energy density:

$$F = F_{zee} + F_{dip} + F_u \tag{4.1.2}$$

Where $F_{zee} = -\vec{H}\cdot\vec{M}$ is the Zeeman energy where $\vec{H}$ is an applied magnetic field, $F_{dip} = 2\pi\left(\vec{M}\cdot\vec{e}_z\right)^2$ is the demagnetizing energy associated to the film geometry and $F_u = -\frac{K_u}{M_s^2}\left(\vec{M}\cdot\vec{u}\right)^2$ is the energy associated to an *ad hoc* uniaxial magnetic anisotropy along $\vec{u}$. Figure 4.1.2 shows the above defined vectors and the used angular notations. In agreement with our experimental results discussed below we have taken $\vec{u}$ along x for simplification. In this condition, the frequency dependence of the uniform mode is given by:

$$f = \frac{\gamma}{2\pi}\sqrt{\left(H\cos(\varphi_M-\varphi_H) + H_u\cos 2\varphi_M\right)\left(H\cos(\varphi_M-\varphi_H) + H_u\cos^2\varphi_M + 4\pi M_s\right)} \tag{4.1.3}$$

The expression of the resonance field is deduced by replacing H by H_{res} and by writing it as function of f and the other parameters. An explicit expression [2] can be deduced if we consider that $\varphi_M \sim \varphi_H$ which means that the magnetization is always aligned along the applied magnetic field. This is particularly true in the angular dependence experiments. In this conditions, we can write:

$$H_{res} = \sqrt{\left(2\pi M_s + H_u\sin^2\varphi_H\right)^2 + \left(\frac{2\pi f}{\gamma}\right)^2} - 2\pi M_s - H_u\left(\frac{1}{2} + \frac{3}{2}\cos 2\varphi_H\right) \tag{4.1.4}$$

The full lines in figures 4.1.1-a) and 4.1.1-b) correspond to fits of the experimental data using the parameter of table 4.1. We observe that the anisotropy field is maximum

1. This anisotropy field H_u is not a real field vector. However, in the FMR community, it is usual to define anisotropy fields from the anisotropy coefficients.

2. All the fits presented in this research project have been performed by using the full formulation with no assumption in φ_M and φ_H. However, we write H_{res} by considering that $\varphi_M \sim \varphi_H$ to have an explicit expression.

for Ni which possesses the minimum saturation magnetization. The deduced saturation magnetization values correspond to the ones generally reported for similar materials deposited on conventional substrate (rigid ones). We have thus a confirmation of the "good" magnetic properties of our films deposited on polymer substrate.

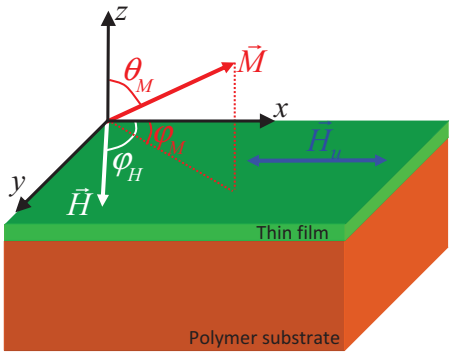

Figure 4.1.2 – Sketch of the coordinate system used in this section. In the experiments presented here, the magnetic field is applied in the (xy) plane. Note that H_u is aligned along $\vec{e}_x$ for simplicity.

Sample	Co_2FeAl	$Co_{40}Fe_{40}B_{20}$	Ni
H_u(Oe)	30	60	310
M_s (emu.cm^{-3})	820	1040	480
γ ($\times 10^7$)	1.835	1.948	1.885

Table 4.1 – Values of the uniaxial anisotropy field (H_u), the saturation magnetization (M_s) and the gyromagnetic ratio (γ) extracted thanks to the experimental data fits.

4.2 Determination of the magnetostriction coefficients

In this section, we present the methodology combining FMR and DIC in order to simultaneously measure the voltage-induced strains and the magnetic resonance response in our thin films. We will see that this methodology is powerful to estimate the magnetostriction coefficient of ferromagnetic thin films deposited onto polymer substrates. In addition, it should be noted that this technique can be also applied to artificial magnetoelectric heterostructures (such as a magnetic film on a piezoelectric substrate) and allows the determination of the effective magnetoelectric coefficient of the whole heterostructures in addition to the piezoelectric coefficients related to the in-plane voltage-induced strains. Finally, this methodology can be applied only to system for which the strains are well transmitted at the different interfaces.

4.2.1 Piezoelectric actuation of the magnetic specimens

We have glued the different films onto a commercially available piezoelectric actuator (see Chapter 2). This actuator will allow us to apply some in-plane strains to the different

films and thus to probe their magnetic response. Note that in this section, the films have been glued such as the easy axis coincides with the long axis of the actuator. We have already shown in Chapter 2 that the transmission of the deformation between the actuator and the film/substrate system is near 100%. Typical FMR spectra are presented in figures 4.2.2-a), Figure 4.2.2-b) and 4.2.2-c) corresponding to different specimens: Ni, Co_2FeAl and $Co_{40}Fe_{40}B_{20}$ respectively. Those spectra have been performed at 0 V and +100 V under similar conditions: driving frequency of 8 GHz and applied magnetic field perpendicular to the actuator (*i. e.* along y axis). We now define the resonance field shift as: $\delta H_{res}(V) = H_{res}(0) - H_{res}(V)$. One can note that this field shift is negative in the case of CFA and CoFeB material while it is positive in the case of Ni material. This is due to the respective sign of the magnetostriction coefficients λ of the different materials. Indeed, if we consider that the films are isotropic in a magnetoelastic point of view and are submitted to a nearly uniaxial stress σ_{xx}, the magnetoelastic energy can roughly be written as:

$$F_{me} = -\frac{3}{2}\lambda(\alpha_x^2 - \frac{1}{3})\sigma_{xx}$$

where α_x is the direction cosine of the magnetization. Thus, an effective magnetoelastic field, defined as $\vec{H}_{me} = -\vec{\nabla}_{\vec{M}} F_{me}$ can be introduced. For positive λ and σ_{xx} values, this field is aligned along x direction, which leads to an easy axis that will increase the resonance field (negative shift) of the uniform mode (because $\varphi_H = \pi/2$) as experimentally observed for CFA and CFB material. A first conclusion concerning the sign of the magnetostriction can be thus done without any modeling of the data: we found that $\lambda^{Ni} < 0$ and $\lambda^{CFA,CFB} > 0$.

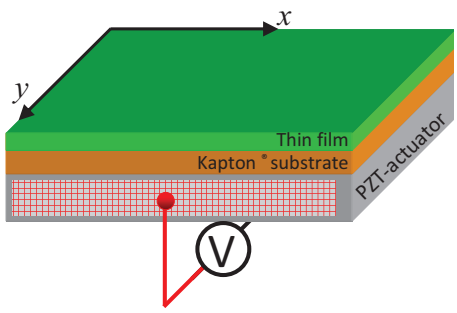

Figure 4.2.1 – Sketch showing the film/substrate glued onto the piezoelectric actuator.

In order to quantitatively determine the magnetostriction coefficients of the films, we have performed DIC and FMR experiments under similar conditions. The measurements have been performed by varying the external voltage from 0 V to 100 V and back to 0 V for the Ni and CFB films and from 0 V to 200 V for the CFA film. The FMR measurements have been performed with a magnetic field applied along y. Figures 4.2.3-a), 4.2.3-b) and 4.2.3-c) present the deduced δH_{res} as function of the applied voltage. We clearly see that δH_{res} is positive in the case of the Ni film and negative for the CFA and CFB films confirming the first observation previously made. Non linear variations of δH_{res} as function of the applied voltage are also found. These variations are similar to the ones found for σ_{xx} and σ_{yy} as function of the applied voltage. We will see in a next section that δH_{res}-variations become linear if we plot them as function of σ_{xx} or σ_{yy} (or $2\sigma_{xx} - \sigma_{yy}$). Thus, we can conclude that this effect is not magnetic or magnetoelastic

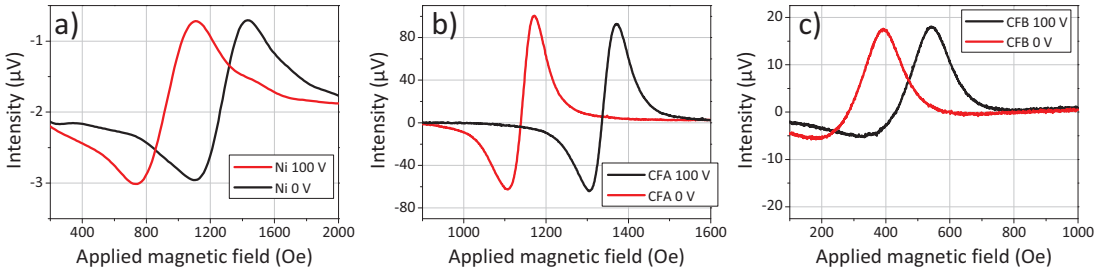

Figure 4.2.2 – Experimental spectra recorded at 8 GHz for an in-plane magnetic field at 90 degree with respect to the main positive strain axis of the actuator (along y-axis) and along the easy axis of the magnetization. A negative shift of the FMR spectra is observed in Ni film while positive shifts are noticed for CFA and CFB films.

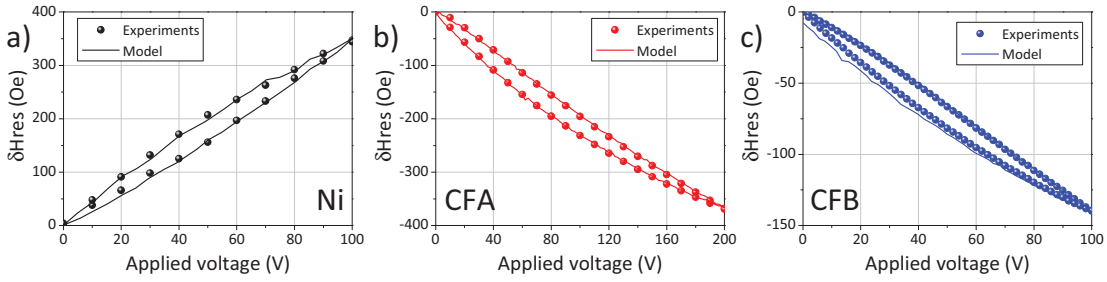

Figure 4.2.3 – a, b) Resonance field shift δH_{res} as function of the applied voltage (between 0 and 200 V for the CFA film). Symbols represent experimental data while solid lines refer to fit obtained from the model described in the text.

but simply due to the specific behavior of the piezoelectric actuator. We note that δH_{res} is important for the Ni film, it reaches a value around 350 Oe at 100 V while it is around 250 Oe for CFA and 150 Oe CFB at 100 V.

4.2.2 Modeling of the resonance field shift

The modeling of the resonance field needs to add the magnetoelastic contribution F_{me} to the energy F defined in equation 4.1.2. We consider that the magnetostriction coefficient λ is isotropic at the macroscopic scale. If we consider that our films are only submitted to in-plane stresses ($\sigma_{zz} = 0$), the magnetoelastic energy can be written as:

$$F_{me} = \frac{3}{2}\lambda((\alpha_x^2 - \frac{1}{3})\sigma_{xx} + (\alpha_y^2 - \frac{1}{3})\sigma_{yy}) \tag{4.2.1}$$

σ_{xx} and σ_{yy} being the in-plane principal stress tensor components while α_x and α_y are the direction cosines of the magnetization. The relation between the stress tensor components (σ_{xx}, σ_{yy}) and the measured strains ($\varepsilon_{xx}(V)$, $\varepsilon_{yy}(V)$) is given by the Hooke's law (see Chapter 2). Like the magnetoelastic properties, the elastic ones are expected to

present isotropic behaviors, the Hooke's law is thus given by:

$$\sigma_{xx} = \left(\frac{Y_f}{1+\nu_f}\right)\left(\frac{1}{1-\nu_f}\varepsilon_{xx}(V) + \frac{\nu_f}{1-\nu_f}\varepsilon_{yy}(V)\right)$$
$$\sigma_{yy} = \left(\frac{Y_f}{1+\nu_f}\right)\left(\frac{1}{1-\nu_f}\varepsilon_{yy}(V) + \frac{\nu_f}{1-\nu_f}\varepsilon_{xx}(V)\right) \quad (4.2.2)$$

Where Y_f and ν_f are the Young's modulus and the Poisson's ratio of the films. The correspondence between strains and voltage are given by the DIC measurements. In these conditions, the resonance field is derived from equation 4.1.1:

$$H_{res}(\varphi_M \simeq \varphi_H) = \sqrt{\left(2\pi M_s\right)^2 + \left(\frac{2\pi f}{\gamma}\right)^2 + H_1 H_2} - 2\pi M_s - \frac{3\lambda}{M_s}(\sigma_{xx} - \sigma_{yy}) \quad (4.2.3)$$

where:

$$H_1 = \frac{3\lambda}{M_s}(\sigma_{xx}\sin^2\varphi_M + \sigma_{yy}\cos^2\varphi_M) \quad (4.2.4)$$
$$H_2 = 4\pi M_s + \frac{3\lambda}{M_s}(\sigma_{xx}\sin^2\varphi_M + \sigma_{yy}\cos^2\varphi_M) \quad (4.2.5)$$

In this formalism, the main unknown is the magnetostriction coefficient λ since Y_f and ν_f can be either estimated from single-crystal elastic coefficients or measured by Brillouin light scattering (BLS). Indeed, CFA and Ni single-crystal elastic coefficients can be found in the literature[20, 21](see table 4.2). Hence, being given the random distribution of the crystallites inside the Ni and CFA films, we can simply use homogenization methods presented in chapters 1 and 2 to estimate the Young's modulus and the Poisson's ratio. Concerning CFB material, even if its amorphous structure confers to the film a full isotropic behavior (both local and macroscopic scales), their coefficients are unknown. However, we will see in chapter 6 that Brillouin light scattering (BLS) can be astutely employed to measure the phonon dispersion which directly depends on those parameters. For all the materials, Y_f and ν_f are presented in table 4.2. We have also calculated the corresponding Zener anisotropy index A for CFA and Ni film from the elastic coefficients ($A = 2C_{44}/(C_{11} - C_{12})$).

The full lines in figures 4.2.3 corresponds to the best fit using equation 4.2.3, the only fitted parameter is λ. As a conclusion, we have shown in this section that the magnetostrictive coefficient can be measured with accuracy.

4.3 Magnetoelastic effect: equivalent stresses concept

In chapters 2 and 3, we have presented two types of methods allowing the study of the magneto-mechanical properties of ferromagnetic thin films: i) bending and ii) piezoactuation. One way to compare the resultant effects from the different types of solicitations is to introduce the multi-axiality of the stress state into the classical uniaxial models through the definition of a fictive uniaxial stress: the equivalent stress that would change the magnetic behavior in a similar manner as the multi-axial one. Several attempts are available in the literature [13, 14], where the most general definition of the equivalent

Sample	Co_2FeAl	$Co_{40}Fe_{40}B_{20}$	Ni
Y_f (GPa)	243	160	200
ν_f	0.27	0.30	0.30
$\lambda(\times 10^{-6})$	14	23	-26
C_{11}(GPa)	253	—	253
C_{12}(GPa)	165	—	152
C_{44} (GPa)	153	—	124
A	3.48	—	2.46

Table 4.2 – Values of the films Young's modulus (Y_f), Poisson's ratio (ν_f), magnetostriction coefficient (λ) and of the elastic coefficients (C_{11}, C_{12} and C_{44}). The Zener anisotropy index (A) is also indicated.

uniaxial stress has been given in 2010 by Daniel and Hubert [15, 16]. In this section, we will present in-depth study of the magnetoelastic properties of the CFA thin film submitted to strainS induced by piezoelectric actuation or by bending tests (uniaxial). After a comparison of results (study of the anisotropy field and determining the magnetostriction coefficients) for these tests under applied magnetic field, we will show how the definition of the equivalent uniaxial stress allows plotting the whole data on a single graph.

4.3.1 Multi-axial stress and resulting anisotropy field

In our system, these in-plane stresses are applied either by a piezoelectric medium or by a curved support. Being given the absence of texture in our films, the magnetostrictive and elastic properties of the films are considered as isotropic at the macroscopic scale. With these assumptions, the magnetostriction coefficient, the Young's modulus and the Poisson's ratio of the thin film are scalars parameters, as previously discussed. Moreover, in order to dissociate the effect of the residual uniaxial anisotropy (H_u) from the anisotropy coming from the magnetoelastic effect, we will neglect the energy F_u. Thus, the magnetic energy of the thin film can be written as:

$$F = F_{zee} + F_{dip} + F_{me} \tag{4.3.1}$$

Where the last term is the magnetoelastic energy F_{me} which can be expressed for a general stress state as follows:

$$F_{me} = -\lambda \left[\frac{3}{2} {}^t\vec{\alpha}\sigma\vec{\alpha} - \frac{1}{2} tr(\sigma) \right] \tag{4.3.2}$$

where $\overrightarrow{\alpha} = (\cos\varphi_M \sin\theta_M, \sin\varphi_M \sin\theta_M, \cos\theta_M)$ is the unit vector along the magnetization (see figure 4.3.1 and σ is the stress tensor that has the following general form in the absence of shear stress:

$$\sigma = \begin{pmatrix} \sigma_{xx} & 0 & 0 \\ 0 & \sigma_{yy} & 0 \\ 0 & 0 & \sigma_{zz} \end{pmatrix} \tag{4.3.3}$$

Where σ_{xx}, σ_{yy} and σ_{zz} are the orthogonal normal stresses.

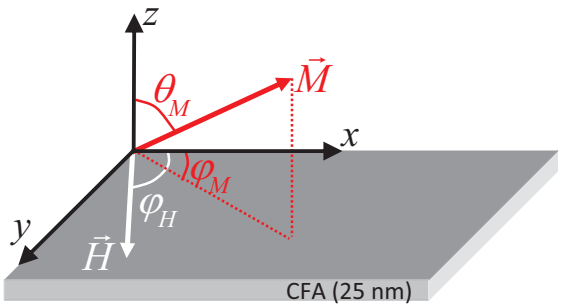

Figure 4.3.1 – Schematic illustration showing the angles and the coordinate system used in the text.

Then, the magnetoelastic energy is:

$$F_{me} = -\frac{3}{2}\lambda\left(\sigma_{xx}\cos^2\varphi_M \sin^2\theta_M + \sigma_{yy}\sin^2\varphi_M \sin^2\theta_M + \sigma_{zz}\cos^2\theta_M\right) + \frac{\lambda}{2}\left(\sigma_{xx}+\sigma_{yy}+\sigma_{zz}\right) \tag{4.3.4}$$

The situation could be simplified if an in-plane magnetic field is applied (sufficiently strong to ensure a uniform magnetization distribution), the equilibrium polar angle is thus $\theta_M = \frac{\pi}{2}$ because of the large effective demagnetizing field associated with the planar film geometry, the magnetoelastic energy can finally be expressed as:

$$F_{me}\left(\theta_M = \frac{\pi}{2}\right) = -\frac{\lambda}{4}[\sigma_{xx}(1+3\cos 2\varphi_M) + \sigma_{yy}(1-3\cos 2\varphi_M) - 2\sigma_{zz}] \tag{4.3.5}$$

An equivalent stress σ_{eq}^{DH} has been introduced by Daniel and Hubert [15, 16] and comes from the general expression of the magnetoelastic energy in the isotropic case, e.g. from equation 4.3.2. It defines a fictive uniaxial stress that would change the magnetic behavior in a similar manner than a multi-axial one. This is particularly useful to compare results obtained from different kind of solicitations as it will be shown in this section. Indeed, from equation 4.3.2, being given that the magnetoelastic energy for a given uniaxial stress $\sigma_{uniaxial}$ is $F_{me} = -\lambda\sigma_{uniaxial}$, the equivalent stress introduced by Daniel and Hubert can be expressed as follows :

$$\sigma_{eq}^{DH} = \frac{3}{2}{}^t\vec{\alpha}\sigma\vec{\alpha} - \frac{1}{2}tr(\sigma) \tag{4.3.6}$$

If we consider the specific "in-plane" case ($\theta_M = \frac{\pi}{2}$), this equivalent stress becomes:

$$\sigma_{eq//}^{DH} = \frac{1}{4}[\sigma_{xx}(1+3\cos 2\varphi_M) + \sigma_{yy}(1-3\cos 2\varphi_M) - 2\sigma_{zz}]$$

Moreover, from the energy (equation 4.3.4), it is convenient to introduce an "effective" magnetoelastic anisotropy field, which magnitude can be defined as follows for an in-plane magnetization:

$$H_{me}(\varphi_M) = \frac{1}{M_s}\frac{\partial^2 F_{me}}{\partial \varphi_M^2}\bigg|_{\theta_M=\frac{\pi}{2}} = \frac{3\lambda\left(\sigma_{xx}-\sigma_{yy}\right)\cos 2\varphi_M}{M_s} \tag{4.3.7}$$

If one consider the x axis ($\varphi_M = 0$), we find the following expression for the magnetoelastic anisotropy field:

$$H_{me} = \frac{3\lambda\left(\sigma_{xx}-\sigma_{yy}\right)}{M_s} \tag{4.3.8}$$

This expression is independent of σ_{zz} and is directly related to the difference of stresses along the principal axes x and y. We will discuss about the links with the equivalent stress $\sigma_{eq//}^{DH}$ in the next subsection.

4.3.2 Resonance field as function of equivalent uniaxial stress

The resonance field of the uniform precession mode evaluated at the equilibrium is obtained from the Smith-Beljers, the expression is given by equation 4.1.1 where the different derivatives are evaluated at the equilibrium direction of the magnetization. An explicit expression can be derived for an in-plane applied magnetic field ($\theta_M = \frac{\pi}{2}$):

$$\begin{aligned}\left(\frac{2\pi f}{\gamma}\right)^2 = &\Big[4\pi M_s + H_{res}\cos(\varphi_M-\varphi_H) + \frac{3\lambda}{M_s}\left(\sigma_{xx}\cos^2\varphi_M + \sigma_{yy}\sin^2\varphi_M - \sigma_{zz}\right)\Big] \\ &\times\Big[H_{res}\cos(\varphi_M-\varphi_H) + \frac{3\lambda}{M_s}((\sigma_{xx}-\sigma_{yy})\cos 2\varphi_M\Big]\end{aligned} \tag{4.3.9}$$

The angles φ_H and φ_M are defined in figure 4.3.1. We can derive the resonance field expression from equation 4.3.9 by considering that the magnetic field is strong enough to saturate the magnetization ($\varphi_M \simeq \varphi_H$):

$$H_{res}(\varphi_M \simeq \varphi_H) = \sqrt{\left(2\pi M_s\right)^2 + \left(\frac{2\pi f}{\gamma}\right)^2 + H_a H_b} - 2\pi M_s - \frac{3\lambda}{M_s}\sigma_{eq//}^{DH} \tag{4.3.10}$$

Where:

$$H_a = \frac{3\lambda}{2M_s}(\sigma_{xx}\sin^2\varphi_M + \sigma_{yy}\cos^2\varphi_M - \sigma_{zz}) \tag{4.3.11}$$

and

$$H_b = 4\pi M_s + \frac{3\lambda}{2M_s}(\sigma_{xx}\sin^2\varphi_M + \sigma_{yy}\cos^2\varphi_M - \sigma_{zz}) \tag{4.3.12}$$

Being given that the order of the stress-induced anisotropy is twofold, it is convenient to determine the magnitude of the magnetoelastic anisotropy field by measuring the total amplitude of the angular dependance of the resonance field H_{res}. Here, we can introduce

the FMR-magnetoelastic field determined by the following expression, and that can be measured from in-plane angular dependence of the resonance field:

$$2H_{me}^{FMR} = \Big[H_{res}(\varphi_M = \frac{\pi}{2}) - H_{res}(\varphi_M = 0)\Big] \tag{4.3.13}$$

This can be expressed as follows:

$$\begin{aligned} 2H_{me}^{FMR} &= \frac{9\lambda}{2M_s}(\sigma_{xx} - \sigma_{yy}) \\ &+\Big[(2\pi M_s)^2 + \big(\frac{2\pi f}{\gamma}\big)^2 + 6\pi\lambda(\sigma_{xx} - \sigma_{zz}) + \big(\frac{3\lambda(\sigma_{xx} - \sigma_{zz})}{2M_s}\big)^2\Big]^{1/2} \\ &-\Big[(2\pi M_s)^2 + \big(\frac{2\pi f}{\gamma}\big)^2 + 6\pi\lambda(\sigma_{yy} - \sigma_{zz}) + \big(\frac{3\lambda(\sigma_{yy} - \sigma_{zz})}{2M_s}\big)^2\Big]^{1/2} \end{aligned} \tag{4.3.14}$$

In each square-root of 4.3.14, with standard experimental conditions ($(\sigma_{xx} - \sigma_{zz})$ and $(\sigma_{yy} - \sigma_{zz})$ of the order of 100 MPa, $\lambda \sim 20 \times 10^{-6}$, $M \sim 1000$ emu.cm^{-3}, f of a few GHz, and $\frac{\gamma}{2\pi} = 0.003$ GHz.Oe^{-1}) the third term is about 3 orders of magnitude higher than the fourth one and 5 lower than the two first ones. Thus, concerning the two terms related to magnetoelastic contribution, the fourth term can be neglected as compared to the third one. Finally, the usual way is to apply the following first-order Taylor expansion inside each square-root (with $i = x, y$):

$$\begin{aligned} &\big[(2\pi M_s)^2 + \left(\frac{2\pi f}{\gamma}\right)^2 + 6\pi\lambda(\sigma_{ii} - \sigma_{zz})\big]^{1/2} \approx \\ &\left((2\pi M_s)^2 + \left(\frac{2\pi f}{\gamma}\right)^2\right)^{\frac{1}{2}} \left(1 + \frac{1}{2}\frac{6\pi\lambda(\sigma_{ii} - \sigma_{zz})}{(2\pi M_s)^2 + \big(\frac{2\pi f}{\gamma}\big)^2}\right) \end{aligned} \tag{4.3.15}$$

Therefore, the magnetoelastic anisotropy can be expressed as:

$$H_{me}^{FMR} \approx \frac{9\lambda}{4M_s}(\sigma_{xx} - \sigma_{yy}) + \frac{3\pi\lambda(\sigma_{xx} - \sigma_{yy})}{2\sqrt{(2\pi M_s)^2 + \left(\frac{2\pi f}{\gamma}\right)^2}} \tag{4.3.16}$$

One can note that H_{me}^{FMR} depends on the frequency, this variation being shown on figure 4.3.2 $\big(H_{me}^{FMR}(f)\big) / \big(H_{me}^{FMR}(f = 0)\big)$ as function of f. At $f = 0$ GHz, the FMR resonance field is equal to the static one H_{me} already determined in equation 4.3.8. It decreases with frequency, according to equation 4.3.16, and gradually approaches $\frac{3}{4}H_{me}$.

In our standard range (0-10GHz), one can see that H_{me}^{FMR} is very close to H_{me} so that the the expression can be rewritten as:

$$H_{me}^{FMR}(f) \approx H_{me} \approx \frac{3\lambda}{M_s}(\sigma_{xx} - \sigma_{yy}) \tag{4.3.17}$$

Concerning the stress dependance, this expression suggests that in the case of an in-plane magnetized thin film, any given multi-axial stress state leads to an in-plane

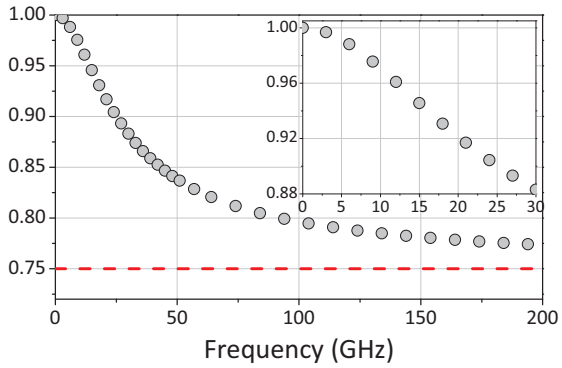

Figure 4.3.2 – Frequency dependence of H_{me}^{FMR} for a large frequency range. The inset shows this frequency dependence for usual FMR frequency range (0-30 GHz).

anisotropy field proportional to the term $(\sigma_{xx} - \sigma_{yy})$. This is consistent with the equivalent stress $\sigma_{eq}^{SR} = (\sigma_{xx} - \sigma_{yy})$ proposed by Schneider and Richardson [17] to describe the evolution of the anisotropy field with an applied biaxial stress state. Moreover, one can note that σ_{eq}^{SR} is simply equal to:

$$\sigma_{eq}^{SR} = -\frac{2}{3}\left[\sigma_{eq//}^{DH}\left(\varphi_M = \frac{\pi}{2}\right) - \sigma_{eq//}^{DH}\left(\varphi_M = 0\right)\right] \tag{4.3.18}$$

Hence, the whole experimental data resulting from various kind of solicitations (uniaxial or multi-axial) can be plotted in a common graph with the term $(\sigma_{xx} - \sigma_{yy})$ defining the abscissa axis and H_{me} the ordinate ones, as we will see in the following subsection.

4.3.3 Confrontation of piezo-actuation and bending strains effects

We propose now to apply the equivalent stress concept to the thin CFA film (25 nm). This last one is stressed both by piezo-actuation (non equibiaxial) or by bending tests (uniaxial) and measured with our broadband ferromagnetic resonance technique. In order to obtain of maximum of points in the $(\sigma_{xx}, \sigma_{yy})$ map, we have performed piezoactuation in the range -200 V, +200 V. Figures 4.3.3-a) and 4.3.3-b) show the deformations measured by digital image correlation (DIC) as function of the applied voltage. When applying a voltage, the mean values of ε_{xx} and ε_{yy} vary with $\frac{\varepsilon_{yy}}{\varepsilon_{xx}} \sim -0.625$, while the in-plane shear strain ε_{xy} remains unchanged (not shown here). In figure 4.3.3-a), the curve corresponds to a simple electric loading-unloading (0 V - 200 V - 0 V) ; the non-linearity characterized by a "loop" shape is due to the specific piezoelectric behavior of the actuator, which is reversible. In figure 4.3.3-b), we show a symmetrical cyclic loading path, *.i.e.* an unloading from +200 V to −200 V and a subsequent loading from −200 V to +200 V. We observe the so-called "butterfly" behavior that is due to polarization switching at about −60 V during unloading and +60 V during loading [11]. Data shown in 4.3.3-a) and 4.3.3-b) are reported in a ε_{yy} *versus* ε_{xx} graph (figure 4.3.3-c). The "loop" (full blue circle symbols) and "butterfly" (open blue symbols) data are well superimposed despite of the polarization switching occurring in the case of cyclic path. From the values of ε_{xx} and ε_{yy}, it is straightforward to calculate the planar stresses σ_{xx}

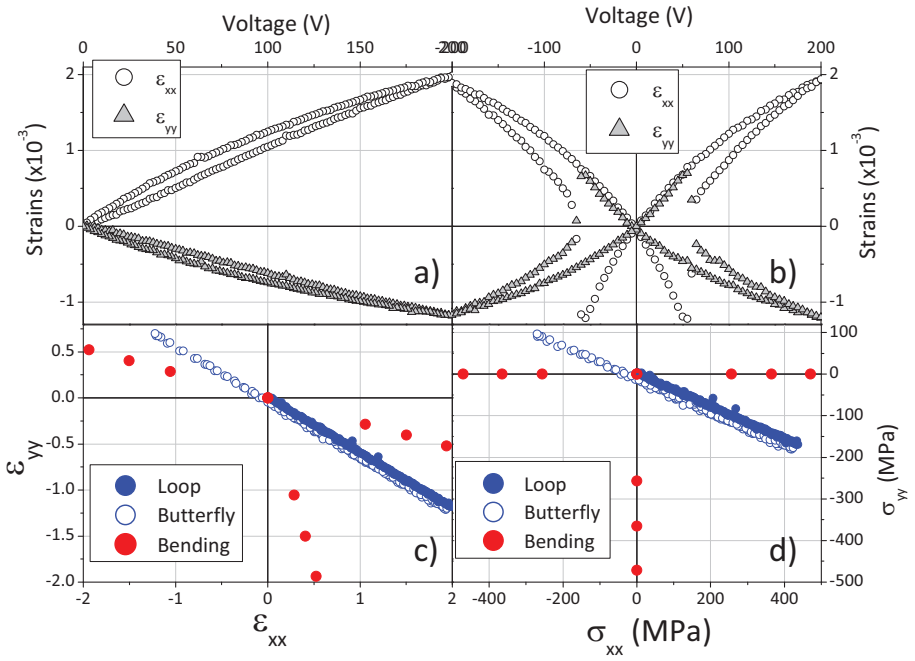

Figure 4.3.3 – a) ε_{xx} and ε_{yy} as function of voltage applied to piezoelectric actuator, measured by DIC, for a simple electric loading-unloading. b) ε_{xx} and ε_{yy} as function of voltage applied to piezoelectric actuator, measured by DIC, for a symmetric electric loading path. c) ε_{yy} as a function of ε_{xx} for piezoelectric actuation ("loop" and "butterfly" behavior) and unaxial bending. d) σ_{yy} as a function of σ_{xx} for piezoelectric actuation ("loop" and "butterfly" behavior) and unaxial bending.

and σ_{yy} using isotropic Hooke's law, knowing the elastic constants of the polycrystalline film, being given the isotropic crystallographic texture. The mean values of σ_{xx} and σ_{yy} vary with $\frac{\sigma_{yy}}{\sigma_{xx}} \sim -0.394$ as shown in 4.3.3-d).

In addition, we have also shown in figures 4.3.3-c) and 4.3.3-d) attainable strains and stresses respectively by bending the samples. These experiments have been performed by gluing the films onto small pieces of aluminum blocks of circular cross-section of known radii R: 32.2 mm, 41.6 mm, 59.2 mm and infinite (flat surface). More details about the *in situ* can be found in chapters 2 and 3. Here, the curvature stress can be applied either along x axis or y axis. When the bending is applied along x axis, the strains are given by:

$$\varepsilon_{xx} = \frac{(t_f + t_s)}{2R}\Gamma \tag{4.3.19}$$

and

$$\varepsilon_{yy} = -\nu_f \frac{(t_f + t_s)}{2R}\Gamma \tag{4.3.20}$$

Where Γ is the correction introduced in chapter 2. However, being given the mechanical parameters of the film and the substrate and their respective thicknesses, we found that Γ is close to unity. In the case of bending along y axis, the expressions of ε_{xx} and ε_{yy} are found by substituting one for the other. In any case, the uniaxial stress along x axis or y

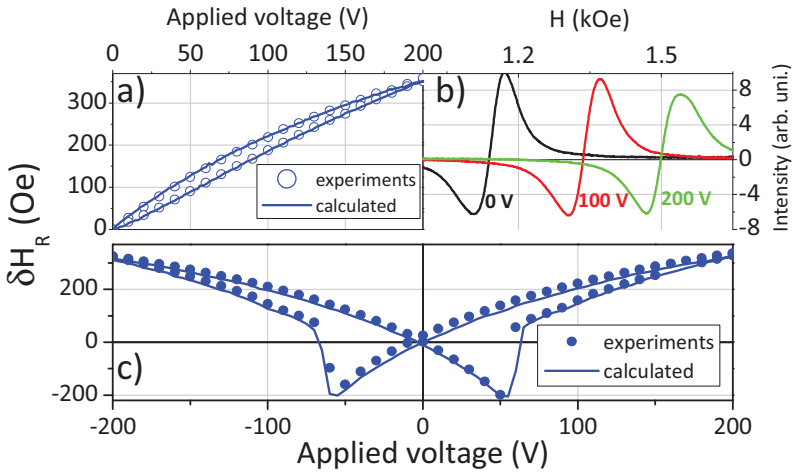

Figure 4.3.4 – a) . Resonance field shift, defined as $\delta H_R = H_R(V) - H_R(V = 0)$, as function of applied voltage to the piezoelectric actuator in the case of backward and forward voltage loops (0 ; 200 V). Circled points refer to experimental data while solid line is the fit using the model described in the text. b) Typical FMR spectra for different applied voltages (0 V, 100 V and 200 V). The positive shift is coherent with a positive magnetostriction coefficient of CFA. c) Resonance field shift as function of applied voltage to the piezoelectric actuator in the case of cyclic electric loading (-200 V ; 200 V).

axis is found by using Hooke's law. In our conditions, the above-mentioned radii values correspond respectively to the following values of applied stresses : 0.47 GPa, 0.37 GPa, 0.26 GPa, 0 GPa. Moreover, the stress in the thin film is compressive if the film is in contact of the bent-block and tensile if the substrate is the bent block. We have thus studied three opposite stress states and the zero stress state (unbent sample).

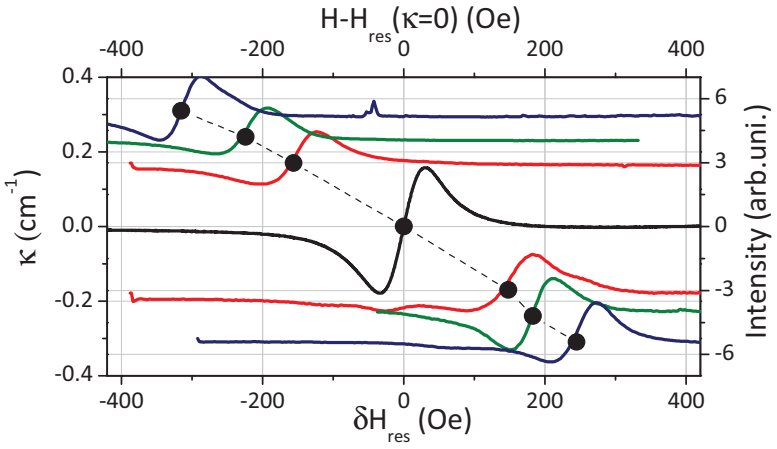

Figure 4.3.5 – FMR spectra for bended samples with different curvatures $\kappa = \pm 1/R$ (here along x axis). Circle symbols show the curvature κ as function of $\delta H_R = H_R(\kappa) - H_R(\kappa = 0)$.

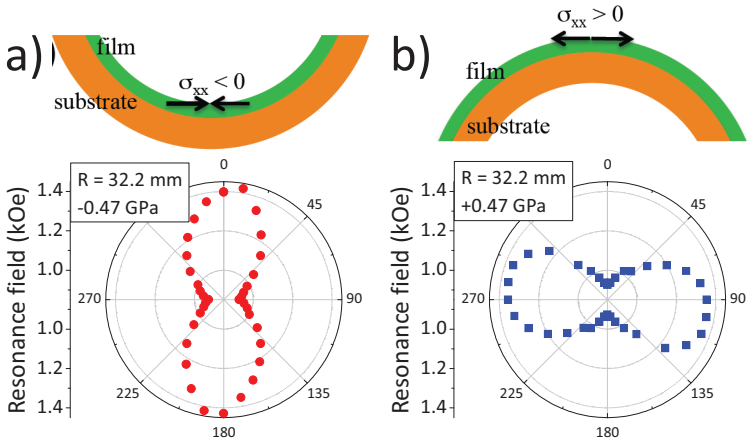

Figure 4.3.6 – Azimuthal angle dependance of the resonance field in polar representation with the corresponding bending effect on the stress state (either negative a) or positive b)) for CFA film placed on aluminum block with 32.2 mm radius.

Now, we study the influence of voltage-induced strains on the magnetization uniform precession mode by *in situ* MS-FMR measurements, before comparing these tests with bending ones. For this, the MS-FMR spectra have been reordered at 10 GHz microwave frequency and the magnetic static applied field has been varied. A backward and forward voltage loops (0-200 V) with steps of 10 V were applied to the PZT-actuator. The relative evolution of resonance field, defined as $\delta H_R = H_R(V) - H_R(V = 0)$, is shown in figure 4.3.3-a). Figure 4.3.3-b) shows the typical MS-FMR spectra at different applied voltages (0 V, 100 V and 200 V). Obviously, the resonance field evolution versus the voltage depends on the sign of the magnetostriction coefficient at saturation as we observe it in the precedent section. Since the magnetoelastic field H_{me} is a voltage-dependent

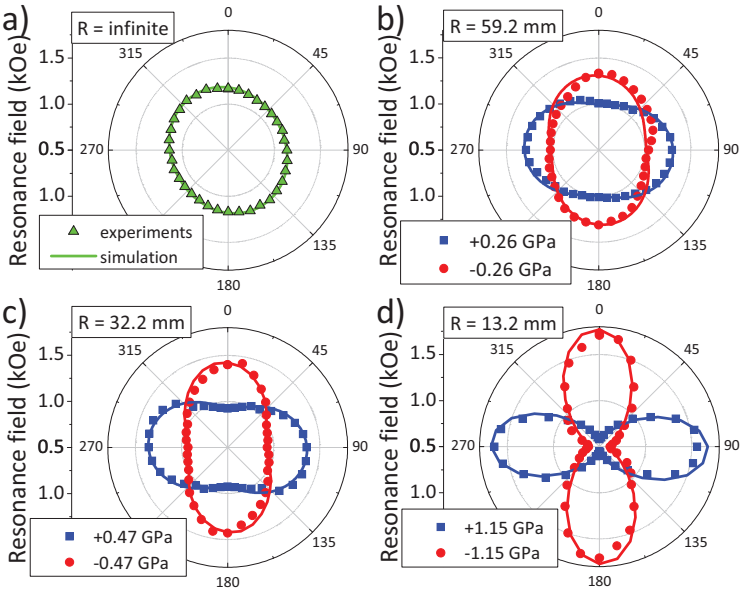

Figure 4.3.7 – Angular dependance of the resonance field (at 10 GHz) for $R = \infty$ (a), $R = 59.2$ mm (b), $R = 32.2$ mm (c), $R = 13.2$ mm (d). In figures (b), (c) and (d) are shown the opposite stress states.

field, expressing the resonance field as function of the applied voltage is equivalent to expressing the resonance field versus H_{me}. Thus, as shown on figure 4.3.3-a), a non-linear and loop-like behavior of the evolution of the uniform precession mode resonance field with the applied voltage and the magnetoelastic field is observed. As ferromagnetic films follow perfectly the elastic strains of the piezoelectric actuator, the hysteretic behavior of the resonance field shift can be explained by the intrinsic behavior (ferroelectric) of the actuator. Moreover, this is confirmed by measurements made for the cyclic electric loading (figure 4.3.3-c) for which we find a resonance field following perfectly the "butterfly" behavior found in 4.3.3-c). All these experimental observations are well described by the theoretical model already described in the precedent sub-section.

Considering samples submitted to mechanical bending, figure 4.3.5 shows the evolution of MS-FMR spectra for different curvatures $\kappa = \pm 1/R$ along x-axis. The shift of the resonance field is related to the resulting applied uniaxial stresses given in figure 4.3.3-d). Obviously, this behavior is similar when the experiments are made along y -axis. In order to easily extract the strain-induced magnetoelastic anisotropy field, we have performed FMR angular dependence measurements. It is interesting to see in figures 4.3.6-a) and 4.3.6-b) that the sign change for σ_{xx} in the thin film induces a switching of the uniaxial anisotropy as revealed by the angular dependencies of the resonance field for the two opposite stress values $\sigma_{xx} = -0.47$ GPa and $\sigma_{xx} = +0.47$ GPa. In our configuration, the x axis corresponds to $\varphi_H = 90°$ and $270°$ and y axis corresponds to $\varphi_H = 0°$ and $180°$. Note that the apparent slight misalignment between the easy axis and the x axis in figure 4.3.6-a) ($\sigma_{xx} < 0$) and the y axis in figure 4.3.6-b) ($\sigma_{xx} < 0$) respectively is due to the initial residual uniaxial anisotropy field H_u in the thin film (before applied bending) at about $30°$ from the x axis. Fig.4.3.7-a) shows the angular dependance of

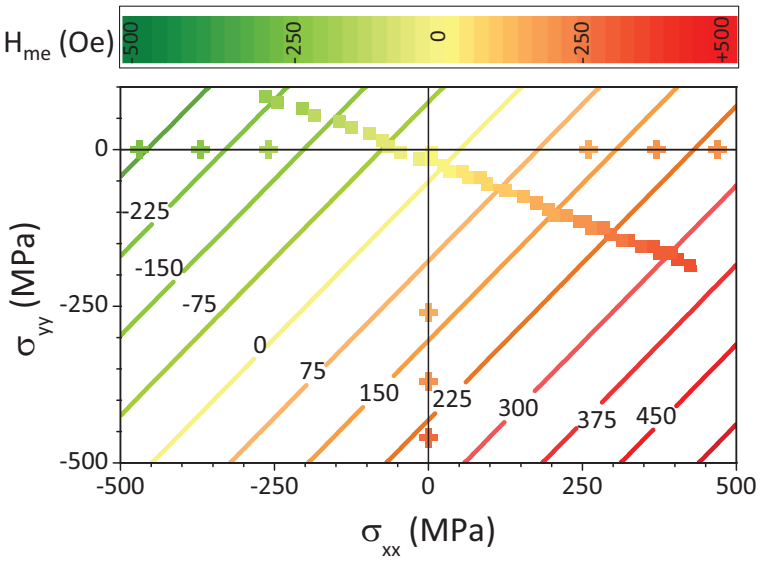

Figure 4.3.8 – Theoretical (iso-anisotropy field lines) and experimental (square symbols for piezoactuation experiments, circle symbols for bending experiments) anisotropy field H_{me} map in the principal stress space $(\sigma_{xx}, \sigma_{yy})$.

the resonance field for unbent sample. We will see in the next chapter that this initial uniaxial anisotropy, is due to a slight initial unavoidable curvature of the sample after deposition when using polymer substrates. In figures 4.3.7-b), 4.3.7-c) and 4.3.7-d) are shown the angular dependencies of the resonance fields for all the applied stress states. The continuous lines are fits to the experimental data by using equation 4.3.10 with $\sigma_{yy} = \sigma_{zz} = 0$ and $\sigma_{xx} = Y_f \varepsilon_{xx}$. Note that we have used the parameters determined in the precedent section ($M_s = 820$ emu.cm^{-3}, $\gamma = 1.835 \times 10^7$ s^{-1}.Oe^{-1}, $H_u = 30$ Oe and $\lambda = 14 \times 10^{-6}$). One can note the good agreement between the experimental data and the calculated lines.

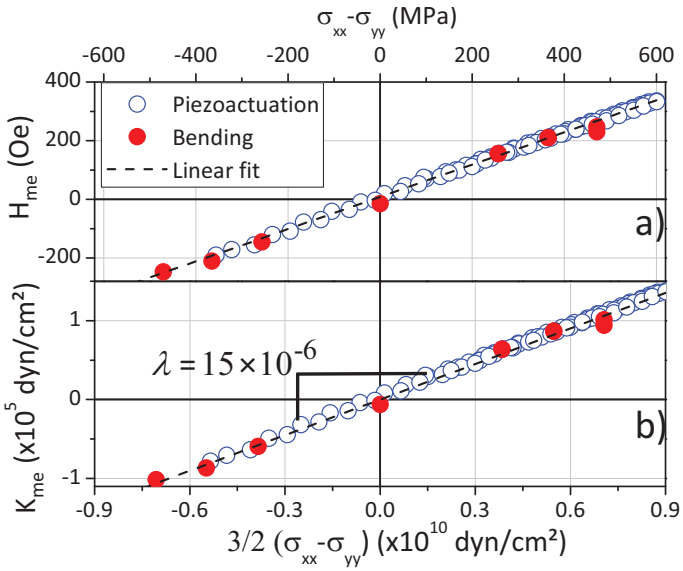

Figure 4.3.9 – (a) Anisotropy field H_u and (b) Anisotropy constant K_u, as function of $\frac{3}{2}(\sigma_{xx} - \sigma_{yy})$. Knowing the magnetization at saturation, the slope of the linear regression gives directly the magnetostriction coefficient λ.

We can now compare the results coming from the piezoactuation and the ones coming from bending by plotting the extracted magnetoelastic field H_{me} as function of σ_{xx} and σ_{yy}. In figure 4.3.8, we show the theoretical (iso-anisotropy field lines) and the experimental (square symbols for piezoactuation experiments, circle symbols for bending experiments) anisotropy field H_{me} mapped in the principal stress space $(\sigma_{xx}, \sigma_{yy})$. The analytical expression of $H_{me} = \left[H_{res}(\varphi_M = \frac{\pi}{2}) - H_{res}(\varphi_M = 0)\right]/2$ is given in equation 4.3.16 and is directly proportional to $(\sigma_{xx} - \sigma_{yy})$; that is why the iso-anisotropy field are perfectly linear. Here, the only fitting parameter is the magnetostriction coefficient $\lambda_{CFA} = 14 \times 10^{-6}$ (by fitting the overall data). The accordance between model and experimental data seems very good and show that an equibiaxial stress state with opposite components favorizes the in-plane anisotropy.

However, from this map, it is not straightforward to compare the two kinds of experiments since one is biaxial and the other uniaxial. That is why we have plotted H_{me} as function of $\sigma_{eq}^{DH}(\varphi_M = 0) - \sigma_{eq}^{DH}\left(\varphi_M = \frac{\pi}{2}\right) = \frac{3}{2}(\sigma_{xx} - \sigma_{yy})$ in order to underscore the efficiency of the equivalent stress concept, especially here for thin films submitted to different solicitations (figure 4.3.9-a). We show here that the overall data (blue circle symbols for piezoactuation and red square symbols for bending) follows the same line on this graph. Obviously, a simple linear fit given by equation 4.3.14 allows determining the magnetostriction coefficient $\lambda_{CFA} = 15 \times 10^{-6}$, in a very simple and direct manner, as shown on figure 4.3.9 that presents $K_{me} = \frac{H_{me} M_s}{2}$ as function of $\frac{3}{2}(\sigma_{xx} - \sigma_{yy})$. Finally, it should be noted that this good agreement between the voltage and the bending induced strain is another indication of the perfect strain transmission from the piezoelectric actuator to the CFA film.

Bibliography

[1] G. Lin, D. Makarov, M. Melzer, W. Si, C. Yan and O. G. Schmidt, Lab on a Chip **14**, 4050 (2014). (Cited on page 68.)

[2] C. Barraud, C. Deranlot, P. Seneor, R. Mattana, B. Dlubak, S. Fusil, K. Bouzehouane, D. Deneuve, F. Petroff and A. Fert, Applied Physics Letters **96**, 072502 (2010). (Cited on page 68.)

[3] A. Bedoya-Pinto, M. Donolato, M. Gobbi, L. E. Hueso, and P. Vavassori, Applied Physics Letters **104**, 062412 (2014). (Cited on page 68.)

[4] M. Melzer, M. Kaltenbrunner, D. Makarov, D. Karnaushenko, D. Karnaushenko, T. Sekitani, T. Someya and O. G. Schmidt, Nature Communications **6**, 6080 (2015). (Cited on page 68.)

[5] E. Fernez, G. V Kurlyandskaya, A. GarcArribas and A. V. Svalov, Nanoscale Research Letters **7**, 230 (2012). (Cited on page 68.)

[6] K. Agra, T.J.A. Mori, L. S. Dorneles, V. M. Escobar, U.C. Silva, C. Chesman, F. Bohn and M. A. Corr Journal of Magnetism and Magnetic Materials **355**, 136 (2014). (Cited on page 68.)

[7] B. Li, M. N. Kavaldzhiev and J. Kosel, Journal of Magnetism and Magnetic Materials **378**, 499 (2015). (Cited on page 68.)

[8] A. Alfadhel, B. Li, A. Zaher, O. Yassine and J. Kosel, Lab on a Chip, **14**, 4362 (2014). (Cited on page 68.)

[9] R. Streubel, D. J. Thurmer, D. Makarov, F. Kronast, T. Kosub, V. Kravchuk, D. D. Sheka, Y. Gaididei, R. Schr and O. G. Schmidt, Nano Letters **12**, 3961 (2012). (Cited on page 68.)

[10] Y. Yu, Q. Zhan, J. Wei, J. Wang, G. Dai, Z. Zuo, X. Zhang, Y. Liu, H. Yang, Y. Zhang, S. Xie, B. Wang and R.-W. Li, Applied Physics Letters **106**, 162405 (2015). (Cited on page 68.)

[11]) F. Zighem, A. El Bahoui, J. Moulin, D. Faurie, M. Belmeguenai, S. Mercone and H. Haddadi, Journal of Applied Physics **116**, 123903 (2014). (Cited on pages 91 and 94.)

[12] Z. Suo, E. Y. Ma, H. Gleskova, and S. Wagner, Applied Physics Letters **74**, 1177 (1999). (Cited on pages 44, 45 and 90.)

[13] C. S. Schneider and J. M. Richardson, Journal of Applied Physics **53**, 8136 (1982). (Cited on page 74.)

[14] J. Pearson, P. T. Squire, M. G. Maylin, and J. G. Gore, IEEE Transaction on Magnetism **36**, 3251 (2000). (Cited on page 74.)

[15] L. Daniel, O. Hubert, Journal of Applied Physics **105**, 07A313 (2009). (Cited on pages 75 and 76.)

[16] L. Daniel, O. Hubert, IEEE Transactions on magnetics **46**, 3089 (2010). (Cited on pages 75 and 76.)

[17] C. S. Schneider and J. M. Richardson, Journal of Applied Physics **53**, 8136 (1982). (Cited on page 79.)

[18] R. D. Mc Michael, M. D. Stiles, P. J. Chen and W. F. Egelhoff, Jr, Physical Review B **58**, 9605 (1998). (Not cited.)

[19] D. Faurie, P. Djemia, E. Le Bourhis, P.-O. Renault, Y. Roussign. M. Chf, R. Brenner, O. Castelnau, G. Patriarche, Ph. Goudeau, Acta Materiala **58**, 4998 (2010). (Not cited.)

[20] M. S. Gabor, T. Petrisor, Jr., C. Tiusan, M. Hehn, and T. Petrisor, Physical Review B **84**, 134413 (2011). (Cited on page 74.)

[21] J. R. Neighbours, F. W. Bratten, and Charles S. Smith, Journal of Applied Physics **23**, 389 (1952).

(Cited on page 74.)

5 Residual anisotropy in magnetic films deposited on polymer substrate

In the introduction of this thesis, we saw that thin films deposited on polymer substrates represent a new generation of functional systems. These lasts allow applications involving non-planar geometries, especially in confined spaces [1, 2, 3]. Moreover, low cost and light weight polymers are additional benefits and significant for the industrialization of these systems. However, the functional properties of the thin films must be well controlled in this type of substrate that has specificities (flexibility, roughness, anisotropy behavior related to the extrusion process). Regarding magnetic films, several applications such as flexible tunnel junctions [4], magneto-impedance [5, 6] or magnetoresistance sensors are under development [1, 7].. However, it is crucial to understand in depth the magnetic behavior of such specific systems. Magnetic films deposited on polymer substrates have specific properties. Indeed, many groups have reported residual planar magnetic anisotropy without deciding on their possible origin (magnetoelastic effect related to intrinsic or extrinsic stresses, anisotropic geometry related to the extrusion direction, roughness, interfacial effect, etc.) [8, 9, 10, 11, 12, 13]. In the precedent chapter, we have interpreted this phenomenon, without providing an absolute objective evidence (single confrontation of the anisotropy of the same material deposited on silicon and Kapton®). To give an answer, we have studied a $Ni_{80}Fe_{20}$ film known to have a very low magnetostriction and compared to the results on much more magnetostrictive films.

5.1 Preambles

In this chapter, we argue that the residual anisotropy of the studied films is due to magnetoelastic effects. This residual magnetoelastic effect must obviously be due to residual stresses in the thin film. It is known that thin film growth on a substrate generates residual stresses even if no epitaxy occurs. Indeed, even at room temperature, many phenomena are sources of stresses in amorphous films (atomic peening due to ion bombardment) and polycrystalline films (atomic peening, coalescence at grain boundaries, grain growth, ...). Hence, theses stresses will modify the "film-substrate" system geometry. In the following, Y_f and Y_s refer to film and substrate Young's modulus, respectively, t_f and t_s refer to film and substrate thickness, respectively. We will separate two cases: i) rigid substrate and ii) flexible substrate.

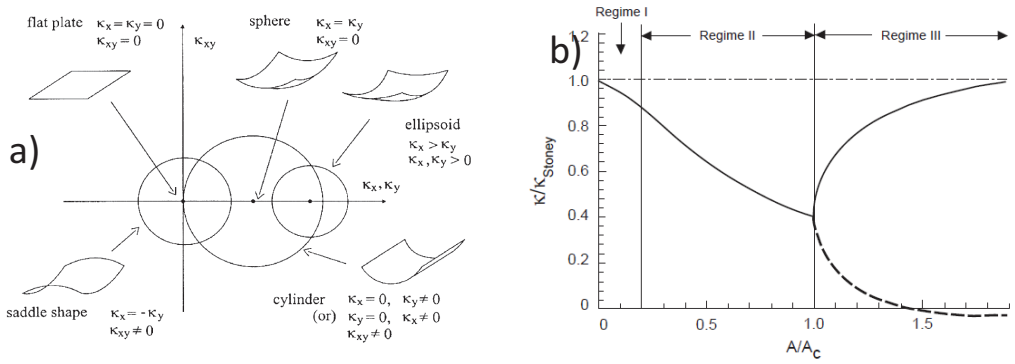

Figure 5.1.1 – a) Mohr's circle representation of the shapes of curved surfaces describing all the possible configurations for flexible system. κ_x, κ_y are the principal curvatures while κ_{xy} is the twist one (negligible for a thin film on a substrate). b) Numerical predictions of principal curvatures at wafer center normalized by the small deformation spherical curvature (κ_{Stoney}) as a function of the ratio A/A_c. The parameter A depends on the film and substrate thickness and elastic coefficients; Behind the critical parameter A_c, $\kappa_x \neq \kappa_y$ and thus cylindrical shape occurs (bifurcation phenomenon).

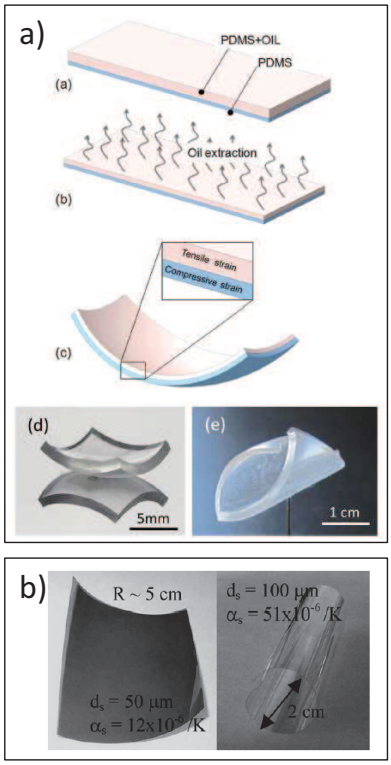

Figure 5.1.2 – a) Facile fabrication scheme of PDMS bilayers with a spontaneous curvature and the films acquiring spherical and cylindrical deformation, depending on the film sample size. The spherically deformed sample is photographed on a reflecting substrate. b) PECVD silicon nitride film deposited on two different plastic substrates. The substrate thickness and the coefficient of the thermal expansion are shown for each substrate. The film is deposited on the top and the structures roll into cylinder.

• Rigid Substrate ($Y_f t_f \ll Y_s t_s$):

In the case of rigid substrate (like silicon), the substrate dominates and the film complies with it. The stress in the substrate is small, and the film/substrate system curves only slightly, even when the film is highly stressed. The stress is equibiaxial and the structure forms a spherical cap with a radius of curvature R given by the so-called Stoney's equation linking R to the residual stresses [14].

• Flexible Substrate ($Y_f t_f$ approaches the magnitude of $Y_s t_s$):

Such case gives rise to complicated mechanical situations as shown in figure 5.1.1-a). A curvature bifurcation phenomenon (see figure 5.1.1-b)) arises from the fact that the substrate cannot deform into a spherical cap shape without stretching or compressing portions of its mid-plane when deformation is not small. The substrate is very stiff in extension compared to bending due to its plate-like shape. Therefore, this coupling between curvature and stretching tend to stiffen the system response. Furthermore, in contrast to spherical bending, ellipsoidal (or cylindrical) bending can occur with only very limited mid-plane extension, which suggests that the system may begin a transition from axially symmetric deformation, as the only possible equilibrium shape, toward cylindrical bending deformation as an alternate shape, which is energetically favorable.

Thus, the structure rolls into a cylinder instead of forming a spherical cap as it can be shown in figure 5.1.2-a) for PDMS bilayer showing strain gradient. Obviously, this phenomenon also occurs for flexible electronics systems [23], as it can be seen in figure 5.1.2-b) . The Stoney formula is no longer valid. The dependence of the bifurcation on the geometrical and mechanical parameters of the bilayer square plates was investigated theoretically by Salamon & Masters in 1995 [15] and Finot & Suresh in 1996 [16]. A few experimental works, consisting in measuring radii of curvature have been made and are in good correlation with models [17, 18, 19]. To conclude on this point, a cylindrical curvature in "thin metal/polymer" system usually exists even if the residual stresses are expected to be equibiaxial and if the sample shape is a square or a circle. Moreover, the manipulation of these flexible systems during their physical characterization may induce undesirable stresses, especially when they are flattened on specimen holders.

5.2 Residual magnetic anisotropy

We have first measured the residual anisotropy in several thin films of different materials, namely: $Ni_{80}Fe_{20}$, Ni, $Co_{40}Fe_{40}B_{20}$, Co_2FeAl and $Fe_{73.5}Cu_1Nb_3Si_{15.5}B_7$ (Finemet ®). All these films were prepared by rf sputtering; it should be noted here that the films thickness are not always similar (20, 200, 20, 20 and 530 nm, respectively). However, we will see that there is no influence of such a variation in our discussions. For measuring the in-plane anisotropy, the ferromagnetic resonance was used in absence of applied stresses. In-plane angular dependencies of the uniform precession mode of different films were measured. The angular dependencies for the different films are presented in figure 5.2.1 (where the driving frequency is fixed to 8 GHz). A twofold (uniaxial) anisotropy if clearly put into evidence in all the studied films. A first observation concerns the microstructure of the films; indeed, here all the studied films present either an amorphous behavior (Finemet and CFB) or are polycrystalline with no strong preferred orientations, thus no macroscopic magnetocrystalline effect is expected. As a conclusion, we can exclude the magnetocrystalline anisotropy for the origin of this anisotropy. Another proof of this

Sample	$Ni_{80}Fe_{20}$	Co_2FeAl	$Co_{40}Fe_{40}B_{20}$	Finemet®[22]	Ni
H_u(Oe)	7	30	60	75	310
M_s (emu.cm^{-3})	756	720	1040	965	480
γ ($\times 10^7$)	1.835	1.835	1.948	1.885	1.885

Table 5.1 – Values of the uniaxial anisotropy field (H_u), the saturation magnetization (M_s) and the gyromagnetic ratio (γ) extracted thanks to the experimental data fits (equation 5.2.1).

statement is that the Ni and the CFA are known to have cubic lattices, the attached magnetocrystalline anisotropy is a fourfold one, which is not the case here.

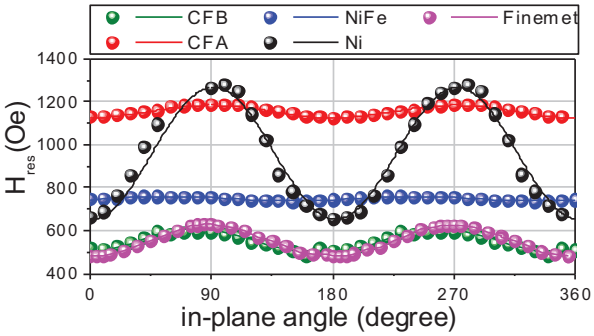

Figure 5.2.1 – Angular dependance of the resonance field as a function of in-plane angle for the different films: $Co_{40}Fe_{40}B_{20}$ (green), $Ni_{80}Fe_{20}$ (blue), Finemet ® (magenta), Co_2FeAl (red) and Ni (black).

We can extract quantitative values of this uniaxial anisotropy field H_u by fitting the experimental dependencies. For this purpose, we can use the Smith and Beljer formulation by introducing an uniaxial anisotropy field H_u. In this condition, the deduced value of the resonance field can be written as:

$$H_{res} = \sqrt{(2\pi M_s + H_u \sin^2\varphi_H)^2 + (2\pi f/\gamma)^2} - 2\pi M_s - H_u(\frac{1}{2} + \frac{3}{2}\cos 2\varphi_H) \quad (5.2.1)$$

It should be noted that this formulation is simplified, indeed we consider here that the magnetization is always aligned along the applied magnetic field. The full lines in figure 5.2.1 correspond to fits of the experimental data using the parameter of table 5.2. We observe that the anisotropy field is maximum for Ni which possesses the minimum saturation magnetization. However, no more correlations could be done between M_s and H_u.

In addition, we have verified that this anisotropy disappears when similar films are deposited onto rigid substrates (Silicon, Young's modulus of 200 GPa). Figures 5.2.2-a) and 5.2.2-b) show the resonance field variation as function of φ_H for Ni and Finemet® films deposited on two Kapton® and Silicon substrate. A uniaxial anisotropy field is still present; however its magnitude is ten times smaller than the one measured on Kapton: H_u for the Ni and Finemet® on Kapton® are respectively $H_u = 300$ Oe and $H_u = 40$

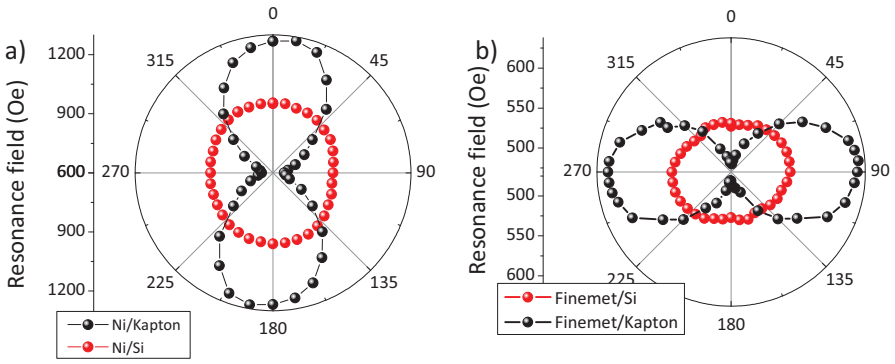

Figure 5.2.2 – Angular dependance of the resonance field as a function of in-plane angle for: (a) 200 nm Ni thin film on Kapton® and Si; (b) Finemet® on Kapton® and Si.

Oe while similar films on Si give $H_u = 7$ Oe and 30 Oe. Finally, we experienced that the easy axis does not necessarily match with the polymer extrusion direction (recognizable by its surface grooves). In this context, the correspondence between magneto-mechanical behavior and residual anisotropy seems to be the only identifiable source of this effect and is certainly due to the high flexibility of the substrate.

5.3 Origin of the residual magnetic anisotropy

To elucidate the origin of residual anisotropy in magnetic films on polymer substrate, magnetostriction coefficients (λ) of the different films are determined thanks to the methods described in chapter 4. For clarity, only results on $Ni_{80}Fe_{20}$ and $Co_{40}Fe_{40}B_{20}$ films will be presented in detail. Figure 5.3.1-a) shows the evolution of the resonance field shift, defined as the resonance field measured in absence of voltage and the one measured at a specific voltage, as function of the applied voltage for two materials (i.e. $Ni_{80}Fe_{20}$ and $Co_{40}Fe_{40}B_{20}$). The curves correspond to a simple electrical loading-unloading (0 V - 100 V - 0 V) during which FMR spectra have been recorded every 2V (at frequency equal to 10 GHz); we have already discussed that the non-linearity of the curve is due to the specific piezoelectric behavior of the actuator that is reversible and well captured in both resonance (figure 5.3.1-a)) and strain (figure 5.3.1-b)) measurements.

It is clear that the $Co_{40}Fe_{40}B_{20}$ resonance field is changing much more than that of $Ni_{80}Fe_{20}$ between 0 V and 100 V (140 Oe instead of 6 Oe). Using a common scale on the y-axis for both curves make difficult to observe the non-linearity of the $Ni_{80}Fe_{20}$ curve. However, this is more apparent with an appropriate scale despite the small variations, which exacerbates the quality of our measurements in terms of resolution (see inset in figure 5.3.1-a)).

The observed behavior can be modeled by measuring the voltage/in-plane strains correspondence. For this purpose, we have measured the in-plane strains variations as function of the applied voltage with similar experimental conditions (electrical loading-unloading (0 V - 100 V - 0 V) by step of 2 V). These variations are presented on figure 5.3.1-b). After extracting the experimental values of the voltage/in-plane strains correspondence, it is possible to model the observed behavior. This correspondence is presented in the

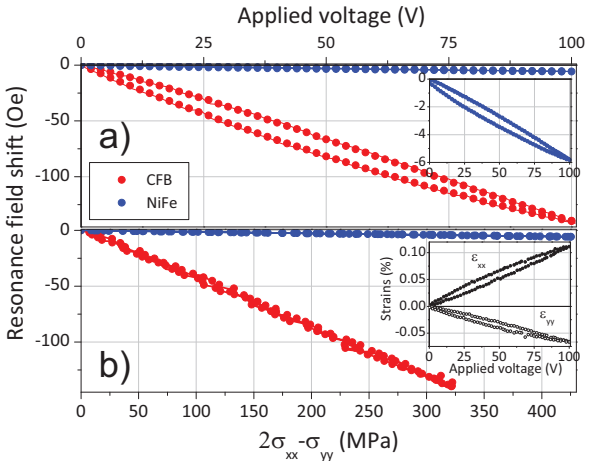

Figure 5.3.1 – Resonance field shift variations as a function of the applied voltage (a) and the applied stress (b) for $Co_{40}Fe_{40}B_{20}$ (red symbols) and $Ni_{80}Fe_{20}$ (blue symbols). Solid lines refer to the adjusting models for the two samples. The insert in (a) is a zoom of the $Ni_{80}Fe_{20}$ curve, while the one in (b) is the measured variation of the in-plane strains (ε_{xx} and ε_{yy} at the top surface of the films) as a function of the applied voltage.

caption of figure 5.3.1-b). Note that the observed nonlinearities in figure 5.3.1-a) can be avoided if the resonance field shift H_{res}, defined as $\delta H_{res} = H_{res}(0) - H_{res}(V)$, is plotted as a function of $2\sigma_{xx} - \sigma_{yy}$ (calculated by using equations 5.3.2 and 5.3.3), as discussed in chapter 4. The analysis can be relatively simple if the resonance field is larger than the magnetoelastic anisotropy field. Indeed, in this condition, the magnetization direction is almost aligned along the applied magnetic field. The resonance field, when the saturation field is applied along the x axis (corresponding to the sample longitudinal elongation direction) is thus given by [21]:

$$H_{res} = \sqrt{\left(2\pi M_s + \frac{3\lambda}{2M_s}\sigma_{yy}\right)^2 + \left(\frac{2\pi f}{\gamma}\right)^2} - 2\pi M_s - \frac{3\lambda}{2M_s}\left(2\sigma_{xx} - \sigma_{yy}\right) \quad (5.3.1)$$

The last term corresponds to the resonance field variation with the voltage-induced magnetoelastic anisotropy field because $\frac{3\lambda}{2M_s}\sigma_{yy} \ll 2\pi M_s$. As previously mentioned, the resonance field shift is approximately equal to $\delta H_{res} \simeq -\frac{3\lambda}{2M_s}\left(2\sigma_{xx} - \sigma_{yy}\right)$, that is confirmed by the linear variation of δH_{res} as a function of $2\sigma_{xx} - \sigma_{yy}$ (see figure 5.3.1-b)). The relation between the in-plane stresses (σ_{xx}, σ_{yy}) and strains (ε_{xx}, ε_{yy}) measured by DIC (see figure 5.3.1-b)) is given by the isotropic Hook's law where Y_f is the film Young's modulus and ν_f is the film Poisson's ratio:

$$\sigma_{xx} = \left(\frac{Y}{1+\nu}\right)\left(\frac{1}{1-\nu}\varepsilon_{xx} + \frac{\nu}{1-\nu}\varepsilon_{yy}\right) \quad (5.3.2)$$

$$\sigma_{yy} = \left(\frac{Y}{1+\nu}\right)\left(\frac{1}{1-\nu}\varepsilon_{yy} + \frac{\nu}{1-\nu}\varepsilon_{xx}\right) \quad (5.3.3)$$

Sample	$Ni_{80}Fe_{20}$	Co_2FeAl	$Co_{40}Fe_{40}B_{20}$	Finemet®[22]	Ni	FeGa[8]
Y_f (GPa)	180[25]	243	160[24]	145	200	60
H_u(Oe)	7	30	60	75	310	455
$\lambda(\times 10^{-6})$	0.75	14	23	23	-30	100
R(cm)	10.9	33	7.1	7.2	6.7	21,3

Table 5.2 – Anisotropy field (H_u), magnetostriction coefficient (λ) and estimated radius of curvature (R) for different magnetic films studied in the framework of this this thesis.

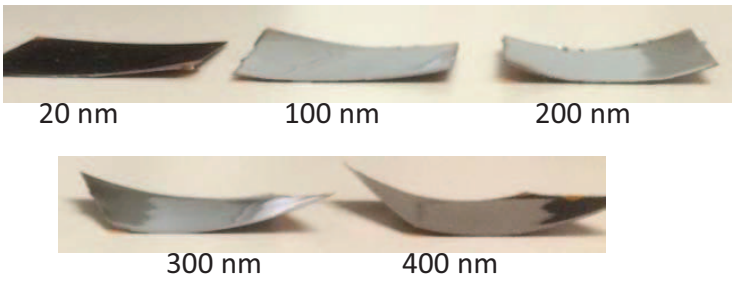

Figure 5.3.2 – Photography of five $Ni_{80}Fe_{20}$ samples with several thicknesses (20nm, 100nm, 200nm, 300nm and 400nm) showing increasing cylindrical bending with thickness.

Finally, being given the physical parameters presented in tables 5.2, λ is the only undetermined parameter. It can be determined by fitting the experimental data thanks to equation 5.3.1. The values of λ for $Co_{40}Fe_{40}B_{20}$ and $Ni_{80}Fe_{20}$ are presented in table 5.2 and are respectively equal to 23×10^6 and 0.75×10^6. The values for all the other films are also summarized in this table in addition to measurements made by Dai *et al.* [8] for FeGa films which possesses high λ. A correlation between the magnetostriction coefficient λ, the residual anisotropy H_u and the saturation magnetization M_s clearly appears. By considering that H_u is due to an unavoidable bending of the system, we can now calculate the corresponding radii of curvature of the different films. For this purpose, we will use H_u values presented in table 5.2. Indeed, in these conditions, H_u could be written as a magnetoelastic field:

$$H_u = \frac{3\lambda\sigma_u}{M_s} \tag{5.3.4}$$

where σ_u is the stress induced by the uniaxial curvature of the system, it can be viewed as a residual stress. It can be related to a radius of curvature by the following formula:

$$\sigma_u = Y\left(\frac{t_f + t_s}{2R}\right)\frac{1 + 2\frac{t_f}{t_s} + \frac{Y_f}{Y_s}\frac{t_f^2}{t_s^2}}{\left(1 + \frac{t_f}{t_s}\right)\left(1 + \frac{Y_f}{Y_s}\frac{t_f}{t_s}\right)} \tag{5.3.5}$$

with R the sample radius of curvature, t_f and t_s are respectively the films and substrate thicknesses and Y_s the substrate Young's modulus. Therefore, the radius of curvature

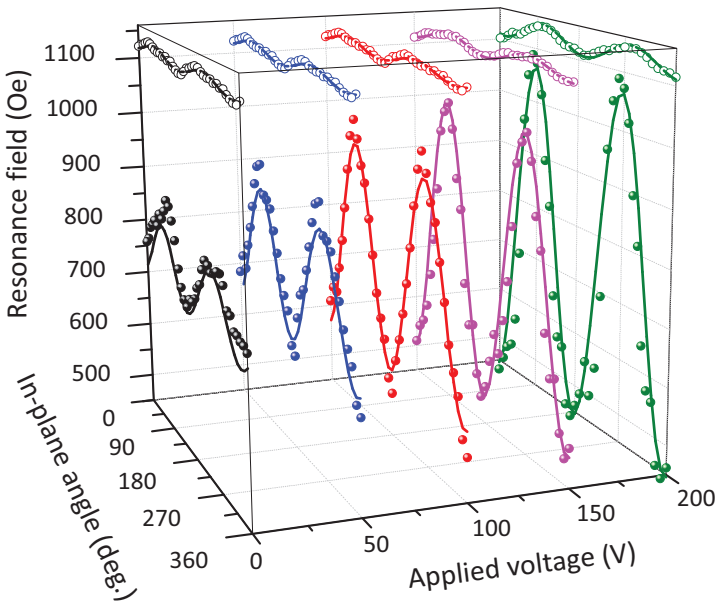

Figure 5.3.3 – Angular and voltage dependences of the resonance field (at $f = 10$ GHz) for the $Ni_{80}Fe_{20}$(open circles) and $Co_{40}Fe_{40}B_{20}$ (spheres) thin films. The solid lines are fit to the experimental data.

can be expressed as follows :

$$R = \frac{3\lambda Y_f}{M_s}\left(\frac{t_f + t_s}{2H_u}\right)\frac{1 + 2\frac{t_f}{t_s} + \frac{Y_f}{E_s}\frac{t_f^2}{t_s^2}}{\left(1 + \frac{t_f}{t_s}\right)\left(1 + \frac{Y_f}{E_s}\frac{t_f}{t_s}\right)} \tag{5.3.6}$$

Table 5.2 shows the radii obtained for all the studied films. It can be seen that the high discrepancies in terms of H_u (from 7 to 455 Oe) or λ (from 0.75×10^{-6} to 100×10^{-6}) leads to radii of the same order (from 7.1 to 33). Moreover, these R values are high when compared to the usual lateral sample dimensions (few millimeters) so that this effect cannot be easily observed. In order to directly estimate this effect, we have deposited films of different thickness ranging from 20 nm to 400 nm on large substrates (3×3 cm^3), i.e. larger than those described before (0.5×0.5 cm^2). A cylindrical curvature has been systematically observed for the whole samples (see figure 5.3.2). Using an optical camera in front of the curvature axis, we have measured the samples deflection and then the radius of curvature R. We find that R varies from 8 cm to 2.5 cm with increasing thickness because of the associated increasing elastic energy. Especially, the value estimated for the 20 nm film is fairly similar to those estimated from FMR measurements (6.7 cm).

All the results can be summarized in figure 5.3.3, which shows the in-plane angle and voltage dependencies of the resonance field. One can see that in the case of $Co_{40}Fe_{40}B_{20}$ sample (spheres symbols in figure 5.3.3), a substantial residual anisotropy occurs at zero applied voltage, as already shown in figure 5.2.1. Subsequently, by applying a voltage to the piezoelectric actuator, with σ_{xx} along the residual easy axis, the magnetic uniaxial anisotropy increases from 60 Oe to 330 Oe when applied voltage varies from 0 V to 200 V. In contrast, figure 5.3.3 shows that the $Ni_{80}Fe_{20}$ sample (open circles) does not present

a significant residual anisotropy, and the applied voltage has a very weak influence as a result of a very low magnetostriction (H_u varies from 5 Oe to 20 Oe when applied voltage varies from 0 V to 200 V). The different solid lines of the figure have been calculated using the parameters already discussed (λ, Y, ν, M_s and γ) and by introducing an in-plane angle φ between σ_{xx} and the applied magnetic field, to equation 5.3.7. By considering that the magnetization is always aligned along the applied magnetic field, the angular dependence of the resonance field can be written as:

$$H_{res} = \sqrt{\left(2\pi M_s + \frac{3\lambda}{2M_s}(\sigma_{xx}\sin^2\varphi + \sigma_{yy}\cos^2\varphi)\right)^2 + \left(\frac{2\pi f}{\gamma}\right)^2} - 2\pi M_s - \frac{3\lambda}{4M_s}\Big(\sigma_{xx}(1+3\cos 2\varphi) + \sigma_{yy}(1-3\cos 2\varphi)\Big) \quad (5.3.7)$$

A well agreement between experimental measurements and the calculated angular dependence of the resonance field is found confirming the robustness of our description. In conclusion, we have shown that the residual magnetic anisotropy generally encountered in thin films on flexible substrates is correlated to the magnetostriction coefficient. Indeed, even if it is known that residual stresses in amorphous or polycrystalline films do not induce planar anisotropy, polymer substrates are inevitably slightly curved during deposition and/or magnetic measurements. This phenomenon, although slight, induces an important in-plane anisotropy field if the magnetostriction is significant. Only the permalloy, whose magnetostriction is very small, can eliminates these effects.

Bibliography

[1] LA. Bedoya-Pinto, M. Donolato, M. Gobbi, L. E. Hueso and P. Vavassori, Applied Physics Letters **104**, 062412 (2014). (Cited on page 88.)

[2] D. Karnaushenko , D. Makarov , M. Stber , D.D. Karnaushenko , S. Baunack , and O. G. Schmidt, Advanced Materials **27**, 880 (2014). (Cited on page 88.)

[3] G. Lin, D. Makarov, M. Melzer, W. Si, C. Yanac and O. G. Schmidtab, Lab on a Chip, **14**, 4050 (2014). (Cited on page 88.)

[4] C. Barraud, C. Deranlot, P. Seneor, R. Mattana, B. Dlubak, S. Fusil, K. Bouzehouane, D. Deneuve, F. Petroff and A. Fert, Applied Physics Letters **96**, 072502 (2010) (Cited on page 88.)

[5] B. Li, M.N. Kavaldzhie, J. Kosel, Journal of Magnetism and Magnetic Materials **378**, 499 (2015). (Cited on page 88.)

[6] K. Agra, R.R. Gomes, R.D. DellaPace, L.S. Dorneles, F.Bohn, M.A. Corr Journal of Magnetism and Magnetic Materials **393**, 593 (2015) (Cited on page 88.)

[7] M. Melzer, M. Kaltenbrunner, D. Makarov, D. Karnaushenko, D. Karnaushenko, T. Sekitani, T. Someya, O. G. Schmidt, Nature Communications **6**, 6080 (2015). (Cited on page 88.)

[8] G. Dai, Q. Zhan, Y. Liu, H. Yang, X. Zhang, B. Chen and R.-W. Li, Applied Physics Letters **100**, 122407 (2012) . (Cited on pages 4, 88 and 94.)

[9] H. Kockar, O. Karaagac, H. Kuru, A. Karpuz, M.S. Haciismailoglu, M. Alper, Optoelectronics and advanced Materials **8**, 270 (2014). (Cited on page 88.)

[10] D. D. Lam, F. Bonell, Y. Shiota, S. Miwa, T. Nozaki, E. Tamura, N. Mizuochi, T. Shinjo, Y. Suzuki, and S. Yuasa, AIP Advances **5**, 067132 (2015) (Cited on page 88.)

[11] F.F. Yang, S.S. Yan, M.X. Yu, S.S. Kang, Y.Y. Dai, Y.X. Chen, S.B. Pan, J.L. Zhang, H.L. Bai, D.P. Zhu, S.Z. Qiao, W.W. Pan, G.L. Liu, L.M. Mei, Journal of Alloys and Compounds **558**, 91 (2013) (Cited on page 88.)

[12] X. Zhang, Q. Zhan, G. Dai, Y. Liu, Z. Zuo, H. Yang, B. Chen, R-W. Li, Journal of Applied Physics **113**, 17A901 (2013) (Cited on page 88.)

[13] H. Zuo, S. Ge, Z. Wang, Y. Xiao and D. Yao, Scripta Materialia **62**, 766 (2010) (Cited on page 88.)

[14] G. Gerald Stoney, "The Tension of Metallic Films Deposited by Electrolysis" Proceedings of the Royal Society of London. Series A, Containing Papers of a Mathematical and Physical Character **82**, 172 (1909) (Cited on page 90.)

[15] N. J. Salamon and C. B. Masters, International Journal of Solids and Structures **3,** 473 (1995) (Cited on page 90.)

[16] M. Finot and S. Suresh, Journal of the Mechanics and Physics of Solids **44**, 683 (1996) (Cited on page 90.)

[17] T.-S. Park, S. Suresh, A.J. Rosakis, J. Ryu, Journal of the Mechanics and Physics of Solids **51**, 2191 (2003) (Cited on page 90.)

[18] C. Kim, T.-I. Lee, M. S. Kim,T.-S. Kim, Polymers **7**, 985 (2015) (Cited on page 90.)

[19] A. I. Egunov, J. G. Korvink and V. A. Luchnikov, Soft Matter **16**, 45 (2016) (Cited on page 90.)

[20] R. Bonin, M. L. Schneider, T. J. Silva and J. P. Nibarger, Journal of Applied Physics **98**, 123904 (2005) (Not cited.)

[21] F. Zighem, M. Belmeguenai, D. Faurie, H. Haddadi and J. Moulin, Review of Scientific Instruments **85**, 103905 (2014) (Cited on page 93.)

[22] F. Zighem, A. El Bahoui, J. Moulin, D. Faurie, M. Belmeguenai, S. Mercone and H. Haddadi, Journal of Applied Physics **116**, 123903 (2014) (Cited on pages 91 and 94.)

[23] Z. Suo, E. Y. Ma, H. Gleskova, and S. Wagner, Applied Physics Letters **74**, 1177 (1999). (Cited on pages 44, 45 and 90.)

[24] Z. Tang, B. Wang, H. Yang, X. Xu, Y. Liu, D. Sun, L. Xia, Q. Zhan, B. Chen, M. Tang, Y. Zhou, J. Wang and R.-W. Li, Applied Physics Letters **105**, 103504 (2014) (Cited on page 94.)

[25] H. Pan, V.L. Zhang, K. Di, M.H. Kuok, H.S. Lim, S.C. Ng, N. Singh and A.O. Adeyeye, Nanoscale Research Letters 8, 115 (2013)

(Cited on page 94.)

6 Influence of annealing on the magnetoelastic properties of $Co_{20}Fe_{60}B_{20}$ thin films

Ferromagnetic amorphous alloys (often also referred as metallic glasses) are at the vanguard of the magnetic materials for their soft properties: high magnetic permeability, well defined magnetic anisotropy, small coercivity, good mechanical properties, etc[5]. Amongst the mist of these materials, CoFeB films are highly prized for spintronics applications particularly as electrodes in magnetic tunnel junctions due to its high spin polarization, high TMR ratio, etc. Nevertheless, to improve the functional properties of ferromagnetic amorphous specially the magnetic and magnetoelastic properties heat treatment is undertaken by annealing the specimen[7, 8, 9, 10, 11, 12]. The annealing lead to a modification of structural properties of specimen with a phase transition from amorphous to crystalline or amorphous to nano-crystalline. Subsequently, the elastic (Poisson's ratio ν_f and Young's modulus Y_f), magnetoelastic (magnetic anisotropy H_u, the saturating magnetization M_s, the magnetostriction coefficient λ,...) are affected. Flexible substrates that serve as drop-in replacements for rigid substrates must meet many requirements: surface roughness, thermal and thermomechanical properties. The working temperature of the substrate, for example the glass transition of the polymer (T_g) of a polymer must be compatible with the fabrication process temperature. The most used flexible substrates are organic polymers including polyethylene terephthalate (PET), polyethylene naphthalate (PEN), polyethersulphone (PES), polydimethylsiloxane (PDMS) since they are flexible, lightweight, cost-effective and compatible with the roll-to-roll processing [1, 4]. However, most of the polymers cannot suffer a high-temperature treatment, polyimide (PI) material particularly the one commercialized by $DuPont's^{TM}$ under the name Kapton®, is suitable for fabrication of most of magnetic films and devices because of the near room temperature deposition and low temperature (usually lower than 400°C) post-annealing, its good mechanical strength, higher glass transition temperature, electrochemical stability, and flexibility in polymer materials [2, 3]. In view of these considerations, the CFB samples used in this chapter are annealed during 60 mn in vacuum for annealing temperature up to 375° C.

6.1 As deposited film: elastic, magnetic and magneto-elastic properties

This section is devoted to the "basic" characterization of $Co_{20}Fe_{60}B_{20}$ (CFB) films deposited on Kapton®. However, in addition to the magnetic and magneto-elastic properties, we also directly probed the elastic properties of this film by using Brillouin light scattering (BLS). The films were deposited using a magnetron sputtering system at room

temperature under an argon pressure of 1 m Torr and a rate of 0.1 nm.s^{-1}. We have deposited films with three different thicknesses: 10 nm, 20 nm and 250 nm. It should be noted that the 250 nm-films were initially deposited to measure the elastic coefficients by BLS in order to avoid the substrate effect but have been finally also analyzed by FMR in order to compare the magnetostriction coefficient. X-ray diffraction measurements have been conducted and their analyzes lead to the conclusion that all the films are amorphous.

6.1.1 Elastic properties

The FINANO research group in within which this PhD thesis has been performed is historically known in view of his Brillouin light scattering measurements in thin films. We remind that Brillouin scattering is the inelastic scattering of light by acoustic waves or by spin waves. It is this thus a powerful technique to probe either the propagation of spin waves or acoustic waves. This subsection concerns the acoustic waves propagation with the idea to "directly" measure the elastic coefficients of our films by analyzing the acoustic waves dispersion. The main principle is to illuminate our thin films and to collect the inelastic scattered light. The frequency shift is related to the velocity of the scattering acoustic wave. The propagation direction and frequency of this acoustic wave are determined by the energy conservation. It is thus possible to calculate the acoustic wave velocity and then the associated elastic moduli.

In the specific case of opaque thin films on substrate, one can only probe surface acoustic waves (SAW) such as the Rayleigh wave and the Sezawa ones [14]. The Rayleigh wave is a slight material undulation confined at the top surface of the film. It has an elliptic polarization that lies in the sagittal plane defined by the propagation direction and the surface normal (xOz on figure 6.1.1-b)). On the other hand, the Sezawa ones are standing waves in the film thickness. Since CFB films is amorphous, its elastic properties can be considered as isotropic. Consequently, the frequencies of the surface acoustic waves (SAW) are function of only two elastic coefficients *viz.* Poisson's ratio (ν_f) and Young's modulus (Y_f). The Rayleigh velocity is mainly related to the shear elastic coefficient ($C_{44}^f = G_f$ for isotropic media [15]) while the harmonic Sezawa ones depends both on Y_f and G_f. Obviously, ν_f is directly related to these two last coefficients. However, it should be noted that the probed surface acoustic waves propagates in a depth roughly equal to half of the laser wavelength. Therefore, the measured effective elastic coefficients can be strongly influenced by the substrate for thicknesses inferior to 250 nm. It is thus more complicated to extract the elastic parameters (Y_f and ν_f). This is the reason why we have measured the acoustic waves dispersions in the 250 nm films. Actually, it is well known that elastic constants in solids are size dependent only for very small thicknesses (below a few nanometers). For instance, P. Villain *et al.* [16] have shown by molecular dynamics that the Young's modulus of W layers is equal to the bulk one within 5% for thickness larger than 6 nm; ; it only strongly decreases for thicknesses smaller than 1 nm. We can also cite the work of P.-M. Chassaing *et al.* [17] who shows by low-frequency Raman spectrometry of acoustic phonons that linear elasticity (using bulk elastic constants) is still valid beyond 3 nm (experiment made on wurtzite prismatic zinc oxide nanoparticles of sizes varying from 2.3 to 6.6 nm). Many works confirm that size effects for elasticity occurs only below 10 nm [18, 19]. In this condition, we will

consider that the extracted Y_f and ν_f values are thickness independent.

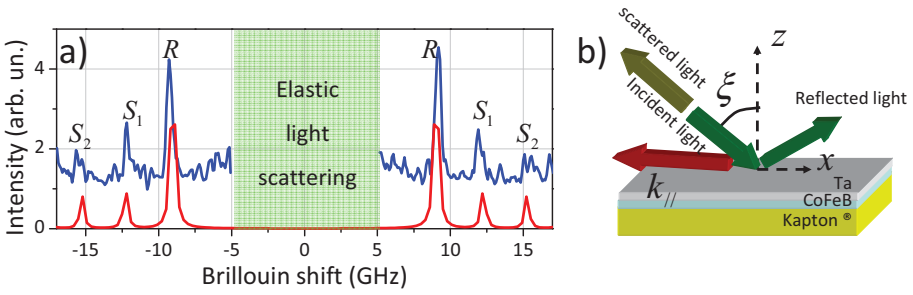

Figure 6.1.1 – Experimental and theoretical Brillouin spectra of a 250 nm thick amorphous CFB thin layer deposited onto Kapton®. The blue (resp. red) line corresponds to the experimental (resp. theoretical) spectrum. Both Rayleigh (R) and Sezawa peaks (S_1 and S_2) can be observed. The sketch illustrates the back-scattering geometry used in the present experiment. The transferred wave-vector is fixed to $k_{\parallel} = 2.14 \times 10^5$ cm^{-1}.

The light beam allows probing phonons that are thermally excited at room temperature. Because of the wave-vector conservation in the phonon-photon interaction, the wavelength of the revealed elastic waves is of the same order of magnitude as that of light. This means that the wavelength is much larger than the interatomic distances, so that the material can be described as a continuum within an effective-medium approach. The back-scattering geometry has been adopted as shown in figure 6.1.1-b). In figure 6.1.1-a), a typical experimental spectrum on the 250nm-CFB film (blue line). It was obtained with an incident angle $\xi = 65°$, so that the wave vector of the SAW is fixed to $k_{\parallel} = \frac{4\pi}{\Lambda}\sin\xi = 2.14 \times 10^5$ cm^{-1}, where $\Lambda = 5.32 \times 10^{-5}$ cm is the wavelength of the incident light (see figure 6.1.1-b)). The Rayleigh (R) and Sezawa (1st (S_1) and 2nd (S_2) harmonics) waves are clearly observed. The central green part corresponds to the elastic light scattering. The red line is a theoretical spectrum obtained by the simulation of the SAW frequencies and intensities of the thin film and by taking into account only the ripple mechanism for the scattered intensity, it has been calculated by using the formalism presented in reference [13]. The comparison between the experimental and the theoretical spectra leads to values of $Y_f = 160$ GPa ($\equiv 160 \times 10^{10}$ dyn.cm^{-2}), $G_f = 59$ GPa and $\nu_f = 0.37$. These values are consistent with those generally reported for metallic glasses, and follows the relationship between Young's modulus and shear modulus for this class of materials ($Y_f \simeq 2.6 G_f$) [20].

6.1.2 Magnetic and magneto-elastic properties

Magnetic and magneto-elastic properties of the CFB films have been studied by performing uniaxial bending tests and by using the methodology presented during chapter 4. Indeed, uniaxial, tensile and compressive stresses have been applied to the films by gluing the films on small pieces of aluminum blocks of circular cross-section of known radii R (13.2 mm, 32.2 mm, 41.6 mm, 59.2 mm, and infinite (flat surface)). In this condition, we have shown in the precedent chapters that the resulting longitudinal strain at the top surface (ε_{xx}) where the metallic film is confined can be calculated with the

following equation:

$$\varepsilon_{xx} = \left(\frac{t_f + t_s}{2R}\right)\Gamma$$

where Γ is near 1 for $t_f = 10$ or 20 nm (film thickness) and $t_s = 125$ µm (substrate thickness). The expression of the stress is thus simply given by the Hooke's law: $\sigma_{xx} = Y_f \varepsilon_{xx}$. Considering the Y_f value previously obtained by BLS, the different applied stresses for the 10 and 20 nm-films are: ±0.75 GPa, ±0.31 GPa, ±0.23 GPa, ±0.16 GPa and 0 GPa. The ones for the 250 nm-films are 8% lower than these last values.

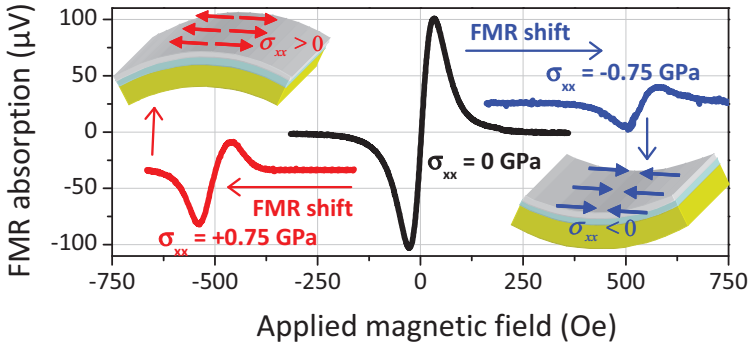

Figure 6.1.2 – FMR spectra measured at different stresses states with an applied magnetic field along the applied stress. The tensile stress (+0.75 GPa) leads to a positive shift while the compressive stress (−0.75 GPa) leads to a negative one. The spectra have been vertically shifted for a better comprehension.

Figure 6.1.2 shows typical FMR spectra recorded at different stresses states with an applied magnetic field along the applied stress for the 20 nm-film. Fore more insight, all the spectra are horizontally shifted by a value of ∼750 Oe (which corresponds to the resonance field of the non-strained spectrum). Moreover, the spectra recorded at +0.75 GPa and −0.75 GPa are vertically shifted for a better representation. Furthermore, the intensity reduction observed for the two spectra measured under non-zero stress (red and blue lines) as compared to the one measured at zero applied stress (black line) is essentially due to smaller magnetic volume of the specimen in contact with the microstripline. A positive (resp. negative) shift of the resonance field, defined as $\delta H_{res} = H_{res}(0) - H_{res}(\sigma_{xx})$, is observed when a tensile (resp. compressive) stress is applied to the film. The directions of the FMR spectra shifts lead to the conclusion that these films possess a positive magnetostrictive coefficient (see chapter 4). Moreover, one can note that the shifts presented in figure 6.1.2 are not symmetrical ($\delta H_{res} \simeq 500$ Oe for the positive shift and $\delta H_{res} \simeq -550$ Oe for the negative one). This asymmetry is due to the presence of the initial pre-stress state (before applied bending) of the whole sample which leads to an initial uniaxial anisotropy, as discussed in chapter 5.

As usual, the beforehand FMR characterization of the magnetic specimen i.e, the angular dependence of H_{res} (see figures 6.1.3-a), 6.1.3-b) and 6.1.3-c)) and its frequency dependence (see figure 6.1.3-d)) at 0 GPa allowed determining the magnetization at saturation (M_s), the gyromagnetic factor (γ) and the small uniaxial anisotropy field H_u. All these values, are found to be almost the same for the whole investigated thicknesses:

M_s = 1030 emu.cm^{-3}(confirmed by magnetometry measurements) , $\gamma = 1.948 \times 10^7$ Hz.Oe^{-1} and $H_u \simeq 40$, 45 and 30 Oe for the 10 nm, 20 nm and 250 nm-films. The full lines in figures 6.1.3-a), 6.1.3-b), 6.1.3-c) and 6.1.3-d) correspond to calculated curves using the model presented during the precedent chapters. In addition, figures 6.1.3-a), 6.1.3-b) and 6.1.3-c) also show the angular variation of H_{res} measured at different stresses states for the different films. Full symbols correspond to the experimental data while solid lines correspond to the best fits of the data using equations previously presented (see chapter 4) and by using the pre-determined values (Y_f by BLS and M_s, γ and H_u by FMR) where λ is the only unknown parameter. A similar λ value of $\sim 23 \times 10^{-6}$ is deduced for the whole investigated thicknesses. This similar value strengthens us in the fact that no thickness effect occurs

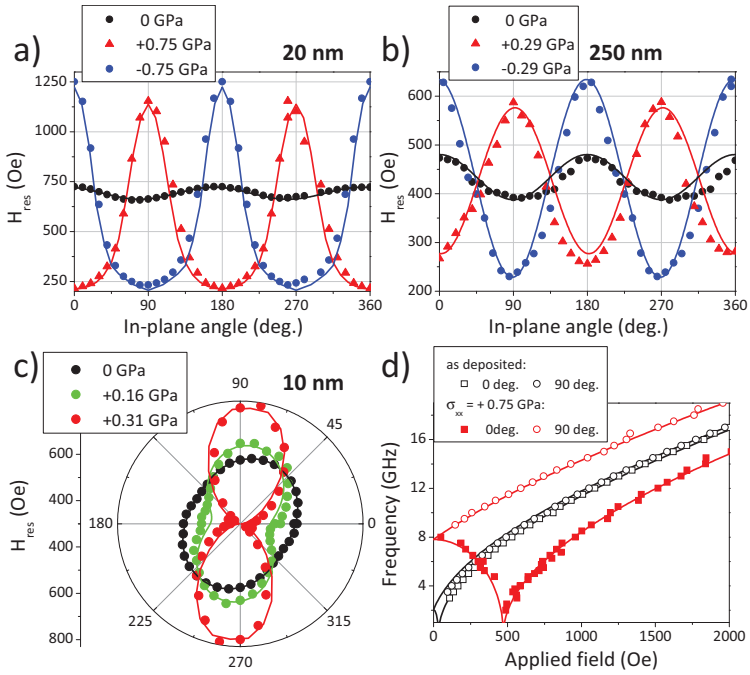

Figure 6.1.3 – Angular dependencies of the uniform mode resonance field for the (a) 20 nm (with f = 9.5 GHz), (b) 250 nm (with f = 8 GHz) and (c) 10 nm (with f = 8 GHz) films. The frequency dependence of the uniform mode is presented in (d) for the 20 nm-thick film along the easy and hard axis (90 deg. and 0 deg.) when applying a tensile stress (blue and red symbols). In all graphs, the full lines are best fits to the experimental data by using equations presented in chapter 4.

Furthermore, it is interesting to observe that the initial uniaxial anisotropy (pre-stress state) leads to non symmetrical angular dependencies for two opposite values of the applied stress (see figures 6.1.3-a) and 6.1.3-b)). Indeed, the initial anisotropy field is aligned along y direction ($\varphi_H = 90°$) which means that the initial pre-stress is compressive along x direction. Thus, the angular dependence is reinforced (resp. reduced) when the sample is compressively (resp. tensely) stressed along x. Interestingly, for the 10 nm thick film (figure 6.1.3-c)), the initial anisotropy is slightly titled with respect to the x

axis and remains slightly titled for an applied stress of +0.16 GPa. All these behaviors are well explained by the analytical modeling.

Figure 6.1.3-d) shows the frequency variation of the uniform mode measured at 0 GPa and at +0.75 GPa for an applied magnetic field along x and y direction ($\varphi_H = 0°$and 90°). A uniaxial anisotropy due to the magneto-mechanical coupling is clearly put into evidence and well described by the model. It is interesting to note that the experimental effective anisotropy field (H_u, sum of the initial anisotropy field and the one due to the applied stress) measured from the data recorded along y ($\varphi_H = 90°$) axis ($H_u \simeq 480$ Oe obtained from the experimental softening of the frequency) is in good agreement with the one resulting from the angular dependence of H_{res} ($H_u \simeq 475$ Oe from figure 6.1.3-a) by using this formula: $2H_u \simeq H_{res}(\varphi_H = 90) - H_{res}(\varphi_H = 0)$).

In this regard, figure 6.1.4-a) reports the measured effective anisotropy field H_u as a function of the applied strains. The extreme values are roughly ±500 Oe and aligned in a single straight line which reinforces the thickness-independent observed magneto-mechanical behavior of the studied thin films. In addition, the saturation magnetostriction coefficient may be also determined by using the following relation: $K_u \sim \frac{3}{2}\lambda\sigma_{xx}$ where $K_u = H_u M_s/2$. This direct determination of λ is illustrated in figure 6.1.4-b) where the slope of the linear fit directly gives the λ value ($\sim 22.5 \times 10^{-6}$) in excellent agreement with the one deduced from the whole FMR experiments.

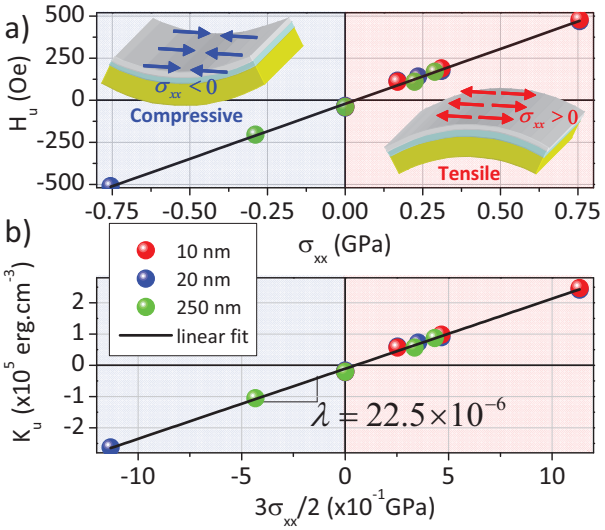

Figure 6.1.4 – a) Effective anisotropy field H_u variation as function of the applied stress. b) Variation of the effective anisotropy constant (K_u) as a function of the $\frac{3}{2}\sigma$; the linear fit slope directly gives the magnetostriction coefficient $\lambda = 22.5 \times 10^{-6}$.

Finally, the magneto-mechanical properties of these films were studied by performing compressive equibiaxial test. For this purpose, the 20 nm thick film was glued onto a 2 cm radius sphere (see schematic of figure 6.1.5). We remind that in the case of an equibiaxial bending (see chapter 2), the biaxial stress can be expressed as a function of the sphere radius R_{sphere}:

$$\sigma = \pm Y_f^* \left(\frac{d_f + d_s}{2R_{sphere}} \right) \Gamma \qquad (6.1.1)$$

with $Y_f^* = \frac{Y_f}{1-\nu_f}$ the biaxial modulus. In these conditions, an in-plane equibiaxial stress of around $\sigma \simeq +0.78$ GPa is expected for the 20 nm film (close to the uniaxial stress value generated by the cylinder whose radius is 1.32 cm); the expression of the resonance field can be written as (by neglecting the effect of H_u):

$$H_{res} = \sqrt{\left(2\pi M_s + \frac{3\lambda\sigma}{2M_s}\right)^2 + \left(\frac{2\pi f}{\gamma}\right)^2} - 2\pi M_s - \frac{3\lambda\sigma}{2M_s} \tag{6.1.2}$$

Obviously, the equibiaxial stress induced by gluing the film on the sphere leads to a vanishing φ_H dependence and a slight shift of the H_{res} baseline lower or higher than the unstressed state depending on the sign of the equibiaxial stress and of the magnetostriction coefficient. Thus, this equibiaxial stress acts as an out-of-plane anisotropy, defined for instance by $K_\perp$, which reduces or increases the value of the effective magnetization $4\pi M_{eff} = 4\pi M_s - \frac{2K_\perp}{M_s}$. Figure 6.1.5 depicts the experimental (black open circles) and calculated (black line) angular dependence of the 20 nm thick film in the benchmark state. The experimental angular dependence of the equibiaxial stress state is represented by the full red circles. As expected, this angular dependence shows that the obtained anisotropy is very far from the uniaxial case previously obtained for a similar stress value of around +0.75 GPa (with $R = 13.2$ mm) shown by the blue symbols and line on figure 6.1.5. However, a weak planar uniaxial anisotropy (~ 50 Oe), superimposed to the initial one, is observed. Indeed, the red line shows the calculated ideal equibiaxial angular dependence of H_{res} The small deviations of these experimental results from the theory are most probably due to small imperfections during equibiaxial bending. Indeed, using a flexible but non-stretchable polymer foil, such as Kapton®, it is impossible to conform perfectly on an object showing a non-zero Gaussian curvature (defined as the product of the principal curvatures).

6.2 Annealing temperature effect

A metallic glass, like CFB, could be described as a random distribution of different polyhedra (in terms of their structure and chemical composition). This structural "flexibility", compared to the rigidity of the polyhedra forming the oxide glasses, is attributed to the metallic nature of the chemical bond, not localized and non-oriented. This description is particularly relevant for understanding the formation of metallic glasses and explaining certain physical characteristics observed in direct relation to the mechanical behavior of metallic glasses. Spaepen *et al.* [22] adopted a first approach describing metallic glass by a perfectly random distribution of an atom type and free volume. Actually, the atomic "mobility" is related to the fraction of free volume distributed between the atoms. If we perform a heat treatment of a few minutes at a temperature close to the T_g, the glass relaxes; the free volume is gradually annihilated thanks to the short-range atomic mobility reducing the stored elastic energy. If we continue the heat treatment longer or at a temperature closer to the crystallization temperature T_x, the vitreous phase disappears in favor of crystals.

Ultrasonic methods, such as BLS, provide sensitive tool for probing sound velocity in solids, which are related to elastic constants. Metallic glasses are thermodynamic and kinetic metastable, and their mechanical and physical properties are very sensitive the

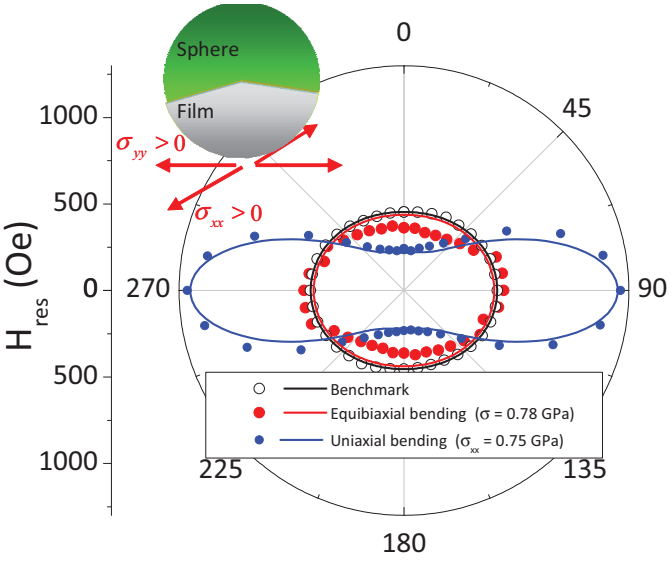

Figure 6.1.5 – Angular dependence of the resonance field for the 20 nm thick film. Symbols are experimental data while full lines are calculated thanks to the analytical models. Black open circles are data from the benchmark state while the red ones correspond to the experimental equibiaxial state (with $\sigma \simeq 0.78$ GPa). The blue circles are measurements coming from uniaxial bending with a uniaxial stress ($\sigma_{xx} \simeq 0.75$ GPa) comparable to the equibiaxial σ.

temperature. The temperature dependence of elastic properties of metallic glasses can provide important information on various transitions such as the temperature induced relaxation, structural change, crystalline phase nucleation and growth, crystallization, glass transition, and mechanical and physical properties changes in metallic glasses [20, 21].

As previously said in this chapter introduction, the Kapton® possesses a glass transition temperature around 400°C. In this condition, our films were *ex situ* annealed in the range [100°C-375°C] for 60 min in vacuum (with a pressure lower than 3×10^{-8} Torr). The films were then analyzed using BLS (for the elastic properties) and FMR (for the magnetic and magneto-elastic properties).

6.2.1 Young's modulus and Poisson's ratio variations

BLS experiments have been performed on the annealed films. Figure 6.2.1-a) shows typical BLS spectra measured with an incident angle $\xi = 65°$. The Rayleigh (R) and the first Sezawa mode (S_1) are clearly observed for all the films, the second Sezawa mode (S_2) is not always well defined. We have represented the frequency variation of R and S_1 modes in figure 6.2.1-b) by using a two ordinates graph with a common scale range (1 GHz). It is interesting to note the similar evolution in annealing temperature range for these modes. We note that after 300°C, the frequency of these modes is almost constant. From these evolutions, we can extract the evolution of the Young's modulus (Y_f) and the Poisson's ratio (ν_f) [13]. Their annealing temperature dependencies are plotted in figures

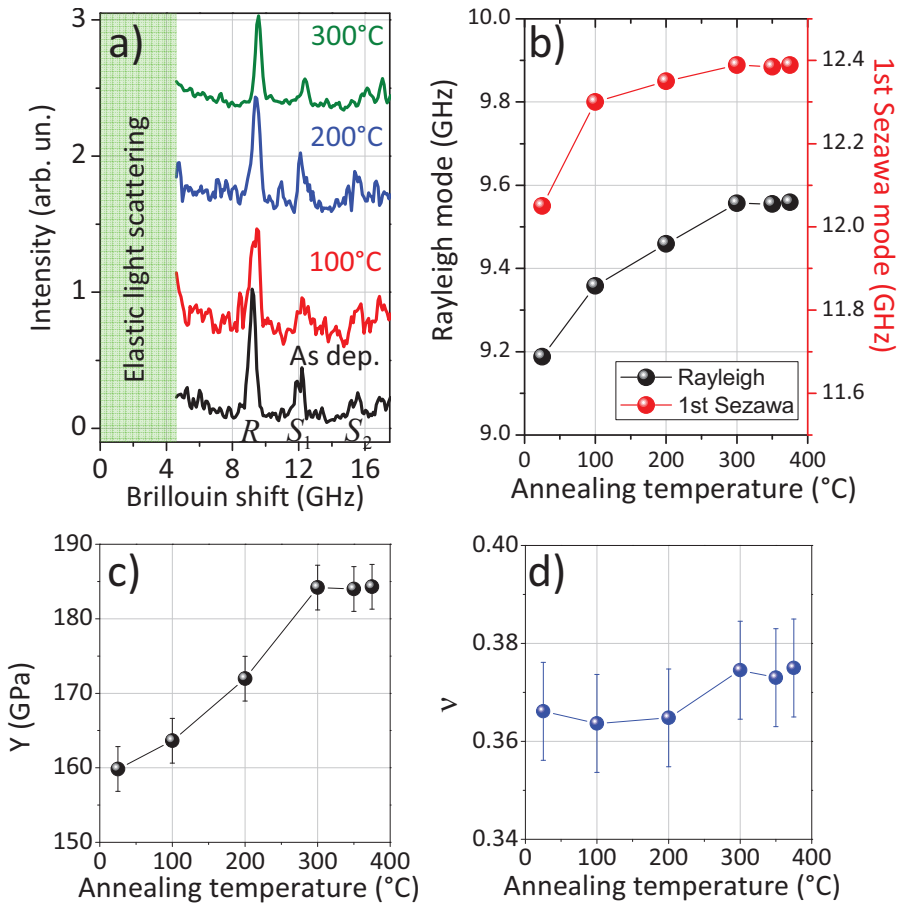

Figure 6.2.1 – a) Typical BLS spectra of the 250 nm-CFB films annealed at different temperature obtained with an incident angle $\xi = 65°$. b) Frequency variations of the Rayleigh and of the first Sezawa modes as function of the annealing temperature. c-d) Young's modulus Y (c) and Poison's ratio ν (d) variations as function of the annealing temperature. The lines in figures b), c) and d) are guided for the eyes.

6.2.1-c) and 6.2.1-d) .While ν_f varies barely, it is in fact almost constant being given the error bars, with the annealing temperature (figure 6.2.1-d)), Y_f increases with the annealing temperature, from 160 GPa for the non-annealed film before reaching a value close to 185 GPa when the film is annealed at 300 °C. Actually, in contrast to common metals and alloys, whose modulus generally decreases with increasing temperature, the metallic glasses become even much stiffer demonstrated with an enhanced elastic modulus before glass transition, and a significant increase (a few 10%) is generally observed in the supercooled liquid region (between T_g and T_x). The Y_f and ν_f variations will be used in the next subsection to quantitatively study the magneto-elastic properties as function of the annealing temperature.

6.2.2 Magnetic and magneto-elastic properties

Annealing temperature on magnetic and magnetoelastic properties have been studied by FMR. We first present experimental results obtained without applying stresses to the films. We saw in chapter 4 that thin films on flexible substrate present an inescapable uniaxial anisotropy which has been ascribed to a contrasted mechanical strength when a stiff film is deposited on compliant substrate. Figure 6.2.2-a) shows angular variations of the resonance field for the as-deposited film and film annealed at 100 °C, 300 °C and 350 °C. The anisotropy field H_u which is roughly given by $2H_u \simeq H_{res}(\varphi_H = 90) - H_{res}(\varphi_H = 0)$ increases with annealing temperature. The evolution of this anisotropy is plotted in figure 6.2.2-b). We observe that H_u is almost constant in between 25 and 200°C (values of 45, 20 and 60 Oe are respectively found). For annealing temperature higher than 200°C, an expected increase of H_u is found (+500%). Indeed, an almost constant value of $H_u \sim 250$ Oe is found (257, 236 and 247 Oe for 300°C, 350°C and 375°C, respectively). We will see that this increase can not be explained by the magnetostriction variation as function of the annealing temperature.

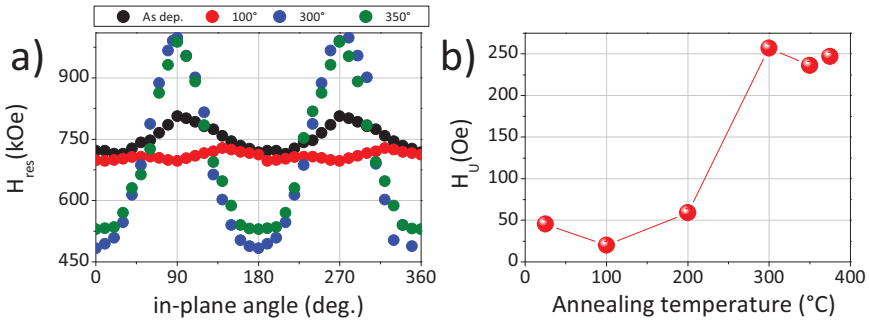

Figure 6.2.2 – a) Typical resonance field angular dependencies of the as deposited and annealed films (100°C, 300°C and 350°C). b) Evolution of the initial anisotropy field H_u as function of the annealing temperature.

FMR experiments were then performed at different stresses states by performing *in situ* uniaxial bending tests. For this purpose, we use the same aluminum blocks of circular cross-section of known radii R than the ones previously used in the precedent section, namely: R =13.2 mm, 32.2 mm, 41.6 mm, 59.2 mm, and infinite (flat surface)). Being given the evolutions of Y_f and ν_f as function of the annealing temperature (see figures 6.2.1-c) and -d)), the stresses states are not same for a similar R. Indeed, for annealing temperature higher than 200°C, the maximum applied stress σ_{xx} is ~ 0.87 GPa while it is ~ 0.75 GPa for the as-deposited film. The variations of magnetostriction λ has been extracted from methodology, namely complete fitting from the whole FMR experiments, presented in the precedent section. This methodology allows us to extract the M_s and λ evolutions as function the annealing temperature. Figure 6.2.3-a) presents M_s variations while figure 6.2.3-b) shows the λ variations. M_s is found is almost constant (around 1050 emu. cm^{-3}) for the whole films, this behavior has been confirmed by conventional magnetometry measurements (VSM). Interestingly, λ presents a quasi-similar evolution than Y_f; indeed, it is almost constant for annealing temperature lower than 300°C and shows an increase from $\sim 23 \times 10^{-6}$ to $\sim 30 \times 10^{-6}$ (+30%) for temperature higher than

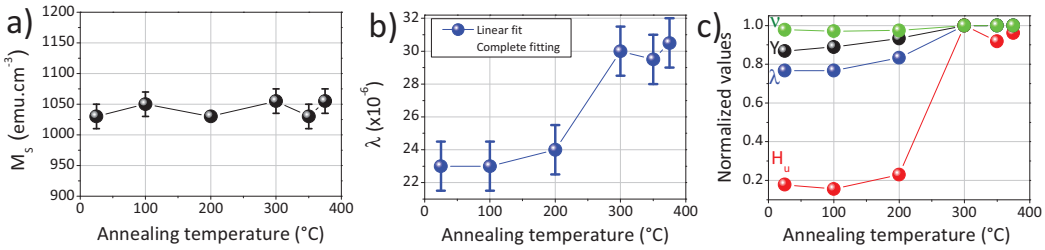

Figure 6.2.3 – Saturation magnetization M_s-a) and magnetostriction coefficient λ-b) variations as function the annealing temperature. c) Evolution of the normalized value of the Young's modulus Y, the Poisson's ratio ν, the initial anisotropy field H_u and the magnetostriction coefficient λ as function of the annealing temperature. In all graphs, lines are guide for the eyes.

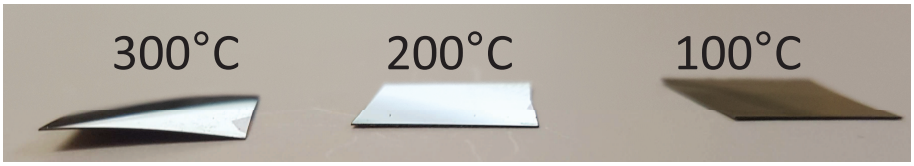

Figure 6.2.4 – Photography of three CFB samples annealed at different temperature (100°C, 200°C and 300°C) showing increasing cylindrical bending with annealing temperature. .

200°C.

Figure 6.2.3-c) summarizes the annealing temperature dependence of the elastic (Young's modulus Y_f, and Poisson's ratio ν_f) and magnetic properties (magnetostriction coefficient λ, magnetic anisotropy H_u). A convergence trend of the magnetostriction and the anisotropy field with the annealing temperature is observed. They remain unchanged for films annealed up to 200 °C before increasing for films annealed above. From these dependencies, we see that the increasing of H_u (+500%) can not be explained by the increasing of magnetostriction (+30%) and Young's modulus (+15%). Actually, the remaining influent parameter that has not been discussed is the internal stress developed during annealing. As in chapter 5, we have examined the curvature of bigger CFB samples (30×20 mm^2) annealed at different temperatures (see figure 6.2.4). We clearly see that films annealed at 100°C and 200°C are relatively flat while those annealed at 300°C is strongly curved. This might be due to internal stress evolution related to microstructural evolution of the amorphous structure. As a conclusion, the sharp increase of H_u at annealing temperature of 300°C and higher is a clear evidence of an atomic structure modification with a relaxation of the free volume for annealing temperature near the glass transition temperature of CFB.

In summary, significant evolutions of Y_f, λ and H_u are reported in $Co_{20}Fe_{60}B_{20}$ thin films. Particularly, a very strong increase of H_u is shown, which is attributed to internal stress evolution. This might be related to important microstructural evolutions between 200°C and 300°C. Such knowledges about these systems are still poor. Actually, a recent paper have reported glass transition and crystallization temperatures values in

similar systems of $Co_{40}Fe_{40}B_{20}$ ($T_g = 231$°C, $T_x = 374$°C) and $Co_{60}Fe_{20}B_{20}$ ($T_g = 278$°C, $T_x = 418$°C) thin films with similar thickness (20 nm)[23]. It is not straightforward to extrapolate values for composition studied in this thesis. However, one can suppose that the T_g value is comprised between 200°C and 300°C and the T_x one is higher than the maximum temperature studied here (375°C). Indeed, in this temperature range, we do not have seen any crystallization signature by x-ray diffraction even for higher thicknesses.

Bibliography

[1] Y. Liu , Q. Zhan and R. W. Li , Chinese Physics B **22**, 127502 (2013). (Cited on page 99.)

[2] W. Y. Chang, T. H. Fang and Y. C. Lin, Applied Physics A **92**, 693 (2008). (Cited on page 99.)

[3] X. D. Huang, S. M. Bhangale, P. M. Moran, N. L. Yakovlev and J. Pan, Polymer International **52**, 1064 (2003). (Cited on page 99.)

[4] W. A. MacDonald, M. K. Looney, D. MacKerron, R. Eveson, R. Adam, K. Hashimoto and K. Rakos, Journal of the Society for Information Display **15**, 1075 (2007). (Cited on page 99.)

[5] Z. Tang, B. Wang, H. Yang, X. Xu, Y. Liu, D. Sun, L. Xia, Q. Zhan, B. Chen, M. Tang, Y. Zhou, J. Wang and R.-W. Li, Applied Physics Letters **105**, 103504 (2014) (Cited on page 99.)

[6] Y. Yu, Q. Zhan, J. Wei, J. Wang, G. Dai, Z. Zuo, X. Zhang, Y. Liu, H. Yang, Y. Zhang, S. Xie, B. Wang and R.-W. Li, Applied Physics Letters **106**, 162405 (2015) (Cited on page 68.)

[7] S. Ikeda, K. Miura, H. Yamamoto, K. Mizunuma, H. D. Gan, M. Endo, S. Kanai, J. Hayakawa, F. Matsukura, and H. Ohno, Nature Materials **9**, 721 (2010). (Cited on page 99.)

[8] S. Kanai, M. Yamanouchi, S. Ikeda, Y. Nakatani, F. Matsukura and H. Ohno, Applied Physics Letters **101**, 122403 (2012). (Cited on page 99.)

[9] D. D. Djayaprawira, K. Tsunekawa, M. Nagai, H. Maehara, S. Yamagata, N. Watanabe, S. Yuasa, Y. Suzuki and K. Ando, Applied Physics Letters **86**, 092502 (2005). (Cited on page 99.)

[10] A. Tavassolizadeh, T. Meier, K. Rott, G. Reiss, E. Quandt, H. Hlscher and D. Meyners, Applied Physics Letters **102**, 153104 (2013). (Cited on page 99.)

[11] A. Tavassolizadeh, P. Hayes, K. Rott, G. Reiss, E. Quandt, D. Meyners, Journal of Magnetism and Magnetic Materials **384**, 308 (2015). (Cited on page 99.)

[12] H. Zhang, Y. Y. Li, M.-Y. Yang, B. Zhang Bao, G. Yang, S.-G. Wang, K.-Y. Wang, Chinese Physics B **24**, 077501(2015). (Cited on page 99.)

[13] C. Rossignol, B. Perrin, B. Bonello, P. Djemia, P. Moch, and H. Hurdequint, Physical Review B **70**, 094102 (2004). (Cited on pages 101 and 106.)

[14] A. Fillon, C. Jaouen, A. Michel, G. Abadias, C. Tromas, L. Belliard, B. Perrin, Ph. Djemia, Physical Review B **88**, 174104 (2013). (Cited on page 100.)

[15] T. Pham, D. Faurie, P. Djemia, L. Belliard, E. Le Bourhis, P. Goudeau, F. Paumier, Applied Physics Letters **103**, 041601 (2013). (Cited on page 100.)

[16] P. Villain, P. Beauchamp, K.F. Badawi, P. Goudeau, P.-O. Renault, Scripta Materialia **50,** 1247 (2004). (Cited on page 100.)

[17] P.-M. Chassaing, F. Demangeot, N. Combe, L. Saint-Macary, M. L. Kahn and B. Chaudret, Physical Review B **79**, 155314 (2009). (Cited on page 100.)

[18] H. Liang, M. Upmanyu and H. Huang, Physical Review B **71**, 241403(R) (2005). (Cited on page 100.)

[19] J.-G. Guo and Y.-P. Zhao, Journal of Applied Physics **98**, 074306 (2005). (Cited on page 100.)

[20] W. H. Wang, Progress in Materials Science **57**, 487 (2012). (Cited on pages 101 and 106.)

[21] Y. H. Wang, W. C. Chen, S. Yi Yang, and K.-H. Shen, Journal of Applied Physics **99**, 08M307 (2006) (Cited on page 106.)

[22] F. Spaepen, Acta Metallurgica **25**, 407 (1977) (Cited on page 105.)

[23] J.-Y. Tseng, Y.-T. Chen, Z. G. Chang, C. W. Wu and L. C. Yang, Journal of Nanomaterials **2015**, 371894 (2015)

(Cited on page 110.)

7 Voltage control of the magnetization probed by ferromagnetic resonance

This chapter is dedicated to the "pure" voltage control of the magnetization direction. We will first give a small introduction in order to give a basic state of the art in this topic and also to present the motivations for performing such a control. The rotation of magnetization direction will be probed by our ferromagnetic resonance set-up (in sweep frequency mode). Thus, basic in a theoretical model will be given based on the works made by Counil et al. Finally we will present our experimental results in a Co_2FeAl thin film.

7.1 Preambles

In recent decades, the development and the sophistication of growth and characterization on the atomic and nanometric scale, has led to the elaboration of smart materials which reveal captivating phenomena. In the midst of these materials, multiferroics magnetoelectric materials, currently at the cutting edge of spintronics, have attracted the attention of many groups[1, 2, 3, 4, 5]. A flurry of research activities has been launched in order to explore the physics behind these materials. From the applications standpoint, an alternative approach to overcome the scientific impediments of weak magnetoelectric coupling in single-phase multiferroics are two-phase systems of ferromagnetic and ferroelectric constituents[6]. One of the major advantages of ferromagnetic/ferroelectric extrinsic multiferroics as reported in the literature is the flexibility in the choice of the materials[6]. One of the main idea behind the fabrication of artificial magnetoelectric multiferroics is the electric or voltage control of the magnetization using electric fields for low power and ultra fast next generation electronics [8, 7].

The straightforward heterostructure allowing such a control appears to be the one presenting a piezoelectric/magnetostrictive interface wherein the interaction vector is the voltage induced in-plane strains [6, 9, 10, 11, 12, 13, 14]. In this context, our systems made by a magnetic thin film/Kapton substrate system glued onto a piezoelectric actuator can be viewed as an artificial magnetoelectric multiferroic device. We will observe the voltage induced magnetization rotation in this artificial magnetoelectric heterostructure by probing the magnetic resonance of the uniform precession mode.

For this purpose, we have used a method only based on our ferromagnetic resonance setup. The two different mode of this technique, sweep field and sweep frequency, are respectively used to perform a quantitative characterization of the effective magnetoelectric coupling as well as of the voltage induced magnetization-rotation. In a sweep field experiment, the microwave driving frequency (f_0) is kept constant while the applied magnetic field (H) is swept whereas in a sweep frequency experiment, the applied magnetic field is kept constant (H_0) and the microwave frequency (f) is swept. A resonance field

(H_{res} at fixed f_0) and a frequency resonance (f_{res} at fixed H_0) are extracted from these two modes each having their own advantage. Indeed, the sweep-field mode is more sensitive than the sweep-frequency one (both modes are of course less sensitive than standard FMR technique where resonance microwave are employed). However, contrary to the sweep-field mode, the sweep-frequency one presents the advantage of performing spectra without disturbing the magnetization distribution of the studied systems, provided that the rf field $\vec{h}_{rf}$ amplitude is weak enough (which is the case here). These behaviors are schematically presented in figure 7.1.1. These two modes have been used in the present study to characterize the indirect magnetoelectric field and to probe the voltage induced magnetization rotation. In the next section, we will briefly present basics on this FMR magnetometry.

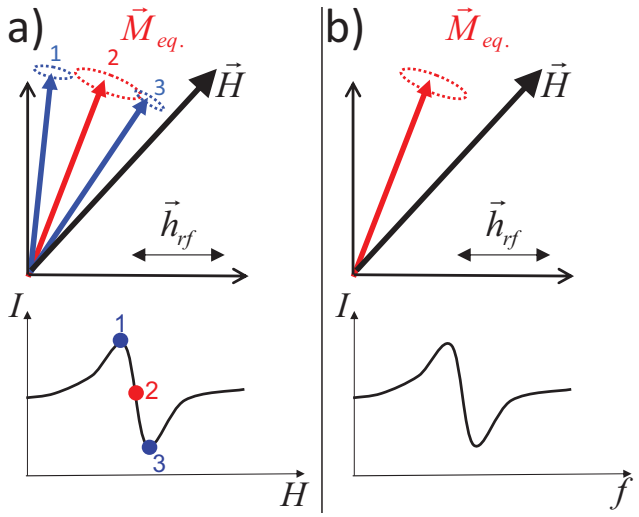

Figure 7.1.1 – b) Sweep field FMR experiment, the driving frequency is constant and the resonance is probed by sweeping the applied magnetic field around the resonance field. During this scan, a quasi-static rotation of the magnetization occurs. b) Sweep frequency FMR experiment, the applied magnetic field is fixed and the resonance is probed by scanning the driving frequency. During this scan, the magnetization distribution is not pertubed.

7.2 Magnetization direction probed by ferromagnetic resonance

We have employed the sweep-frequency-mode of our ferromagnetic resonance setup to probe the magnetization direction as function of the applied voltage by measuring both the resonance frequency and the spectra amplitudes [21]. For this purpose, the selective rule illustrated in figure 7.2.1 has been be used. In this figure, two spectra performed with a similar applied magnetic field (of 500 Oe) along y are presented; the only difference comes from the direction of the weak rf field $\vec{h}_{rf}$ (also called pumping field) emanating from the microstripline, which is either parallel ($\vec{h}_{rf} \parallel \vec{M}$) or perpendicular ($\vec{h}_{rf} \perp \vec{M}$) to the static magnetization. Indeed, the efficiency of the pumping field depends on the angle (ξ) between $\vec{h}_{rf}$ and the static part of the magnetization; it is maximum when

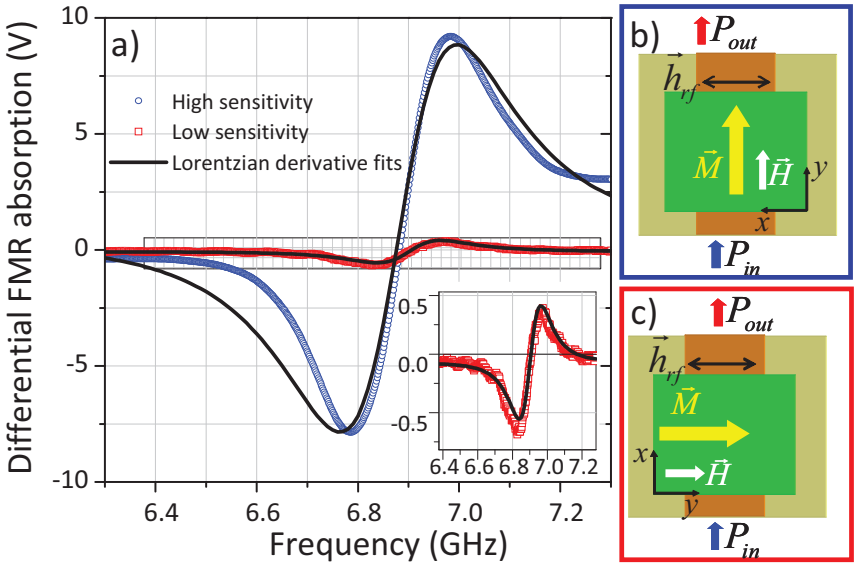

Figure 7.2.1 – a) Sweep-frequency FMR spectra obtained according to the two configurations depicted in b) and c) where P_{in} and P_{out} are the injected and transmitted radio frequency current. The only difference comes from the pumping field ($\vec{h}_{rf}$) which either parallel (red squares) or perpendicular (blue circles) to $\vec{M}$ direction giving rise to the high and low sensitivities geometries. The inset shows a zoom of the marked area. Note that a saturating field of 500 Oe was applied to ensure a uniform magnetization distribution. The solid lines show fits to the first derivative of the standard Lorentzian curve.

$\vec{h}_{rf} \perp \vec{M}$ (Figure 7.2.1-b)) and minimum when $\vec{h}_{rf} \parallel \vec{M}$ (Figure 7.2.1-c)). The idea is to take into advantage of this dependence to detect the magnetization direction. Let us consider that our signal has a Lorentzian profil:

$$\chi(f) = \frac{A}{1 + \left(\frac{f - f_{res}}{\Delta f/2}\right)^2} \tag{7.2.1}$$

Where A and f_{res} are the amplitude of the signal and the resonance frequency. The integration of such a signal in all the frequencies is then proportional the magnetic volume (τ) of the film which is excited by $\vec{h}_{rf}$, thus:

$$\tau \propto \int_0^\infty \chi(f)df = A \int_{-\frac{2f_{res}}{\Delta f}}^{\infty} \frac{dx}{1+x^2} \simeq \frac{\pi}{2} A\Delta f \tag{7.2.2}$$

This approximation is only valid if $\frac{f_{res}}{\Delta f} \gg 1$.The magnitude of the signal is maximal and proportional to $V\Delta f/\Delta f_{FMR}$ when the magnetization is perpendicular to rf-field. In order to describe the magnetization behavior for an arbitrary angle ξ between the magnetization and the rf field $\vec{h}_{rf}$ different to the two extreme cases (0 and $\pi/2$), the linearized LLG equation is used. For this, magnetization vector $\vec{M}(\vec{r}$,t) is decomposed into a static and dynamic components as follows: $\vec{M}(\vec{r},t) = \vec{M} + \vec{m}(\vec{r},t)$. We arbitrary

consider that the magnetization direction lies along y axis ($\vec{M} = M\vec{e}_y$) , thus its dynamics components are in the (xz) plane ($\vec{m}(\vec{r},t) = \vec{m_x}(\vec{r},t) + \vec{m}_z(\vec{r},t)$). The linearized LLG equation assuming weak damping limit, $\alpha \ll 1$, in the presence of in-plane $\vec{h}_{rf}$ field leads to the high-frequency magnetic susceptibility $\overleftrightarrow{\chi}(\omega)$.

$$\begin{pmatrix} m_x \\ m_z \end{pmatrix} = \begin{pmatrix} \chi_{xx}(\omega) & \chi_{xz}(\omega) \\ \chi_{xz}(\omega) & \chi_{zz}(\omega) \end{pmatrix} \begin{pmatrix} h_x(\omega) \\ 0 \end{pmatrix} \tag{7.2.3}$$

For an arbitrary angle (ξ) between the magnetization $\vec{M}$ and the pumping field $\vec{h}_{rf}$, the pumping field with a magnitude $h_{rf}\sin\xi$ is the only one that can exert a torque on the magnetization. Moreover, we measure the component of the magnetization in the plane of the film that is $m_x \sin\xi$. As a consequence, we can finally deduced the measured signal is proportional to $\sin^2\xi$ (see Eq. 7.2.4). In this case, the origin of the linewidths broadening are essentially due to the magnetization relaxation and slightly to the inhomogeneities[24, 25, 27]. The maximum of the signal is measured for $\xi = \frac{\pi}{2}$, and we can extract the relative variations of ξ.

$$I \propto \chi_{xx}(\omega)\sin^2\xi) \tag{7.2.4}$$

where $\chi_{xx}(\omega) = \chi^{'}(\omega) + i\chi"(\omega)$.

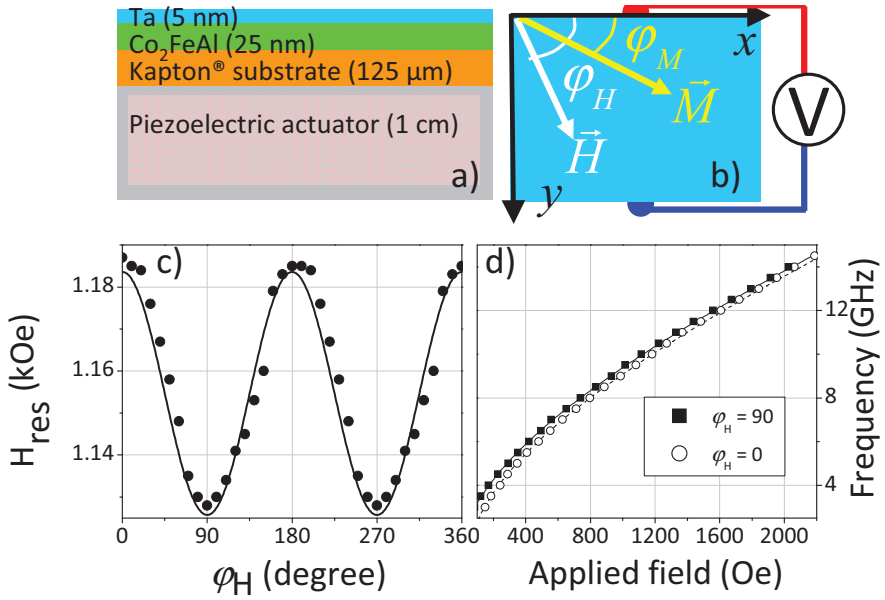

Figure 7.2.2 – a) Depiction of the cross section view of the investigated system in this chapter illustrating the CFA/Kapton® system deposited onto a piezoelectric actuator. b) Top view sketch of the system showing the different angles used in this chapter. c) Angular dependence of the resonance field measured at 10 GHz. d) Experimental and calculated frequency dependence of the uniform mode measured along the easy and hard axis ($\varphi_H = 90$ and $\varphi_H = 0$).

7.3 Experimental results

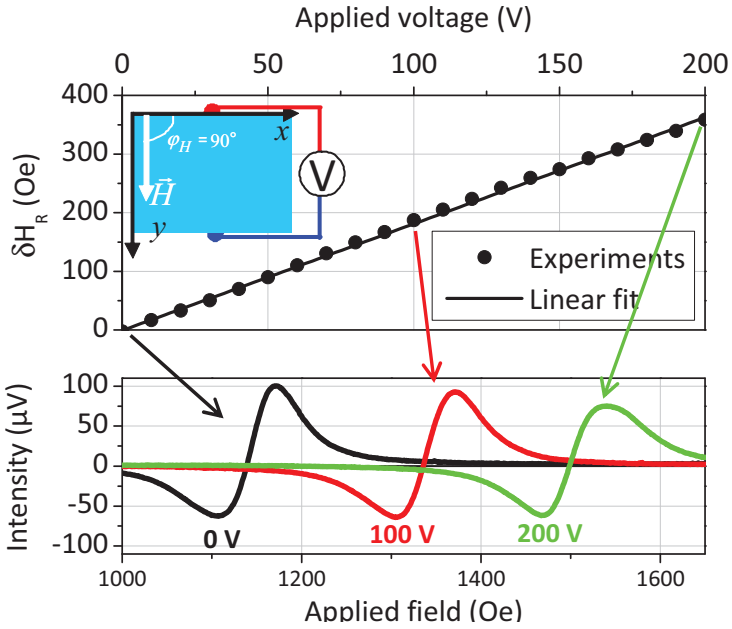

Figure 7.3.1 – Up-graph: Resonance field shift ($\delta H_{res} = H_{res}(V) - H_{res}(0)$) variation as function of the applied voltage. Circles refer to experimental data while solid line represents to the best fit. Down-graph: typical MS-FMR spectra recorded at different applied voltage (0 V, 100 V and 200 V).

The measurements have been performed in an artificial heterostructure composed of a 25 nm Co_2FeAl (CFA) thin film grown onto a 125 µm thick polyimide (Kapton®) flexible substrate and then cemented on a piezoelectric actuator. The CFA film was deposited onto the Kapton® substrate by rf sputtering. The deposition residual pressure was of around 4×10^{-9} mbar, while the working Ar pressure was of 1.3×10^{-3} mbar. A 5 nm thick Ta cap layer was deposited on the top of the CFA film in order to protect it from oxidation. CFA was chosen because of its non-negligible magnetostriction coefficient at saturation even in a polycrystalline film with no preferred orientation ($\lambda \approx 14 \times 10^{-6}$) [16, 17], as previously discussed; a strong indirect magnetoelectric field will then occur [18, 19, 20]. Moreover, we have shown that Kapton substrate does not affect the whole system magnetoelectric behavior because of its high compliance [9, 11].A sketch giving the different axis and angles is presented in figures 7.2.2-a) and 7.2.2-b).

A beforehand characterization of the magnetic properties of the heterostructure has been performed in the benchmark state (i. e. absence of applied voltage) in order to measure the effective magnetization (M_{eff}) and the gyromagnetic factor (γ) as well as the unavoidable uniaxial anisotropy (H_u) due to in-plane non-equibiaxial residual stresses. As presented in a precedent chapter, this initial anisotropy is attributed to imperfect flatness of the Kapton substrate during deposition and/or cementation on the actuator[9]. The quantitative evaluation of this initial uniaxial anisotropy is performed through the angular dependence of the uniform mode resonance field (see figures 7.2.2-c) and 7.2.2-d)) measured at $f_0 = 10$ GHz [15]. Furthermore, one can note that this anisotropy is aligned

along the y-axis since the resonance field minimum reaches a minimum at $\varphi_H = 90°$. In addition, the frequency dependencies of the uniform mode, measured along the easy ($\varphi_H = 90°$) and hard ($\varphi_H = 0°$) axes are shown in figures 7.2.2-c) and 7.2.2-d where full lines in figures 7.2.2-c) and 7.2.2-d) are the best fits to the experimental data. They allow the determination of the following parameters: $M_{eff} = 720$ emu.cm^{-3}, $\gamma = 1.835 \times 10^7$ Hz.Oe^{-1} and $H_u \sim 30$ Oe [16].

We have first recored sweep-field FMR spectra as a function of the applied voltage (with $f_0 = 10$ GHz). This latter was varied from 0 V to 200 V by step of 10 V. Figure 7.3.1 presents typical spectra measured at different applied voltages (0 V, 100 V and 200 V) with an applied magnetic field along y axis ($\varphi_H = 90°$, i. e. along the initial easy axis). A shift of the resonance field, defined as $\delta H_{res} = H_{res}(V) - H_{res}(0)$, is clearly observed. The voltage dependence of δH_{res} is shown in figure 7.3.1, where the solid line corresponds to a linear fit showing that δH_{res} is positive and almost proportional to V . This means that the y direction gradually becomes a hard magnetization axis, or a less easy one for the magnetization direction[11, 15, 17]. This is due to the positive magnetostriction coefficient of Co_2FeAl[16, 17]and to the nearly uniaxial tensile stress (i. e. $\sigma_{xx}(V) > 0$) along the x direction applied by the piezoelectric actuator to the film (for this range of applied voltage: 0 to 200V[23]). Of course, a non linear and hysteretic behavior is observed if the voltage is applied backward from 200 V to 0 V (not shown here) due to the intrinsic properties of the piezoelectric material [9, 10, 11, 15, 23]. It should be noted that the $\delta H_{res}(V)$ curve presented in figure 7.3.1 has been measured several times and all the obtained curves were superimposed. Furthermore, the resonance field shift can also be viewed as an indirect magnetoelectric field $H_{me}(V) = \delta H_{res}(V)$ aligned along x direction, i. e. perpendicular to the initial easy axis induced by the deposition conditions. The evaluation of the voltage dependence of H_{me} will serve to quantitatively study the magnetization rotation using the sweep-frequency mode of the MS-FMR setup.

In the sweep frequency experiments, the pumping field was applied parallel to x direction ($\vec{h}_{rf} \parallel \vec{x}$), i. e. perpendicular to the initial easy axis (see figure 7.2.2). In order to ensure an initial uniform magnetization along the y axis (initial easy axis), a small bias field of 40 Oe was applied. In this condition and in absence of applied voltage, $\vec{M}$ is supposed to be uniform and aligned along y axis. Then, the voltage applied to the actuator, in steps of 10 V, leads to the development of an indirect magnetoelectric field parallel to the x axis, which tends to align $\vec{M}$ along this axis. Figures 7.3.2-a), 7.3.2-b), 7.3.2-c) and 7.3.2-d) present typical spectra obtained by varying the applied voltage (0 V, 20 V, 60 V and 70 V). We clearly observe that the amplitude of the uniform mode decreases as function of the applied voltage. This amplitude is represented in figure 7.3.2-e).

The $x-$component of the magnetization along this magnetoelectric field can be plotted by using the following formula coming from the equation 7.2.4 (see precedent section):

$$m_x(H_{me}) = \frac{\cos\left(\arcsin(\sqrt{A_N(V)}\right)}{\cos\left(\arcsin(\sqrt{A_N(200\ V)}\right)} \tag{7.3.1}$$

where $A_N(200\ V)$ and $A_N(V)$ are the normalized (by the 0 V amplitude spectrum) amplitude of the 200 V spectrum and of the applied voltage spectra, respectively. The red solid line in figure 7.3.3 corresponds to the theoretical value of the normalized x-

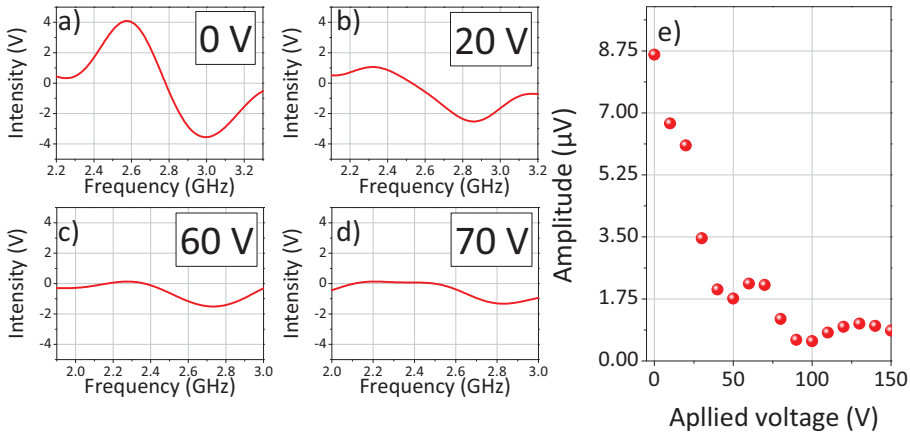

Figure 7.3.2 – a-d) Typical FMR spectra measured with the sweep frequency mode with different applied voltage values. e) Amplitude of the uniform mode signal as function of the applied voltage.

component of the magnetization as function of V. One can note that the rotation is complete at around 40 V ($H_{me} = 70$ Oe) where the magnetoelectric field totally compensates the small bias field ($H_b = 40$ Oe) and the initial anisotropy field (30 Oe). The confrontation between the model and the experimental data proves that a voltage induced magnetization rotation has been performed.

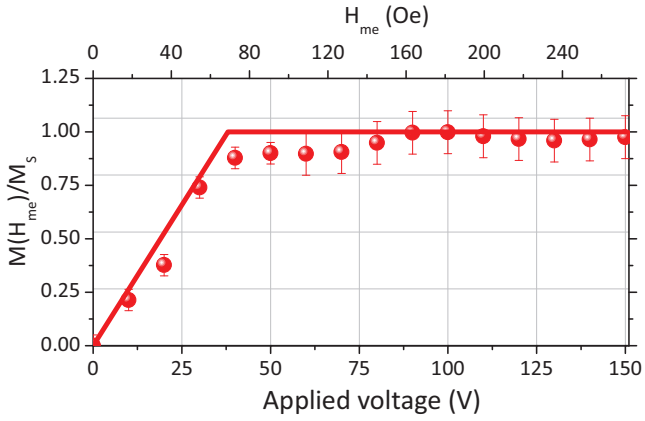

Figure 7.3.3 – Voltage dependencies of the normalized x-component of the magnetization $m_x(H_{me})$. The $m_x(H_{me})$ values have been deduced from equation 7.3.1 and the data presented in figure 7.3.2-e).

Another proof of the effective rotation of the magnetization comes from the voltage dependence of the uniform mode frequency as function of the applied voltage. The blue solid line in figure 7.3.4 refers to the simulation of this frequency being given the $H_{me}(V)$ dependence previously determined (see data in figure 7.3.1). This dependence highlights the well-known softening of the frequency when the magnetization rotates from a hard axis to an easy one [26]; the frequency minimum directly gives the voltage at which the system is in-plane isotropic (i. e. where H_{me} compensates the initial anisotropy field and

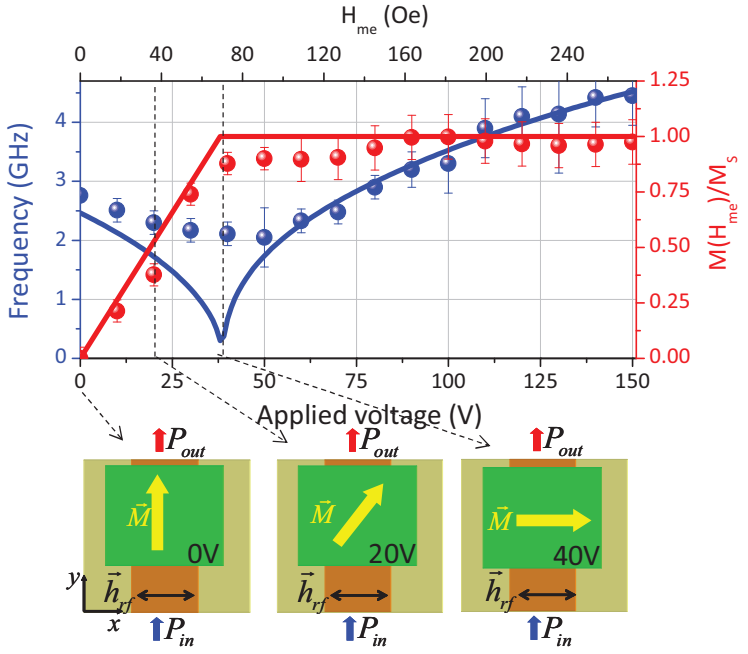

Figure 7.3.4 – Voltage dependencies of the uniform mode frequency (blue symbols) and of the normalized x-component of the magnetization $m_x(H_{me})$ with a pumping field applied along x. The $m_x(H_{me})$ values have been deduced from equation 7.3.1. The solid lines are calculated using equation 7.3.2 with the following parameters: $M_{eff} = 720$ emu.cm^{-3}, $\gamma = 1.835 \times 10^7$ s^{-1}, $H_u = 30$ Oe, $H_b = 40$ Oe. Note that the H_{me} is deduced from the data presented in figure 7.3.1. The sketches show how the magnetization direction rotates as function of the applied voltage.

the bias field). Both the experimental frequency (blue circles) and the amplitude (red circles) dependencies are well fitted by the solid lines and they clearly show a 90 degree of the magnetization direction. The theoretical values have been calculated by using a magnetic energy density of the film where the indirect magnetoelectric field is modeled by a voltage dependent uniaxial anisotropy field. In these conditions, the following analytical expression of the frequency can be derived from the Smit-Beljers equation [15]:

$$\frac{2\pi f}{\gamma} = \sqrt{(H_{me}(V) - H_u)\cos 2\varphi + H_b \sin\varphi} \times \sqrt{4\pi M_s + H_b \sin\varphi + H_u \sin^2\varphi + H_{me}(V)\cos^2\varphi} \tag{7.3.2}$$

Where φ is evaluated at each increment of the applied voltage. Finally, it should be noted that the spectra profiles were not always close to a Lorentzian one, especially at high applied voltages, which make this modeling robust [24, 25].

Bibliography

[1] N. A. Spaldin and M. Fiebig, Science, **309**, 391 (2005) (Cited on page 113.)

[2] S. -W. Cheong and M. Mostovoy, Nature Materials **6**, 13 (2007) (Cited on page 113.)

[3] R. Ramesh and N. A. Spaldin, Nature Materials **6**, 21 (2007) (Cited on page 113.)

[4] M. Bibes and A. Barthmy, Nature Materials **7**, 425 (2008) (Cited on page 113.)

[5] W. Eerenstein, N. Mathur, and J. Scott, Nature **442**, 759 (2006) (Cited on page 113.)

[6] Ce-Wen Nan, M. I. Bichurin, S. Dong, D. Viehland, and G. Srinivasan, Journal of Apllied Physics **103**, 031101 (2008) (Cited on page 113.)

[7] N. X. Sun and G. Srinivasan, Spin, **2**, 1240004 (2012) (Cited on page 113.)

[8] J. Ma, J. Hu, Z. Li, Ce-Wen Nan, Advanced Materials **23**, 1062 (2011) (Cited on page 113.)

[9] M. Gueye, F. Zighem, D. Faurie, M. Belmeguenai and S. Mercone, Applied Physics Letters **105**, 052411(2014) (Cited on pages 113, 117 and 118.)

[10] M. Weiler, A. , S. Gepr, M. Althammer, M. Opel, C. Bihler, H. Huebl, M. Brandt, R. Gross, and S. Goennenwein, New Journal of Physics **11**, 013021 (2009) (Cited on pages 113 and 118.)

[11] F. Zighem, D. Faurie, S. Mercone, M. Belmeguenai, H. Haddadi, Journal of Applied Physics **114**, 073902 (2013) (Cited on pages 79, 113, 117 and 118.)

[12] J. H. Park, J.-H. Lee, M. G. Kim, Y. K. Jeong, M.-A. Oak, H. M. Jang, H. J. Choi, and J. F. Scott, Physical Review B **81**, 134401 (2010) (Cited on page 113.)

[13] C. Thiele, K. Drr, O. Bilani, J. Rdel, and L. Schultz, Physical Review B **75**, 054408 (2007) (Cited on page 113.)

[14] C. Bihler, M. Althammer, A. Brandlmaier, S. Gepr, M.Weiler, M. Opel, W. Schoch, W. Limmer, R. Gross, M. S. Brandt, and S. T. B. Goennenwein, Phys. Rev. B 78, 045203 (2008). (Cited on page 113.)

[15] F. Zighem, A. El Bahoui, J. Moulin, D. Faurie, M. Belmeguenai, S. Mercone and H. Haddadi, Journal of Applied Physics **116**, 123903 (2014) (Cited on pages 117, 118 and 120.)

[16] M. Gueye, B. M. Wague, F. Zighem, M. Belmeguenai, M. S. Gabor, T. Petrisor, C. Tiusan, S. Mercone, and D. Faurie, Applied Physics Letters **105**, 062409 (2014). (Cited on pages 117 and 118.)

[17] S. Li, J. Xu, Q. Xue, H. Du, Q. Li, C. Chen, R. Yang, S. Xie, M. Liu, T. Nan, N. X. Sun, and W. Shao, Journal of Applied Physics **117**, 17B722 (2015) (Cited on pages 117 and 118.)

[18] M. Belmeguenai, H. Tuzcuoglu, M. Gabor, T. Petrisor Jr, C. Tiusan, D. Berling, F. Zighem, T. Chauveau, S. Chf, and P. Moch, Physical Review B **87**, 184431 (2013) (Cited on page 117.)

[19] W. Wang, H. Sukegawa, R. Shan, S. Mitani, and K. Inomata, Applied Physics Letters **95**, 182502 (2009) (Cited on page 117.)

[20] M. S. Gabor, M. Belmeguenai, F. Zighem, S. M. Chf, T. Petrisor Jr, T. Petrisor, C Tiusan and M Hehn, Spin, **4**, 1440022 (2014) (Cited on page 117.)

[21] F. Zighem, Y. Roussigne, S. M. Cherif and P. Moch, Journal of Physics: Condensed Matter **20**, 125201 (2008) (Cited on page 114.)

[22] J. Ben Youssef, N. Vukadinovic, D. Billet and M. Labrune, Physical Review B **69**, 174402 (2004) (Not cited.)

[23] F. Zighem, M. Belmeguenai, D. Faurie, H. Haddadi and J. Moulin, Review of Scientific Instruments, 85, 103905 (2014) (Cited on page 118.)

[24] G. Counil, Joo-Von Kim, T. Devolder, C. Chappert, K. Shigeto and Y. Otani, Journal of Applied Physics **95**, 5646 (2004) (Cited on pages 116 and 120.)

[25] G. Counil, J.-V. Kim, T. Devolder, P. Crozat, C. Chappert and A. Ceballada, Journal of Applied Physics **98**, 023901 (2005) (Cited on pages 116 and 120.)

[26] F. Zighem, Y. Roussign. M. Chf and P. Moch, Journal of Physics: Condensed Matter **19**, 176220 (2007) (Cited on page 119.)

[27] G. Counil, Permeametrie hyperfrequence de couches minces magnetiques, these, Universite Paris 11 (2004).

(Cited on page 116.)

Conclusions / Outlines

Overview This thesis project is devoted to the study of the magneto-mechanical properties of ferromagnetic thin films. The study of magnetic thin films on flexible substrates has developed rapidly due to the numerous applications in flexible microelectronics. Indeed, the miniaturization of the components and the need to subject them to curved geometries during their use (flexible screens, deformable GMR or GMI sensors, etc.) requires a better understanding of the effect of strains (small or large) on magnetic anisotropy of thin films. At the international level, the theme related to indirect magnetoelectric behavior in heterostructures (Ferromagnetic / Ferroelectric) whose coupling parameter is the interfacial strain is in full swing. Many prominent teams have embarked on dynamic (FMR) and static (magnetometry) measurements of magnetization under an electric field, making this topic very competitive around artificial multiferroic materials. Conversely, the study of flexible magnetic systems (thin films on polymer substrates) is still in process of maturation, requiring various skills (nanomagnetism, nanomechanics), and is thus less "monopolized" by solid-state physics teams. The articles that can be described as pioneers in research for the development of flexible sensors (essentially GMR) date back less than ten years and include studies on the effect of strains on magnetoresistance.

In this context, we have developed several original characterization techniques at LSPM to probe couplings between mechanical phenomena and magnetization. We tested in tension (by piezoelectric actuation) or bending several flexible magnetic systems. In a first step, we developed a set-up coupling deformation test, ferromagnetic resonance (FMR) and digital image correlation (DIC). We can thus follow the magnetic behavior (magnetization dynamics) and the mechanical behavior (strain field) in the same experiment. This method makes it possible to follow the evolution of the easy axis of magnetization under deformation but also to determine the effective coefficient of magnetostriction of the films (sometimes unknown). The easy axis of magnetization is determined by an azimuthal rotation of the sample for each applied strain state. Bending tests were carried out using variable radius support, making it possible to know the applied strains in the thin film.

The first tests were carried out on thin films of Co_2FeAl (thickness 20 nm) deposited on a polyimide substrate. We have thus been able to determine the magnetostriction properties of these alloys which are of great interest to the spintronics community for their high spin transfer and their Curie temperature greater than 600K. Our measurements made it possible to quantify the magnetic anisotropy field for several strain states. The proposed approach, very direct in its analysis, can be used to measure coefficients of magnetostriction of all types of thin magnetic films. This is what we have done successfully to validate the technique (Ni, NiFe, Co_2FeAl, CoFeB, FeCuNbSi) in the frame of funded projects. We then preferred to focus on the generalization of the formalism for more complex (multiaxial) solicitations rather than measuring this property for a

plethora of samples. For example, we proposed the application of this method for non-uniaxial curvatures and for larger thicknesses (a few hundred nanometers) for which the simple hypothesis on the neutral fiber axis with a flexible substrate is no longer valid. On the other hand, we have formalized the multiaxial stress dependence of ferromagnetic resonance and showed that the equivalent uniaxial constraint concept already proposed by Laurent Daniel and Olivier Hubert could be applied to this problem. We have mapped the anisotropy field of magnetoelastic origin in the principal stress space, and compared the model to our measurements either by piezoelectric (non-equi biaxial) or uniaxial bending. Thus, all the measurements can be put on a simple graph and show that all the experimental points are aligned on the same straight line. This also shows the robustness of the assumptions made for the data analysis in the two cases : bending or piezoelectric actuation.

Afterward, we were interested in the somewhat more complex problem of the influence of residual stress on the magnetic properties of thin films. Indeed, if the planar magnetic anisotropy of polycrystalline thin films is generally very weak, it is common in the literature to find a strong uniaxial anisotropy (a few hundred Gauss) in thin films deposited on polymer. It was therefore necessary to find the specificity of the magnetic films deposited on flexible substrates. Actually, the literature shows that an equi-biaxial residual stress state, which is common for a polycrystalline thin films, generally leads to a spherical curvature for a rigid substrate but rather cylindrical for a flexible one. It is this phenomenon that we have assumed to be at the source of residual uniaxial magnetic anisotropy. Fabrication of CoFeB (magnetostrictive) and $Ni_{80}Fe_{20}$ (very weakly magnetostrictive) thin films were carried out on a polyimide substrate. It was clearly shown that the curvature for the two materials is cylindrical, in agreement with theoretical predictions. This initial uniaxial curvature (before manipulation), is a source of nonequibiaxiality of the stresses in the thin film and therefore presumably of uniaxial magnetic anisotropy. Thus, we expected to measure a much stronger residual anisotropy for the CoFeB/polyimide system. This is indeed what we found experimentally by FMR. The anisotropy found is uniaxial and more than 200 times greater for the latter system. There is therefore a fairly clear correlation between the magnetostriction coefficient and residual magnetoelastic anisotropy. Moreover, on the basis of the magnetic anisotropy measurements, we were able to trace back to the radius of curvature of our samples, knowing the geometrical, elastic, magnetic and magnetoelastic parameters of the systems.

Subsequently, we have focalized on the magnetic properties of CoFeB films (metallic glass) deposited on polyimide. Particularly, we studied the effect of annealing in the accessible temperature range (0-375 °C), necessarily limited by the glass transition temperature of the substrate. We used the *in situ* curvature method to determine the magnetoelastic properties. Moreover, we have followed the influence of temperature on the elastic properties, because these last play a role in the global formalism adopted in this thesis. We found a slow evolution of the Young's modulus and the magnetostriction coefficient below 200 °C and then a significant increase between 200 °C and 300 °C (+15% and +30% respectively) that is most probably due to exceeding of the glass transition temperature of the thin film. Then, a plateau is observed between 300 °C and 375 °C, which may correspond to the supercooled liquid region of the thin film. At the same time, an enormous increase in magnetic anisotropy was observed between 200 °C and 300 °C (+500%). This is interpreted by a strong increase of the internal stresses in the

thin film when its glass transition temperature is exceeded. This is corroborated by a strong evolution of the curvature of the sample, as observed macroscopically.

Finally, we have employed a method to study the effective evolution of magnetization direction as function of the voltage-induced strains. It is based on the study of FMR spectra evolution in sweep frequency mode. Especially, the spectra amplitude as well as resonance frequency are plotted as function of the applied voltage. Therefore, we have observed the magnetization rotation in Co_2FeAl thin film on polyimide substrate. Actually, this rotation occurs at a voltage of 40 V, which corresponds to a magnetoelastic field of 70 Oe. This last compensates the small bias field (40 Oe) and the initial residual anisotropy field (30 Oe).

Perspectives Up to now, the main groups in the field of magnetic systems on flexible substrates were content to study the effect of uniaxial mechanical strains, without knowledge about microstructure evolution (plasticity, cracks, ...). However, it is also crucial to study the effect of multiaxial solicitations on magnetic properties related to deformation micro-mechanisms (plasticity, cracks initiation and evolution during cyclic loading). Thin films deposited on polymer substrates are intended to be used in flexible devices and may be exposed to repeated large biaxial deformation during manufacturing and application. Hence, their main requirements are to be robust and reliable while stretching without failing mechanically. Indeed, this is unavoidable for keeping the magnetic properties of the flexible system. An important feature in designing reliable flexible devices is to understand interface properties between the nanometric magnetic material and the polymer. Advances must be made in the relationship between film adhesion, mechanical properties and fracture, magnetic properties, which are currently weakly understood for thin films on compliant polymer substrates. Such studies are still lacking and the strain transmission from substrate to thin films must be investigated since it will also play a role in the magneto-mechanical effects.

If one is interested in the applicability of magnetic systems on flexible substrates, attention must be paid to the relationships between microcracking (phenomenon which necessarily appears for deformed thin films) and magnetic properties. This is why Finano team continue to develop new experiences to go further in understanding phenomena . In 2016, the team developed a uniaxial traction experiment with resistivity measurements and *in situ* AFM in order to accurately measure the fragmentation mechanisms of thin magnetic films. This system is not new (it exists the same at the Erich Schmid Institute in Leoben (Austria)) but it is formidably efficient in knowing the distances between cracks, their width, and the strain for which they appear and multiply. This set-up was applied to the CFB (20 nm)/polyimide system studied in chapter 5. Figure 7.0.1 shows the evolution of the relative electrical resistance as a function of the applied macroscopic deformation.

The initiation of the cracks takes place for a deformation of 1.6% (when the relative resistance marks a sudden jump with respect to its basic evolution related to the spacing of the electrical contacts (solid curve)). The evoked cracking is in fact a periodic multi-cracking of the thin film, a phenomenon well known in the "mechanical thin film" community. This is what we observed in situ by AFM at different deformation states (Figure 7.0.2). Straight fissures parallel to each other (perpendicular to the traction axis) are typical of the fragility of the thin film. We also show that the plasticity of

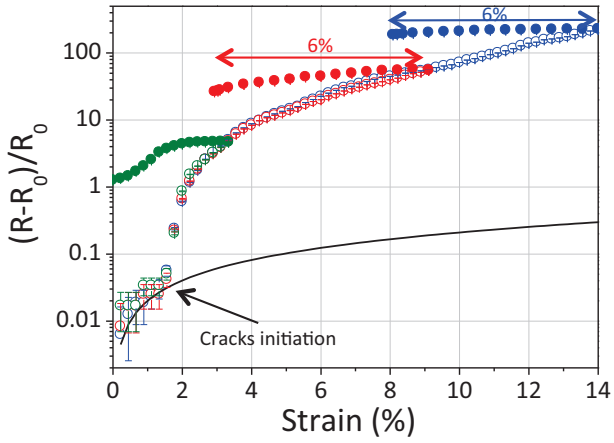

Figure 7.0.1 – Relative resistance $(R - R_0)/R_0$ as function of strain ε. Open symbols correspond to the loads and full symbols corresponds to unloads of three different samples at 3.4% (green), 9.1% (red) and 14% (blue).

the substrate beyond 5% deformation strongly limits the crack closure during the discharge. Indeed, the at least partial closure of the cracks results in a significant drop in resistivity at discharge (green curve in figure 7.0.1). The phenomenon of "buckling" for strains higher than 6% is also observed, which is linked to a transverse compressive stress applied to the fragments of films still adhering to the substrate. From these images we can derive quantitative information such as the evolution of the crack density which is correlated with the resistivity evolution.

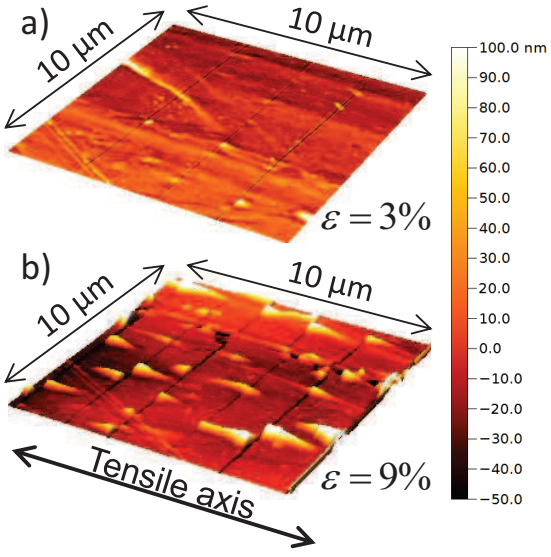

Figure 7.0.2 – 10×10 µm^2 AFM images of a CFB thin film taken at $\varepsilon = 3\%$ (a) and $\varepsilon = 9\%$ (b)

We can also roughly assess the adhesion between film and substrate by studying the morphology of the blisters ("buckles") from the model proposed by Megan Cordill in

2010 which is based on the pioneering work of Hutchinson. If we compare our measurements with those reported in the literature, the value we find for adhesion energy ($\Gamma = 5.4\, J.m^{-2}$) is in the high range of what is found in the literature for metal/polymer systems (between 1 and 7 $J.m^{-2}$). This is of course encouraging for the reliability of the studied systems.

Measurements of *ex situ* magnetic anisotropy by FMR have also been carried out on these cracked systems. In addition to the magnetoelastic energy, we have identified a very significant influence of the thin film fragmentation on the magnetic response when the cracks do not close (shape anisotropy which adds to the magnetoelastic anisotropy), see figure 7.0.3.

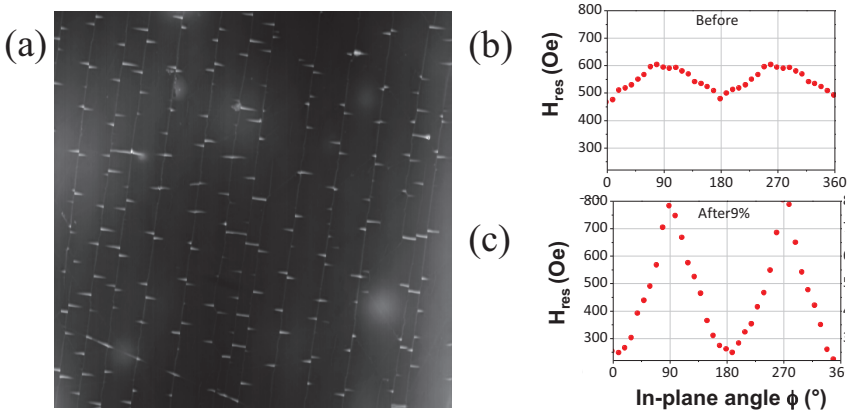

Figure 7.0.3 – (a) 20×20 µm^2 AFM images of a CFB thin film taken at $\varepsilon = 9\%$. The angular dependance of the resonance field H_{res} has been measured (b) before tensile test (c) after tensile test with maximum strain $\varepsilon = 9\%$.

These investigations are still ongoing and these results encourage Finano group to carry out new instrumental developments to follow *in situ* the magnetic behavior during large deformations (which is not possible with piezoelectric actuators for example) with a control of the biaxiality of the stresses in the plane of the thin film. Techniques allowing the control of strains along several axes with *in situ* magnetic probes are still lacking. Thus, Finano team intend to develop an instrumentation for the simultaneous study of the evolution of the magnetic properties and the strains of the film and the substrate during biaxial tensile tests. To achieve this goal, the team develops a unique experimental set that is located on the DiffAbs beamline at Soleil Synchrotron. It will combine the following complementary techniques: (i) A biaxial tensile machine dedicated to compliant materials (ii) X-ray diffraction (XRD) (iii) DIC (iv) A MOKE Magnetometer. The biaxial machine combined with DIC technique (figure 7.0.4) is already available (developed by a consortium involving Pprime Institute (Poitiers), LSPM and Diffabs Beamline (ANR Cmonano). The present development concerns the MOKE implementation in the existing set-up, which is partially funded in 2016-2017 by Region Ile de France through the "Domaine d'Intérêt Majeur" Nano-K. Moreover, a ANR project "I-Flex" involving Pprime Institute, Diffabs Beamline and Finano team (LSPM) is currently under expertise.

For several loading paths (equibiaxial or non-equibiaxial), the magnetic response will be studied at different stress states. Several kind of studies will be possible: (i) In the elastic

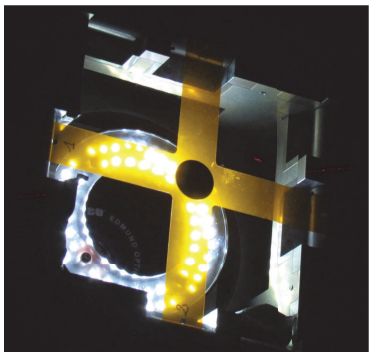

Figure 7.0.4 – Biaxial tensile device at DiffAbs Beamline (Soleil synchrotron). Here, a thin film is deposited on the center of a cruciform shaped Kapton®

domain: mapping of magnetization (M/M_s) and coercive field (H_c) in the principal stress space (σ_{xx}, σ_{yy}), relationships between strain distribution in stacks sub-layers (measured by x-ray diffraction) and magnetization, confrontation with existing magnetic models including magnetoelastic energy. (ii) Effect of plastic deformation on magnetization in such nanometric systems, study of irreversibility of magneto-mechanical behavior and influence of the loading path in the principal stress space ((σ_{xx}, σ_{yy})). (iii) Effect of cracks/decohesion in the systems at large strains on the magnetic behavior, study of mechanical cycle (effect of crack closure on global magnetization during unloadings) and reliability of the systems.

In addition, the FINANO team is gradually moving from thin films to lithographed nanostructures on flexible substrates. It is the object of a collaboration begun in 2015 with Adekunle Adeyeye (NUS Singapore) with whom the team had two funded projects *via* the USPC / NUS alliance (MagnoFlex2016 lead by F. Zighem, and NanoFlex2017 lead by D Faurie) and with whom FINANO develop an ANR PRCI project. The aim is to fabricate flexible magnonic systems (periodic lattice of magnetic nanostructures) on a flexible substrate and optimize their properties. These are elaborated by interferential lithography at NUS (figure 7.0.5).

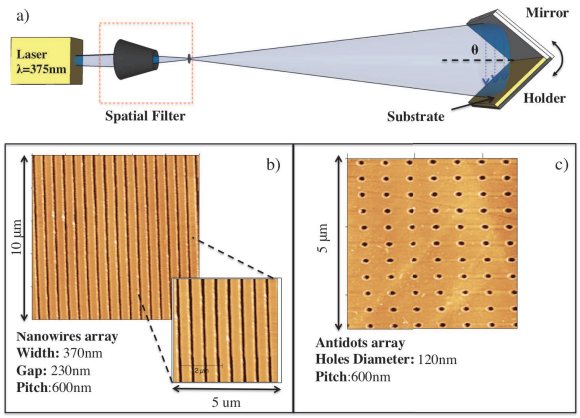

Figure 7.0.5 – (a) Schematic diagram of interferential lithography. (b) NiFe nanowires on polyimide. (c) NiFe antidots on polyimide

Magnetic nanostructures (nanowires and antidots (periodically holes thin films) of CoFeB and NiFe have already been studied by FMR and *in situ* deformation. The first results show that it is possible to adjust by strains the resonance fields of the different magnetic resonance modes of these arrays of nanostructures.

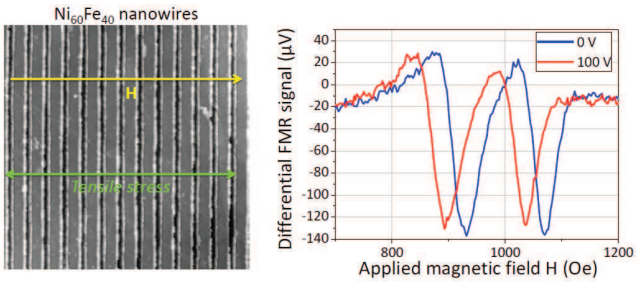

Figure 7.0.6 – On the left: AFM image of magnetostrictive Ni60Fe40 nanowires; the magnetic field and principal applied stress directions are shown. On the right: preliminary study of voltage induced-strain effect on two quantized modes by in situ FMR (f = 8 GHz).

These results are currently non-existent in the literature and will be published next. However, several questions remain: what is the strain transmission from the substrate to the film when the lateral sizes are of the same order as the thickness? What then is the effect on magnetization? How do these objects submitted to higher strains behave? Concerning the first two questions, it will be possible to find some elements of answers by a finite element modeling developed by F. Zighem, D. Faurie and M. Haboussi (LSPM) under Comsol®. They have implemented LLG (Landau-Lischfitz-Gilbert) equations describing the magnetization dynamics by introducing the different energy terms (Zeeman, exchange, dipolar, magnetoelastic, elastic) involved in the problem. Actually, the lateral nanostructuring of our samples induces important strain heterogeneities that cannot be neglected. Thus, for these nano-objects, the hypothesis of a uniform magnetoelastic anisotropy field is no longer valid.

List of publications

1. **M. Gueye**, F. Zighem, M Belmeguenai, M. Gabor, C. Tiusan, D. Faurie
Ferromagnetic resonance in thin films submitted to multiaxial stress state : application of the uniaxial equivalent stress concept and experimental validation Journal of Physics D : Applied Physics **49**, 265001 (2016)
2. **Mouhamadou Gueye**, Pierpaolo Lupo, Fatih Zighem, Damien Faurie, Mohamed Belmeguenai, Adekunle Olusola Adeyeye
Unambiguous magnetoelastic effect on residual anisotropy in thin films deposited on flexible substrates Europhysics Letters, **114**, 17003 (2016)
3. **M. Gueye**, F. Zighem, M. Belmeguenai, M. S. Gabor, C. Tiusan, D. Faurie,
Spectroscopic investigation of elastic and magnetoelastic properties of CoFeB thin films Journal of Physics D : Applied Physics, **49**, 145003 (2016)
4. **M. Gueye**, F. Zighem, M. Belmeguenai, M. S. Gabor, C. Tiusan, D. Faurie
Effective 90-degree magnetization rotation in Co2FeAl thin film/piezoelectric system probed by microstripline ferromagnetic resonance Applied Physics Letters, **107**, 032908 (2015)
5. **M. Gueye**, B. M. Wague, F. Zighem, M. Belmeguenai, M.S. Gabor, T. Petrisor Jr, C. Tiusan, S. Mercone, D. Faurie
Bending strain-tunable magnetic anisotropy in Co2FeAl Heusler thin film on Kapton® Applied Physics Letters, **105**, 062409 (2014)
6. **M. Gueye**, F. Zighem, D. Faurie, M. Belmeguenai, S. Mercone
Optimization of indirect magnetoelectric effect in thin-film/substrate/piezoelectric-actuator heterostructure using polymer substrate Applied Physics Letters, **105**, 052411 (2014)

Abstract

Films minces sur susbtrats flexibles: Etude des propriétés magnéto-mécaniques par résonance ferromagnétique

Les films minces déposés sur des substrats flexibles ont été intensivement étudiés ces dernières années en raison de leur nombreuses applications en électronique flexible. Depuis peu, l'électronique flexible est étendu aux matériaux magnétiques conduisant ainsi au domaine émergeant de la magnéto-électronique flexible actuellement à l'avant garde des sujets de recherche de la spintronique. Ce travail de thèse est dédié à l'étude des propriétés magnéto-mécaniques de films minces magnétiques (Ni, NiFe, Co2FeAl, CoFeB, FeCuNbSi) sur des substrats flexibles. Les analyses structurales ont montré que les films de Ni et de CFA sont polycristallins non texturés; le CFB est amorphe. Par conséquent, les propriétés élastiques et magnétoélastiques de ces films sont considérées comme étant isotropes. Une technique basée sur une utilisation conjointe d'essais mécaniques, la résonance ferromagnétique (FMR) et la corrélation d'images numériques (CIN) a été développée pour étudier les propriétés magnéto-mécaniques de films minces sur substrats flexibles. A l'aide de cette méthode, il est possible de suivre l'évolution de l'anisotropie résiduelle omniprésente dans les films magnétiques sur substrats flexibles. Cette anisotropie est liée aux propriétés mécaniques contrastées lorsqu'on dépose un film mince rédige (grand module d'Young) sur un substrat flexible (petit module d'Young). L'effet du recuit sur les propriétés élastiques et magnétoélastiques a été soigneusement étudié dans le film CFB validant ainsi l'intérêt porté à ses alliages pour des applications en spintronique. Enfin, la résonance ferromagnétique est employé en balayage en fréquence pour suivre la variation de la direction de l'aimantation en fonction des déformations induites par l'application de tension électrique sur l'actionneur piézoélectrique. Un retournement de 90° de la direction de l'aimantation dans le film Co2FeAl sur substrat flexible de Kapton® est observé.

Mots-clés: résonance ferromagnétique (FMR), magnétoélasticité, films minces, anisotropy magnétique, systèmes flexibles.

Magnetic thin films on flexible substrates: magnetomechanical study by ferromagnetic resonance

This thesis project is devoted to the study of the magneto-mechanical properties of ferromagnetic thin films. The study of magnetic thin films on flexible substrates has developed rapidly due to the numerous applications in flexible microelectronics. Indeed, the miniaturization of the components and the need to subject them to curved geometries during their use (flexible screens, deformable GMR or GMI sensors, etc.) requires a better understanding of the effect of strains (small or large) on magnetic anisotropy of thin films.

Abstract

In this context, we have developed several original techniques during this thesis to probe coupling between mechanical phenomena and magnetization. We tested in tension (by piezoelectric actuation) or bending several flexible magnetic systems. In a first step, we developed a set-up coupling deformation test, ferromagnetic resonance and digital image correlation. We can thus follow the magnetic (magnetization dynamics) and mechanical behaviours (strain field) in the same experiment. This method allows following the magnetization easy axis variation under deformation but also allows the magnetostriction determination of the films (sometimes unknown). The first tests were carried out on thin Co2FeAl and CoFeB films deposited on polyimide substrates. We have thus been able to determine these alloys magnetostriction coefficients which are of great interest for the spintronics community. The proposed approach, very direct in its analysis, can be used to measure coefficients of magnetostriction of all types of thin magnetic films. We then focussed on the generalization of the formalism for multiaxial sollicitations. For example, we proposed the application of this method for non-uniaxial curvatures and for larger thicknesses (a few hundred of nanometers) for which the simple hypothesis on the neutral fibber axis with a flexible substrate is no longer valid. On the other hand, we have formalized the multiaxial stress dependence of ferromagnetic resonance and showed that the equivalent uniaxial constraint concept already proposed by L. Daniel and O. Hubert could be applied to this problem. Afterward, we were interested in the somewhat more complex problem of the influence of residual stress on the magnetic properties of thin films.

Subsequently, we have focalized on the magnetic properties of CoFeB films (metallic glass) deposited on flexible substrates. Particularly, we studied the effect of annealing in the accessible temperature range (till 375°C) limited by the polymer. We used the in situ curvature method to determine the magnetoelastic properties. Moreover, we have followed the influence of temperature on the elastic properties, because these last play a role in the global formalism adopted in this thesis. We found a slow evolution of the Young's modulus and of the magnetostriction coefficient below 200°C and then a significant increase between 200°C and 300°C (+15% and +30% respectively) that is most probably due to exceeding of the glass transition temperature of the film. Then, a plateau is observed between 300°C and 375°C, which may correspond to the supercooled liquid region of CoFeB. In addition, an enormous increase in magnetic anisotropy was observed between 200°C and 300°C (+500%). This is interpreted by a strong increase of the internal stresses in the thin film when its glass transition temperature is exceeded. This is corroborated by a strong evolution of the curvature of the sample, as observed macroscopically.

Finally, we have astutely employed a method to measure the magnetization direction variation as function of a voltage-induced strains. It is based on the study of FMR spectra evolution in sweep frequency mode. Especially, the spectra amplitude as well as resonance frequency are plotted as function of the applied voltage. Therefore, we have observed the magnetization rotation in Co2FeAl thin film on polyimide substrate. Actually, this rotation occurs at a voltage of 40V, which corresponds to a magnetoelastic field of 70 Oe. This last compensates the small bias field (40 Oe) and the initial residual anisotropy field (30 Oe).

Keywords: ferromagnetic resonance, magnetoelasticity, thin films, magnetic anisotropy, flexible systems.

Abstract